

UNIVERSITY OF CALIFORNIA SAN DIEGO

**Check it out! Examining western boundary currents using global ocean observations**

A dissertation submitted in partial satisfaction of the  
requirements for the degree Doctor of Philosophy

in

Oceanography

by

Mitchell Chandler

Committee in charge:

Nathalie V. Zilberman, Chair  
Janet Sprintall, Co-Chair  
Katharine Ricke  
Lynne Talley

2025

Copyright

Mitchell Chandler, 2025

All rights reserved.

The Dissertation of Mitchell Chandler is approved, and it is acceptable in quality  
and form for publication on microfilm and electronically.

University of California San Diego

2025

## EPIGRAPH

*You'll be probably frightened at times, scared, worried. You'll hate it, you'll absolutely despise the fact that you're involved and when you get to the finish, you'll know why: because there's nothing like it.*

— Sir Peter Blake

## TABLE OF CONTENTS

Dissertation Approval Page .....	iii
Epigraph .....	iv
Table of Contents .....	v
List of Figures .....	vii
Acknowledgements .....	xi
Vita .....	xiii
Abstract of the Dissertation .....	xiv
Chapter 0     Introduction .....	1
Chapter 1     Seasonal To Decadal Western Boundary Current Variability From Sustained Ocean Observations .....	6
1.1 Abstract .....	6
1.2 Plain Language Summary .....	7
1.3 Introduction .....	7
1.4 Data and Methods .....	9
1.4.1 Data .....	9
1.4.2 Computing Velocity Estimates .....	10
1.4.3 Metrics of WBC Variability .....	12
1.5 Results and Discussion .....	13
1.5.1 Mean Transport and Trends .....	13
1.5.2 Annual Cycles .....	15
1.5.3 Temporal Variability in the Location of the WBC .....	17
1.6 Conclusions .....	20
1.7 Open Research .....	22
1.8 Acknowledgements .....	22
1.A Supplementary Figures for Chapter 1 .....	24
Chapter 2     ENSO Influences Subsurface Marine Heatwave Occurrence In The Kuroshio Extension .....	30
2.1 Abstract .....	30
2.2 Plain Language Summary .....	31
2.3 Introduction .....	31
2.4 Data and Methodology .....	34
2.4.1 Data .....	34
2.4.2 Synthetic Temperature Time Series Development .....	37
2.4.3 Synthetic Temperature Time Series Validation .....	38

2.4.4	Marine Heatwave Identification .....	40
2.5	Results and Discussion .....	42
2.5.1	Temperature Trends .....	42
2.5.2	Trends in Marine Heatwave Occurrence .....	45
2.5.3	Marine Heatwave Primary Metrics .....	47
2.5.4	Influence of ENSO on Marine Heatwave Occurrence .....	49
2.6	Conclusions .....	55
2.7	Open Research .....	58
2.8	Acknowledgments .....	59
2.A	Supplementary Figures for Chapter 2 .....	60
2.B	Supplementary Text for Chapter 2 .....	64
<b>Chapter 3</b>	<b>The Deep Western Boundary Current Of The Southwest Pacific Basin: Insights From Deep Argo .....</b>	<b>65</b>
3.1	Abstract .....	65
3.2	Plain Language Summary .....	66
3.3	Introduction .....	67
3.4	Data and Methodology .....	72
3.4.1	Deep Argo Profiles and Trajectories .....	72
3.4.2	Ocean Reanalysis .....	74
3.4.3	Ekman Pumping .....	75
3.4.4	Turbulent Mixing .....	76
3.4.5	Seasonality .....	77
3.5	Results .....	79
3.5.1	Deep Western Boundary Current Pathway .....	79
3.5.2	Turbulent Mixing .....	82
3.5.3	Kermadec Trench Seasonality .....	84
3.6	Discussion .....	90
3.7	Open Research .....	97
3.8	Acknowledgements .....	98
3.A	Supplementary Figures for Chapter 3 .....	99
<b>Chapter 4</b>	<b>Conclusions .....</b>	<b>104</b>
4.1	Future Research Questions .....	106
4.2	Summary .....	107
<b>Bibliography</b>	<b>.....</b>	<b>109</b>

## LIST OF FIGURES

<p>Figure 1.1. (a) Mean dynamic height at the surface relative to 1975-dbar from Argo.          (b–d) Mean depth-integrated absolute geostrophic velocity across HR-XBT transects (b) IX21, (c) PX30, and (d) PX40. ....</p> <p>Figure 1.2. Longitude-time Hovmöller plots of depth-integrated absolute geostrophic velocity for the western section of HR-XBT transects (a) IX21, (b) PX30, and (c) PX40. ....</p> <p>Figure 1.3. Annual cycles in the Agulhas Current, East Australian Current, and Kuroshio for: (a–c) western boundary current transport; (d–f) core depth-integrated velocity; (g–i) offshore edge deviations. ....</p> <p>Figure 1.4. (a) Monthly time series of Agulhas Current core longitude. (b) Absolute cross-transect geostrophic velocity composite for Natal Pulse (NP) events. (c) As in (b) but for non-NP periods. (d) Difference between the two composites. (e) Composite of monthly sea level anomaly for NP months.</p> <p>Figure 1.5. (a) Absolute cross-transect geostrophic velocity composite for periods when the Kuroshio Extension Index (KEI) is positive. (b) As in (a) but for negative KEI. (c) Difference between the two composites. ....</p> <p>Figure A1.1. Cross-transect volume transport across transect PX40 between 0–1975-m and 143.95–148.35°E from our monthly estimates and from the Kuroshio Extension System Study. ....</p> <p>Figure A1.2. Number of Argo trajectory measurements between 900–1100-dbar (a–c) each year and (d–f) each month along HR-XBT transects IX21, PX30, and PX40. ....</p> <p>Figure A1.3. Comparison between our monthly estimates of geostrophic volume transport between 153.75–155.25°E across transect PX30 and total volume transport between 153.77–155.30°E across a mooring array at 27°S. ....</p> <p>Figure A1.4. Time series of monthly western boundary current transport between the surface and 1975-m for the (a) Agulhas Current, (b) East Australian Current, and (c) Kuroshio. ....</p> <p>Figure A1.5. Cross-transect absolute geostrophic velocity (a) time-mean and (b) trend over 2004–2019 in the poleward-flowing Kuroshio across transect PX40. .</p> <p>Figure A1.6. Weekly time series of the Kuroshio Extension Index. ....</p> <p>Figure 2.1. PX40 nominal transect overlain on the bathymetry of the northwest Pacific Ocean. ....</p>	<p style="text-align: right;">9</p> <p style="text-align: right;">12</p> <p style="text-align: right;">16</p> <p style="text-align: right;">18</p> <p style="text-align: right;">19</p> <p style="text-align: right;">24</p> <p style="text-align: right;">25</p> <p style="text-align: right;">26</p> <p style="text-align: right;">27</p> <p style="text-align: right;">28</p> <p style="text-align: right;">29</p> <p style="text-align: right;">34</p>
---	--

Figure 2.2.	Time-mean of the 2004 to 2019 monthly cross-transect velocity time series from <b>(a)</b> Chandler et al. (2022a) and <b>(b)</b> GLORYS, and <b>(c)</b> correlation coefficients between the two time series. . . . .	36
Figure 2.3.	Leave-one-out validation between HR-XBT observed temperature anomalies and synthetic temperature anomalies. . . . .	39
Figure 2.4.	Validation between Kuroshio Extension System Study temperature anomalies and synthetic temperature anomalies. . . . .	40
Figure 2.5.	<b>(a)</b> Temperature trends over 1993 to 2022. <b>(b)</b> Vertical temperature gradients in the 1993 to 2022 time-mean temperature. <b>(c)</b> Temperature anomaly time series over 1993 to 2022 in the region where Kuroshio warming trends were largest. . . . .	44
Figure 2.6.	Trends over 1993 to 2022 in <b>(a)</b> marine heatwave days per year and <b>(b)</b> marine heatwave days per year when the 1993 to 2022 temperature trend is removed. . . . .	46
Figure 2.7.	Mean <b>(a)</b> intensity and <b>(b)</b> duration averaged over all marine heatwave events between 1993 and 2022. . . . .	48
Figure 2.8.	Percentage of time that marine heatwaves occurred along PX40 during El Niño and La Niña over 1993 to 2022. . . . .	50
Figure 2.9.	GLORYS depth-integrated velocity <b>(a)</b> 1993 to 2020 time-mean, and anomalies averaged during <b>(b)</b> El Niño and <b>(c)</b> La Niña. . . . .	51
Figure 2.10.	Difference in temperature anomaly mean and standard deviation during El Niño and La Niña compared to the full 1993 to 2022 time series. . . . .	53
Figure 2.11.	Percentage of time that subsurface marine heatwaves occurred along PX40 during <b>(a)</b> Eastern Pacific El Niño conditions and <b>(b)</b> Central Pacific El Niño conditions over 1993 to 2022. . . . .	54
Figure A2.1.	Change in temperature anomaly variance, sea level anomaly variance, and eddy kinetic energy variance along transect PX40 between the first half and second half of the time series. . . . .	60
Figure A2.2.	GLORYS depth-integrated velocity anomalies averaged during the longest duration ( $>30$ days) MHW events at $144.05^{\circ}\text{E}$ , 440-m deep. . . . .	61
Figure A2.3.	Percentage of time that subsurface marine heatwaves occurred along PX40 during El Niño and La Niña over 1993 to 2022 when using a 20-day duration threshold. . . . .	62

Figure A2.4.	Percentage of time that surface marine heatwaves occurred along PX40 during El Niño and La Niña over 1993 to 2022 when using a 20-day duration threshold and when applying the Hobday et al. (2016) definition to daily observations.....	63
Figure 3.1.	Bathymetry at the western boundary of the Southwest Pacific Basin with a schematic of the deep western boundary current pathway. ....	68
Figure 3.2.	Meridional sections of <b>(a)</b> potential temperature and <b>(b)</b> salinity between 2000–6000-dbar from Deep Argo profiles collected at the western boundary of the Southwest Pacific Basin. ....	70
Figure 3.3.	<b>(a)</b> Locations of Deep Argo profiles and <b>(b)</b> number of Deep Argo profiles per month.....	73
Figure 3.4.	Potential temperature – salinity curves for Deep Argo profiles and GLORYS profiles in the Kermadec Trench. ....	75
Figure 3.5.	<b>(a)</b> Deep Argo trajectory velocities in the deep western boundary current of the Southwest Pacific Basin and historical time-mean velocities from WOCE mooring array <b>(b)</b> PCM9 in the Kermadec Trench and <b>(c)</b> PCM11 in the Samoan Passage. ....	80
Figure 3.6.	<b>(a)</b> GLORYS time-mean velocity in the Kermadec Trench. <b>(b)</b> Comparison of Deep Argo trajectory velocity and GLORYS velocity in the Kermadec Trench. <b>(c)</b> Comparison of the speed of the Deep Argo trajectory velocities and GLORYS velocities in the Kermadec Trench. ....	81
Figure 3.7.	Estimates of vertical turbulent diffusivity through the Samoan Passage....	83
Figure 3.8.	Seasonal cycles between 2000–4000-dbar from Deep Argo profiles in the Kermadec Trench DWBC for <b>(a)</b> dynamic height, <b>(b)</b> salinity, <b>(c)</b> potential temperature, and potential temperature decomposed into <b>(d)</b> heave and <b>(e)</b> spice components. ....	86
Figure 3.9.	As for Figure 3.8 but computed from GLORYS interpolated to the locations of Deep Argo profiles in the Kermadec Trench DWBC. ....	88
Figure 3.10.	Seasonal cycles in the northern Kermadec Trench DWBC for <b>(a)</b> Ekman pumping from ERA5 and <b>(b)</b> dynamic height from GLORYS. <b>(c)</b> Coherence and <b>(d)</b> phase between 1993–2020 detrended monthly anomalies of Ekman pumping and dynamic height. ....	90

Figure A3.1. (a) Locations of Deep Argo profiles immediately upstream and downstream of the Samoan Passage. (b) Potential temperature - salinity curves for profiles upstream and downstream of the Samoan Passage and solutions of the numerical model applied to the mean upstream profile. ....	99
Figure A3.2. As for Figure A3.1, but applied to the Louisville Seamount Chain collision zone. ....	100
Figure A3.3. Detrended 1993–2020 monthly anomalies of (a) Ekman pumping from ERA5 and (b) dynamic height from GLORYS, both in the northern Kermadec Trench DWBC. ....	101
Figure A3.4. (a) Seasonal cycle of GLORYS dynamic height in the northern Kermadec Trench DWBC, and (b) coherence and (c) phase at the annual period between 1993–2020 monthly anomalies of detrended local Ekman pumping and dynamic height.....	102
Figure A3.5. (a) Seasonal cycle of GLORYS northward meridional velocity at 3221-m depth in the northern Kermadec Trench DWBC. (b) Mean difference in GLORYS meridional velocity between March and August at 3221-m depth in the Kermadec Trench and surrounding area. ....	103

## ACKNOWLEDGEMENTS

Firstly, of course, an immense thank you to my advisors – Nathalie Zilberman and Janet Sprintall – for your valuable support and guidance. Graduate school brings a whole suite of challenges, and being an international student only adds to them. Although it was never intentional, I believe it turned out to be rather valuable having advisors who better understood some of the additional challenges that come with being a foreign national in America. Thank you also to my two other committee members – Lynne Talley and Kate Ricke – your contributions have been much appreciated.

To the first-year office – especially Matt, Hayden, Youran, and Monica – I am not sure I would have passed all our first-year classes without you.

During my time in graduate school, I suffered a moderately significant TBI that had a drastic impact on my ability to do, well, anything. My recovery back to being able to complete everyday tasks – let alone being able to perform intensive academic research – was a slow, frustrating, and lonely experience. I do not think I could have made the progress I did without the support of Wellbutrin and the team – Alan, Stacy, and Liz – at the UCSD Concussion Clinic. For that, you have my gratitude (and also my money, @US\_Healthcare).

I am appreciative of the physical oceanography community back home in New Zealand – including Denise Fernandez and Phil Sutton – who allowed me to stay engaged and connected via remote participation in zoom chats and workshops. In addition, I would like to acknowledge my Honours advisors – Melissa Bowen and Rob Smith – who provided the foundation that has allowed me to succeed at graduate school. Thank you also to Gary Wilson, who first introduced me to the concept of oceanography while I was in high school, and then later pushed me to apply for the Fulbright Scholarship that initially brought me to the US. You have had a much larger influence on my career, and indeed life, than you probably realise.

Thank you to my family – Diane, Lyndon, and Holly – for your love and support. You instilled in me my appreciation and curiosity for the natural environment that I now get to study. I would also like to thank my American family – Carol and Michael, and the late Molly and Paco

– for giving me a home away from home. Being welcomed into your family with open arms was especially important to me when border closures meant that I was unable to spend Christmas with my immediate family. I hope you know how much I appreciate you.

Lastly, and most importantly, a huge thank you to my housemate-turned-girlfriend-turned-partner-turned-fiancee – Sarah McTague. You have experienced every step of this journey with me and I truly could not have made it through these last (almost) 6 years without you. Words cannot express my gratitude. I am proud of what you have achieved and I am excited for what our future together holds.

Chapter 1, in full, is a reprint of the material as it appears in ‘Chandler, M., Zilberman, N. V., and Sprintall, J. (2022). Seasonal to decadal western boundary current variability from sustained ocean observations. *Geophysical Research Letters*, 49, e2022GL097834, <https://doi.org/10.1029/2022GL097834>’. The dissertation author was the primary investigator and author of this paper.

Chapter 2, in part, is currently being prepared for submission for publication of the material by Chandler, M., Sprintall, J., and Zilberman, N. V. The dissertation author was the primary investigator and author of this paper.

Chapter 3, in full, is a reprint of the material as it appears in ‘Chandler, M., Zilberman, N. V., and Sprintall, J. (2024). The deep western boundary current of the Southwest Pacific Basin: Insights from Deep Argo. *Journal of Geophysical Research: Oceans*, 129, e2024JC021098, <https://doi.org/10.1029/2024JC021098>’. The dissertation author was the primary investigator and author of this paper.

## VITA

- |      |   |
|------|---|
| 2017 | Bachelor of Science in Oceanography, University of Otago  |
| 2018 | Bachelor of Science with First Class Honours in Geophysics, University of Auckland                              |
| 2020 | Master of Science in Oceanography, Scripps Institution of Oceanography at University of California San Diego    |
| 2025 | Doctor of Philosophy in Oceanography, Scripps Institution of Oceanography at University of California San Diego |

## ABSTRACT OF THE DISSERTATION

**Check it out! Examining western boundary currents using global ocean observations**

by

Mitchell Chandler

Doctor of Philosophy in Oceanography

University of California San Diego, 2025

Nathalie V. Zilberman, Chair

Janet Sprintall, Co-Chair

The subtropical western boundary currents (WBCs) in the upper-ocean and deep western boundary currents (DWBCs) in the deep-ocean are large-scale ocean currents located on the western side of the world's major ocean basins. These currents redistribute oceanic mass and heat around the globe and exert a sizeable influence on climate variability. However, due to their complexity, both WBCs and DWBCs are difficult to observe across multiple time and space scales. This dissertation therefore sets out to explore WBC and DWBC variability, and the impacts of this variability, from seasonal to multi-decadal and from local to basin scales. To achieve this goal, a suite of complementary global ocean observing platforms is used to study

the Agulhas Current in the Indian Ocean, and the East Australian Current (EAC), Kuroshio, and Southwest Pacific Basin DWBC in the Pacific Ocean.

Chapter 1 examines transport trends and seasonality in the Agulhas Current, EAC, and Kuroshio. Over the 16-year time series – longer than most other time series of subsurface WBC velocity – a decreasing trend in Kuroshio transport was found. There were no significant trends in Agulhas Current or EAC transport.

Chapter 2 examines the occurrence of subsurface marine heatwaves (MHWs) along a transect intersecting the Kuroshio and Kuroshio Extension. Using a novel 30-year synthetic temperature time series, subsurface MHWs were found to occur significantly more often during El Niño periods due to a strengthening of the Kuroshio Extension and its Southern Recirculation Gyre. This was a surprising result given that surface MHW occurrence along the transect is not influenced by El Niño.

Lastly, Chapter 3 examines flow pathways, turbulent mixing, and seasonality in the Southwest Pacific Basin DWBC. Deep Argo observations confirmed the existence of a previously hypothesised cyclonic circulation over the Kermadec Trench. While, inside the northern Kermadec Trench, seasonal heaving within the DWBC was discovered to be driven by local Ekman pumping at the surface. Finally, the deep-ocean salinity maximum was eroded as the DWBC exited the Kermadec Trench to the north, thus revealing the Louisville Seamount Chain collision zone as a previously unidentified region of enhanced deep-ocean mixing.

# Chapter 0

## Introduction

We can think of ocean currents as the arteries and veins of the climate system. Much like our arteries and veins transport blood around our body and help regulate our body temperature, these ocean currents – or oceanic arteries – transport large amounts of water and heat around the ocean and help regulate the global temperature. In this dissertation, I have focussed on a subsection of these ocean currents – western boundary currents (WBCs) – that are located along the ocean’s western boundaries.

The location of these WBCs can be explained by conservation of potential vorticity ( $Q$ ):

$$Q = \frac{f + \zeta}{H}$$

where  $f$  is planetary vorticity,  $\zeta$  is relative vorticity, and  $H$  is water column height (Colling et al. 2001; Talley et al. 2011). In the subtropics, surface winds induce Ekman pumping that compresses the water column beneath the Ekman layer. As  $\zeta$  is small in the ocean interior, this decrease in  $H$  must be balanced by a decrease in the magnitude of  $f$ , thereby resulting in an equatorward interior flow and a corresponding poleward return flow along an ocean boundary. This poleward return flow must occur at the western boundary as, using the Southern Hemisphere as an example and assuming constant  $H$ , a water parcel moving poleward has decreasing (more negative)  $f$  and therefore increasing  $\zeta$ . The negative  $\zeta$  input required to oppose this increase in  $\zeta$  can be produced by coastal friction at the western boundary, but not at the eastern boundary.

Similarly, in the deep-ocean, interior upwelling lifts the thermocline (i.e.  $H$  increases) which causes a poleward interior flow (i.e. magnitude of  $f$  increases) and a corresponding equatorward return boundary flow. As in the upper-ocean, this equatorward return flow must occur at the western boundary.

The subtropical WBCs are therefore poleward-flowing currents that redistribute oceanic mass and heat from low-latitudes to mid-latitudes. In doing so, these currents release heat and moisture to the atmosphere and thus exert a substantial influence on regional weather and climate (Bond and Cronin 2008; Minobe et al. 2008; Nakamura et al. 2008; Njouodo et al. 2018; Nonaka and Xie 2003; Qiu et al. 2014; Sasaki et al. 2012; Sugimoto et al. 2021). Furthermore, changes in these currents, as is expected under a warming climate (Oliver and Holbrook 2014; Sen Gupta et al. 2021; Yang et al. 2016), impact extreme climate variability. For example, intensification or changes in the path of WBCs can influence local sea-level (Archer et al. 2017; Diabat   et al. 2021; Ezer et al. 2013; Holbrook et al. 2011; Nhantumbo et al. 2020; Sasaki et al. 2014) and produce advection-driven marine heatwaves (Elzahaby et al. 2021; Li et al. 2020; Oliver et al. 2017, 2021). These impacts, and more, mean that WBCs often hold cultural, economic, and climatic importance for nearby countries (Ando et al. 2021).

The Deep Western Boundary Currents (DWBCs) lie much deeper in the ocean, thousands of metres below the sea surface. These currents transport cold, dense waters away from their high-latitude formation regions, filling the deep and abyssal ocean (Johnson 2008; Stommel and Arons 1959a). DWBCs are therefore a critical component of the meridional overturning circulation that redistributes heat, salt, carbon, nutrients, and oxygen around the globe (Sloyan et al. 2013; Talley 2013). However, the waters transported by these currents are initially formed near the surface. Cooling and brine rejection around Antarctica, and cooling and deep convection in the northern North Atlantic, increase the density of surface waters which then descend into the deep-ocean to form deep and bottom waters (Talley 2013; Talley et al. 2011). The properties of these deep and bottom waters are therefore influenced by climatic conditions at the time and location of their surface formation. As such, changes in deep and bottom water properties –

caused by changes in climate – are advected into the deep-ocean by DWBCs, impacting ocean heat uptake, dissolved oxygen content, sea level, and carbon storage (Desbruyères et al. 2016; Gunn et al. 2023; Kouketsu et al. 2011; Purkey and Johnson 2010, 2013; Purkey et al. 2019; Sloyan et al. 2013).

The oceanographic community therefore considers WBCs to be a crucial area of study (e.g. Ayoub et al. 2024; Morris et al. 2021; Savidge et al. 2024). However, WBCs are difficult to observe over multiple time and space scales due to their complex nature and substantial variability. As such, few long-term measurements of their subsurface structure exist (e.g. Liu et al. 2021; Oka et al. 2018; Ridgway et al. 2008; Wei et al. 2015). Mooring arrays can provide the highest temporal resolution measurements over the full vertical extent of a WBC, but these arrays are typically restricted to a few years at most and may not capture the entire width of the current (e.g. Beal et al. 2015; Bryden et al. 2005; Lee et al. 2001; Mata et al. 2000; Sloyan et al. 2016). Developing long-term WBC time series therefore often requires combining complementary ocean observing platforms (e.g. Beal and Eliot 2016; Goes et al. 2020; Lee et al. 2001; Ridgway et al. 2008; Zilberman et al. 2018).

Observing DWBCs is even more challenging. Extremely high pressures and frigid waters make it difficult to maintain high-quality measurements thousands of metres deep, with sensor drift rather common (e.g. Watts and Kontoyiannis 1990). Additionally, profiling instruments must be able to operate across large temperature and pressure gradients and withstand repeated pressure cycling (e.g. Roemmich et al. 2019b). Shipboard measurements, such as those from quasi-decadal repeat hydrographic surveys, have typically been used to study the deep-ocean (Sloyan et al. 2019). However, deep-ocean observations are sparse, with less than 10% of historical non-Argo temperature and salinity profiles extending below 2000-dbar (Roemmich et al. 2021). Deep-ocean moorings have also been deployed, but only in a limited number of locations for short periods of time (e.g. Meinen et al. 2017; Rudnick 1997; Voet et al. 2016; Whitworth III et al. 1999). DWBCs are therefore one of the least observed large-scale circulation features in the global ocean.

Nevertheless, the ability to observe WBCs beneath the sea surface and over long time periods is invaluable in helping to better understand WBC variability and dynamics, and in identifying how this variability impacts society at the ocean's western boundaries. Such subsurface observations are also crucial for verifying the representation of WBCs in the ocean and climate models used to project future changes. Developing a sustainable global ocean observing system is therefore one of the key challenges of the 2021–2030 United Nations Decade of Ocean Science for Sustainable Development (Challenge 7; Miloslavich et al. 2024).

In this dissertation, I have studied four different WBCs – the Agulhas Current, East Australian Current, and Kuroshio in the upper-ocean (shallower than 2000-m), and the Southwest Pacific Basin DWBC in the deep-ocean (deeper than 2000-m) – to address the following research questions:

- Are projected changes in WBC transport evident in long-term observations?
- Have conflicting warming and weakening trends within the Kuroshio caused any long-term changes in subsurface MHW occurrence?
- Do patterns of large-scale climate variability, such as the El Niño-Southern Oscillation, influence MHW occurrence in the Kuroshio Extension?
- Does the Southwest Pacific Basin DWBC exhibit a cyclonic recirculation over the entire Kermadec Trench?
- Is seasonality evident within the Southwest Pacific Basin DWBC?
- Can observations from Deep Argo floats be used to identify deep-ocean mixing hotspots?

To conduct this research, I utilised a suite of global ocean observing systems – including the High-Resolution eXpendable Bathymeter network (Goni et al. 2019), Argo program (Wong et al. 2020; Zilberman et al. 2023c), and satellites (Huang et al. 2021; Taburet et al. 2019) – alongside output from an eddy-resolving ocean reanalysis (Lellouche et al. 2021).

In Chapter 1 (Chandler et al. 2022a), I examined transport trends and seasonality in the Agulhas Current, East Australian Current, and Kuroshio using 16-year time series of cross-transect absolute geostrophic velocity between the surface and 1975-m deep. In Chapter 2 (in prep), I examined the occurrence of subsurface marine heatwaves in the upper 800-m using a 30-year subsurface temperature time series along a transect intersecting the Kuroshio and Kuroshio Extension. Finally, in Chapter 3 (Chandler et al. 2024), I examined flow pathways, turbulent mixing, and seasonality in the Southwest Pacific Basin DWBC using recent observations from Deep Argo floats that profile between the sea surface and 6000-m deep. The dissertation is concluded in Chapter 4.

# Chapter 1

## Seasonal To Decadal Western Boundary Current Variability From Sustained Ocean Observations

### 1.1 Abstract

Subtropical western boundary currents (WBCs) exert a substantial influence on regional climate. To improve WBC observations on seasonal-to-decadal timescales, and characterise their subsurface structure to 1975-m depth, we combine high-resolution expendable bathythermograph, Argo, and satellite altimetry observations in the Agulhas Current, East Australian Current, and Kuroshio. The resulting 16-year time series (2004–2019) show a weakening trend in Kuroshio transport, but no trend in Agulhas Current transport or East Australian Current transport. All three WBCs have stronger transport in summer, driven mostly by changes in current speed rather than current width. This unique subsurface view of WBC variability reveals changes in the path of the Kuroshio Extension on interannual timescales, and eddy variability in the Agulhas Current. Our work highlights how this application of a consistent methodology to combine complementary ocean observations allows for an unprecedented direct comparison of variability between WBCs.

## 1.2 Plain Language Summary

Western boundary currents are major ocean currents located on the western side of the world's oceans. These currents transport warm water towards the poles, which influences regional weather and climate. However, despite their importance, the fast speeds, high variability, and narrow width of these currents makes them difficult to observe. Here we examine the western boundary currents of the Indian Ocean (Agulhas Current) and Pacific Ocean (East Australian Current and Kuroshio) using measurements from three different ocean observing networks. The same method is applied to each current, allowing us to compare variability in the three currents. Between the start of 2004 and end of 2019 we find that transport of water has decreased in the Kuroshio but has not changed in the Agulhas or East Australian Current. We find changes in the path of the Kuroshio on interannual time scales, and shorter and irregular changes in the path of the Agulhas. On annual time periods, all three currents transport more water in summer than winter, which is related to faster speeds during the summer. These long subsurface time series can help us better understand how western boundary current variability impacts society at the western boundaries of the ocean.

## 1.3 Introduction

The subtropical western boundary currents (WBCs) are strong, poleward-flowing currents located on the western side of the major ocean basins (Figure 1.1). They redistribute oceanic mass and heat from low- to mid-latitudes and are vital in the release of heat and moisture to the atmosphere (Cronin et al. 2010; Hu et al. 2015), which influences weather patterns and regional climate (Minobe et al. 2008; Nakamura et al. 2008; Njouodo et al. 2018; Qiu et al. 2014; Sugimoto et al. 2021). Furthermore, changes in these currents impact extreme climate variability. Intensification or changes in the path of WBCs can produce advection-driven marine heatwaves (Oliver et al. 2017, 2021), likewise, variability in WBC strength and proximity to the coast are correlated with local sea-level variability (Archer et al. 2017; Diabaté et al. 2021; Ezer et al.

2013; Holbrook et al. 2011; Nhantumbo et al. 2020; Sasaki et al. 2014).

WBCs are expected to change under a warming climate (Oliver and Holbrook 2014; Sen Gupta et al. 2021; Yang et al. 2016). Most recently, Sen Gupta et al. (2021) project decreased Kuroshio, Gulf Stream, and Agulhas Current transport, and increased transport in the Brazil Current and extension regions of the East Australian Current (EAC) and Agulhas. However, challenges associated with measuring these currents across multiple time and space scales can cause large uncertainties, even in present-day conditions. Producing long-term transport estimates of these narrow, fast, and highly variable WBCs from a single observing platform is often not feasible. Mooring arrays provide the highest resolution measurements over the full vertical extent of WBCs, but are typically restricted to only a few years and do not always capture the full width of WBCs (e.g. Beal et al. 2015; Bryden et al. 2005; Lee et al. 2001; Mata et al. 2000; Sloyan et al. 2016). On the other hand, broadscale observing systems used in the ocean interior - such as Argo - do not adequately sample these narrow and swift WBCs (Riser et al. 2016; Send et al. 2010). Developing WBC time series therefore often requires combining complementary observing platforms (e.g. Beal and Eliot 2016; Goes et al. 2020; Lee et al. 2001; Liu et al. 2021; Ridgway et al. 2008; Zilberman et al. 2018).

In this study, we examine and compare seasonal-to-decadal variability in the WBCs of the Pacific Ocean (Kuroshio and EAC) and Indian Ocean (Agulhas Current) (Figure 1.1). Complementary High-Resolution eXpendable Bathymeterograph (HR-XBT), Argo, and satellite altimetry observations are combined over their shared 2004–2019 period to produce cross-transect geostrophic velocity estimates down to 1975-m depth at 1 month and 0.1° longitude resolutions (section 1.4). These estimates allow us to characterise the subsurface velocity structure over a longer time period than afforded by most other subsurface observations of WBCs. In addition, because a consistent methodology is used, variability is directly comparable between the WBCs. We examine the transport mean, trend, and annual cycle for each WBC, along with variability in the location of each WBC (section 1.5).

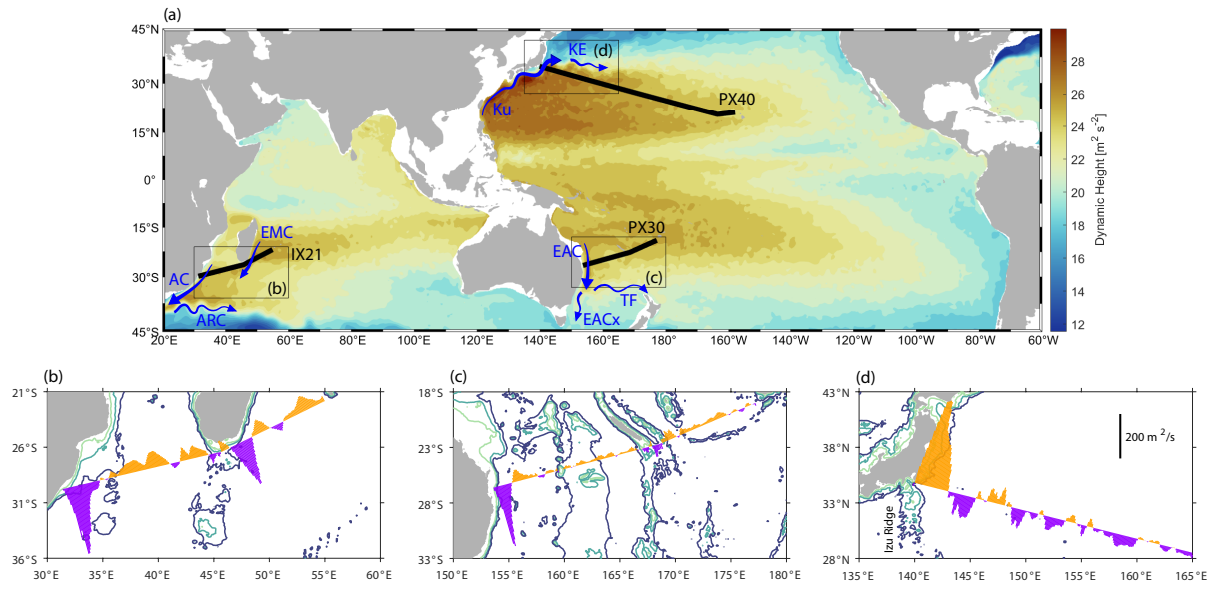


**Figure 1.1.** (a) 2004–2018 mean dynamic height at the surface relative to 1975-dbar from Argo (Roemmich and Gilson 2009), HR-XBT nominal transects (black), and associated western boundary currents (blue). Abbreviations are: AC - Agulhas Current; ARC - Agulhas Return Current; EMC - East Madagascar Current; EAC - East Australian Current; EACx - East Australian Current Extension; TF - Tasman Front; Ku - Kuroshio; KE - Kuroshio Extension. (b–d) 2004–2019 mean depth-integrated (0–1975-m) absolute geostrophic velocity across mean HR-XBT transects (b) IX21, (c) PX30, and (d) PX40. Depth contours are 200-m (green), 1000-m (blue-green), and 2000-m (blue). Izu Ridge (referred to in the text) is labelled in (d).

## 1.4 Data and Methods

### 1.4.1 Data

HR-XBT transects are occupied nominally four times a year and measure temperature to roughly 860-m depth with horizontal resolution of 6–10-km in WBC regions and 25–50-km in the ocean interior (Goni et al. 2019). The Agulhas Current is sampled by IX21 between Durban, South Africa and Port Louis, Mauritius; the EAC by PX30 between Brisbane, Australia and Suva, Fiji; and the Kuroshio by PX40 between Yokohama, Japan and Honolulu, Hawai’i (Figure 1.1). For each transect, temperature was objectively mapped onto 10-m depth intervals from 0–800-m and 0.1° intervals in longitude (Roemmich 1983; Zilberman et al. 2018). Corresponding salinity data was obtained using temperature-salinity relationships based on Argo data (Zilberman et al. 2018) and mapped at the same 0.1° resolution as the objectively mapped temperature. Argo

profiles to 1975-m depth were used for temperature and salinity (TS) profiles, and Argo trajectory velocities (Scanderbeg et al. 2019) were used to provide reference velocities at 1000-m depth. We also used the 2004–2018 mean Argo TS  $1/6^\circ \times 1/6^\circ$  gridded climatologies (Roemmich and Gilson 2009). The satellite altimetry product used was the daily-mean sea-level anomaly (SLA)  $1/4^\circ \times 1/4^\circ$  gridded product (Taburet et al. 2019). All data sets were for 2004–2019, covering the period since global Argo coverage was first achieved.

### 1.4.2 Computing Velocity Estimates

The method used to compute the velocity estimates was based on Zilberman et al. (2018), which the reader is referred to for complete details. Nominal transects (Figure 1.1) were determined as the linearised average of the 2004–2019 HR-XBT transects. The difference between Argo TS climatologies along individual HR-XBT transects and along the nominal transect were added to HR-XBT TS to produce corrected TS along the nominal transect. Corrected transects were extended from the reference depth ( $z_{ref}$ ) to 1975-m depth using the linear regression (Ridgway and Godfrey 1997; Zilberman et al. 2018):

$$h(z/1975) - h(z/z_{ref}) \approx m(z_{ref}) \cdot T_{z_{ref}} + c(z_{ref}), \quad 0 \leq z \leq z_{ref} \quad (1.1)$$

$$h(z/1975) \approx m(z) \cdot T_{z_{ref}} + c(z), \quad z_{ref} < z \quad (1.2)$$

where  $m$  and  $c$  are the regression coefficients, determined using Argo profiles within  $\pm 1.5^\circ$  latitude of the nominal transect that extend to at least 1975-m depth;  $T_{z_{ref}}$  is the temperature at  $z_{ref}$ ; and  $h(z/z_1)$  is the steric height ( $h$ ) at depth  $z$  relative to depth  $z_1$ . For each transect,  $z_{ref}$  (800-m for IX21 and PX30, 600-m for PX40) was selected based on where maximum correlations occurred between  $h$  and  $T_{z_{ref}}$  from Argo profiles (profile-averaged  $r > 0.8$  for all three transects). Steric height was then adjusted to be relative to 1975-m or the bottom depth if shallower ( $z_b$ ) using bathymetry from Smith and Sandwell (1997).

To obtain monthly estimates of  $h$ , daily-mean SLAs were interpolated onto the nominal

transect and the time-mean and trend over the HR-XBT measurement period (2004–2019 for IX21 and PX30, 2012–2019 for PX40; Figure 1.2) were removed to obtain the SLA temporal anomaly ( $SLA'$ ). Daily-mean  $SLA'$  was averaged over 7 days centered on the HR-XBT WBC sampling date. The  $h$  time-mean and trend at each coordinate ( $x$ ) and depth were removed to obtain the  $h$  temporal anomaly ( $h'$ ). A linear regression was calculated between  $h'$  and the 7-day average  $SLA'$  (Zilberman et al. 2018):

$$h'(z/z_b)(x) \approx m(x,z) \cdot SLA'(x) + c(x,z) \quad (1.3)$$

to obtain the regression coefficients  $m$  and  $c$ . Using these regression coefficients, equation 1.3 was applied to monthly-averaged  $SLA'$  to obtain monthly estimates of  $h'$ , which then had the  $h$  trend added back in over the HR-XBT measurement period and  $h$  time-mean added back in over 2004–2019. For PX40, where the HR-XBT record is shorter (Figure 1.2c), our transport estimates compared favourably with observations from the Kuroshio Extension System Study (Donohue et al. 2008, 2010) over June 2004 – October 2005 (Figure A1.1) when PX40 was not occupied. This favourable comparison provides confidence in our methodology.

Cross-transect geostrophic velocity ( $v_g$ ) was calculated from the thermal wind relation (e.g. Gill 1982) relative to a level of no motion at  $z_b$ . Argo trajectory velocities (Scandenberg et al. 2019) at the nominal parking depth of  $1000 \pm 100$ -dbar were used to obtain estimates of cross-transect absolute geostrophic velocity ( $v$ ) by referencing  $v_g$  to this level of known motion:

$$v(z,x,t) = v_g(z,x,t) - \overline{v_g(1000,x)} + \overline{v_\perp(x)} \quad (1.4)$$

where  $t$  is time, the overbar represents the 2004–2019 time-average, and  $v_\perp$  is the component of the Argo trajectory velocity perpendicular to the nominal transect. Velocities were referenced to the bathymetry in regions shallower than 1000-m. Mean Argo trajectory velocities were computed using  $1/2^\circ$  longitude  $\times$   $3^\circ$  latitude bins centered on the nominal transect (Zilberman et al. 2018). Because WBCs tend to follow the bathymetry near the coast, bins were aligned

parallel to the 1000-m isobath in WBC regions. Offshore of the WBCs, in the ocean interior, bins were meridionally oriented. The relatively sparse (Figure A1.2) and noisy Argo trajectory velocity data dominates the uncertainty, hence it was not possible to employ a time-varying  $v_{\perp}$  and  $v$  uncertainties were assigned based on the standard error of  $v_{\perp}$ . Our transport estimates for transects PX40 (Figure A1.1) and PX30 (Figure A1.3) were validated against independent measurements.

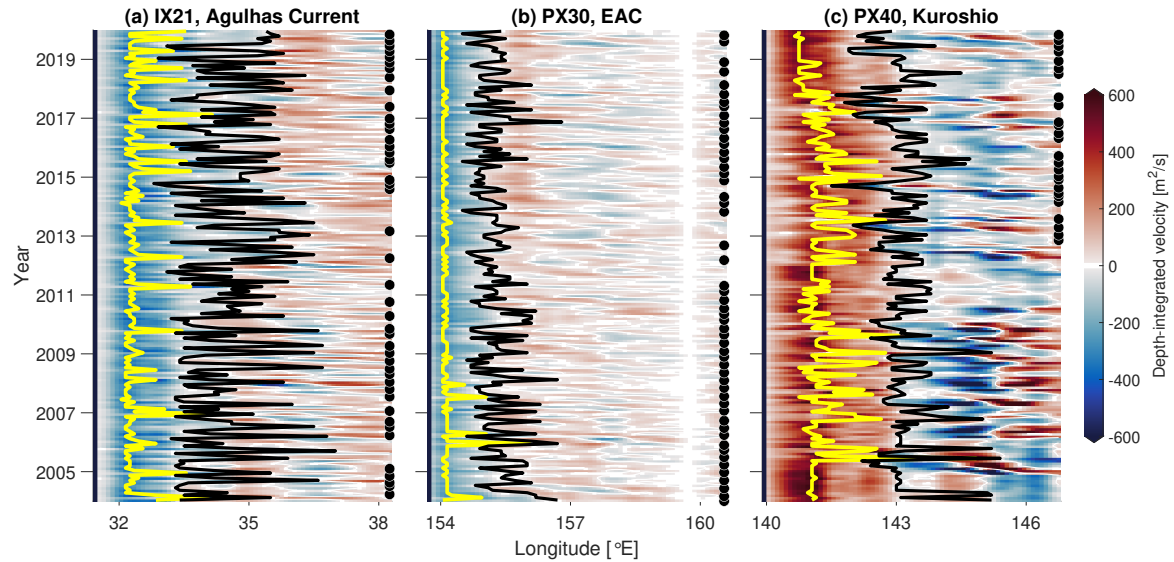


**Figure 1.2.** Longitude-time Hovmöller plots of depth-integrated (0–1975-m) absolute geostrophic velocity for the western section of HR-XBT transects (a) IX21, (b) PX30, and (c) PX40 sampling the Agulhas Current, East Australian Current (EAC), and Kuroshio respectively. Negative values (blue) indicate southward flow. Yellow and black lines identify the core and offshore edge of the western boundary current. Filled circles on the right indicate the dates of HR-XBT transects. Low depth-integrated velocities near 160°E (PX30) are due to a shallow seamount (Figure 1.1c).

### 1.4.3 Metrics of WBC Variability

Four metrics were used to compare WBCs: core longitude, core depth-integrated velocity, offshore edge deviations, and WBC transport (Figure 1.2). To compute these metrics,  $v$  was depth-integrated (0–1975-m) then smoothed along-transect using a triangle filter with size chosen based on the deformation radius in each region (LaCasce and Groeskamp 2020). The WBC core

was defined as where poleward depth-integrated velocities were maximum. The offshore edge was defined as where depth-integrated velocities changed from poleward to equatorward moving offshore from the WBC core. Offshore edge deviations were used, rather than WBC width, as nominal transects are not necessarily perpendicular to the WBC flow (Figure 1.1). The inshore edge was defined as the western edge of the transect. WBC transport (Figure A1.4) was the depth-integrated velocity horizontally integrated between the inshore and offshore edges. The uncertainty on the time-mean WBC transport was assessed using the  $v_{\perp}$  standard error out to the mean offshore edge. To compute annual cycles, time series were smoothed using a 3-month boxcar filter (Figure A1.4) and an average monthly climatology was formed. Annual cycle uncertainties are the standard error of the monthly mean. Significance levels were computed using an effective degrees of freedom determined from an integral time scale (Chapter 3 in Thomson and Emery 2014).

## 1.5 Results and Discussion

### 1.5.1 Mean Transport and Trends

Time-mean WBC transport between 0–1975-m over 2004–2019 was  $-45.0 \pm 5.2$  Sv ( $1 \text{ Sv} \equiv 1 \times 10^6 \text{ m}^3 \text{ s}^{-1}$ ) for the Agulhas,  $-20.9 \pm 1.8$  Sv for the EAC, and  $69.8 \pm 8.2$  Sv for the Kuroshio (Figures 1.3a–c). Our EAC estimate is comparable to nearby shorter period observations in the upper 2000-m of  $-19.5 \pm 2.0$  Sv at PX30 over 2004–2015 (Zilberman et al. 2018),  $-22.1 \pm 7.5$  Sv near  $27^\circ\text{S}$  over 2012–2013 (Sloyan et al. 2016), and  $-23.67$  Sv at  $30^\circ\text{S}$  over 1991–1993 (Mata et al. 2000). Our Agulhas cross-transect transport estimate is smaller than the upper 2400-m transport estimate of  $-76.2$  Sv made using direct current measurements near  $31^\circ\text{S}$  over a 9-month period in 1995 (Bryden et al. 2005). IX21 is located over a wider section of the continental shelf (Figure 1.1b) where, during 2004–2019, both Argo trajectory velocities and satellite altimetry surface geostrophic velocities were weaker than the stronger and more coherent poleward velocities associated with the Agulhas Current at the location of the Bryden

et al. (2005) mooring array (not shown). In the Kuroshio south of Japan, around 32°N, 133°E, a comparable full-depth transport of  $65 \pm 4$  Sv was found over 1993–1995 (Book et al. 2002).

Trends in the raw monthly transport time series over 2004–2019 were only significant (at the 95% confidence interval) in the Kuroshio, which showed a weakening poleward transport ( $-1.20 \pm 0.36$  Sv yr $^{-1}$ ; Figure A1.4c) with contributions from both a weakening core depth-integrated velocity ( $-4.66 \pm 2.64$  m $^2$  s $^{-1}$  yr $^{-1}$ ) and a narrowing of the offshore edge ( $-3.27 \pm 1.97$  km yr $^{-1}$ ). Wang et al. (2016) and Liu et al. (2021) also observed a weakening Kuroshio (upstream of Japan) over earlier 1993–2013 and 1998–2013 periods, respectively. This decreasing Kuroshio transport over recent decades has been hypothesised to be caused by a weakening of the negative North Pacific wind stress curl (Liu et al. 2021; Wang et al. 2016) which propagates baroclinic signals into the Kuroshio region, causing a shallower offshore pycnocline depth and relaxation of the pycnocline gradient across the Kuroshio (Liu et al. 2021; Sugimoto et al. 2010). Examination of our velocity trends over 2004–2019 (Figure A1.5) suggests that the offshore region of the poleward-flowing Kuroshio has experienced the largest decrease in velocity, consistent with this proposed mechanism. However, as these winds are known to demonstrate multi-decadal variability (Sugimoto et al. 2010; Trenberth et al. 2014) it is uncertain whether the recent decreasing transport trend will continue over future decades. EAC transport showed no significant trend ( $0.03 \pm 0.19$  Sv yr $^{-1}$ ; positive trend indicates weakening) which could be due to competing influences from a strengthening core depth-integrated velocity ( $-4.14 \pm 1.24$  m $^2$  s $^{-1}$  yr $^{-1}$ ) and narrowing of the offshore edge ( $-2.78 \pm 1.54$  km yr $^{-1}$ ). No other observational EAC transport trends have been published in the literature. However, modelling studies have examined past and future trends and suggest increased transport in the southern EAC and EAC extension (i.e. downstream of PX30) that is driven by strengthening of the positive South Pacific wind stress curl south of where the EAC separates from the coast, and a largely unchanged wind stress curl to the north (Cetina-Heredia et al. 2014; Oliver and Holbrook 2014). Agulhas transport also showed no significant trend ( $-0.21 \pm 0.37$  Sv yr $^{-1}$ ; negative trend indicates strengthening). Beal and Eliot (2016) found a non-significant transport trend downstream of IX21 over 1993–

2015, concluding that the Agulhas was instead broadening due to increased eddy activity. We also found a significant broadening trend in the Agulhas offshore edge ( $3.38 \pm 3.19 \text{ km yr}^{-1}$ ) at IX21, suggesting that this broadening may be happening over the length of the Agulhas Current.

### 1.5.2 Annual Cycles

All three WBCs demonstrate a significant transport annual cycle (Figures 1.3a–c), accounting for 14%, 25%, and 23% of the variance in the Agulhas, EAC, and Kuroshio respectively. In the southern hemisphere, the Agulhas and EAC are stronger in the austral summer and weaker in the austral winter. Agulhas transport peaks in March ( $-48.6 \pm 1.7 \text{ Sv}$ ) and is minimum in September ( $-41.4 \pm 1.5 \text{ Sv}$ ). EAC transport peaks in January ( $-23.6 \pm 0.8 \text{ Sv}$ ) and is minimum in July ( $-17.7 \pm 0.7 \text{ Sv}$ ). Other studies have shown comparable timing of the transport annual cycle in both the Agulhas (e.g. Beal and Eliot 2016; Beal et al. 2015) and EAC (e.g. Kerry and Roughan 2020; Ridgway and Godfrey 1997; Zilberman et al. 2018). The smaller amplitude at IX21 than observed further downstream (Beal and Eliot 2016; Beal et al. 2015) suggests that the amplitude of the Agulhas transport annual cycle increases poleward. In the northern hemisphere, the Kuroshio is stronger in the boreal summer, peaking in September ( $74.7 \pm 2.6 \text{ Sv}$ ), and weaker in the boreal winter, with a minimum in March ( $64.8 \pm 2.5 \text{ Sv}$ ). Stronger transport in summer has been observed in the upstream Kuroshio (e.g. Gilson and Roemmich 2002; Lee et al. 2001; Wei et al. 2015; Zhu et al. 2017), though often with minimum transport in autumn (Lee et al. 2001; Wei et al. 2015; Zhu et al. 2017). Observations of the Kuroshio annual cycle near PX40 have not been published before and we find a much larger amplitude than observed further upstream in the Kuroshio. The different timing of the annual cycle minimum compared to further upstream may be linked to PX40’s location east of Izu Ridge (Figure 1.1d) which blocks barotropic Rossby waves propagating westward from the ocean interior (Lee et al. 2001).

All three WBCs also demonstrate a significant annual cycle in core depth-integrated velocity (Figures 1.3d–f), accounting for 15%, 26%, and 33% of the variance in the Agulhas, EAC, and Kuroshio respectively. The timing of these annual cycles are consistent with those for

WBC transport, with poleward core depth-integrated velocity at a maximum (minimum) in April (October) in the Agulhas, January (July) in the EAC, and August (February) in the Kuroshio. In contrast, annual cycles are not clear in the offshore edge deviations (Figures 1.3g–i). The offshore edge of the Agulhas and Kuroshio hint at an annual cycle but remain close to the mean for almost all months and the annual cycles are not significant, with each explaining only 4% of the variance. The EAC offshore edge demonstrates a significant quasi semiannual cycle, with an offshore maximum in February and onshore maximum in October, that explains 13% of the variance.

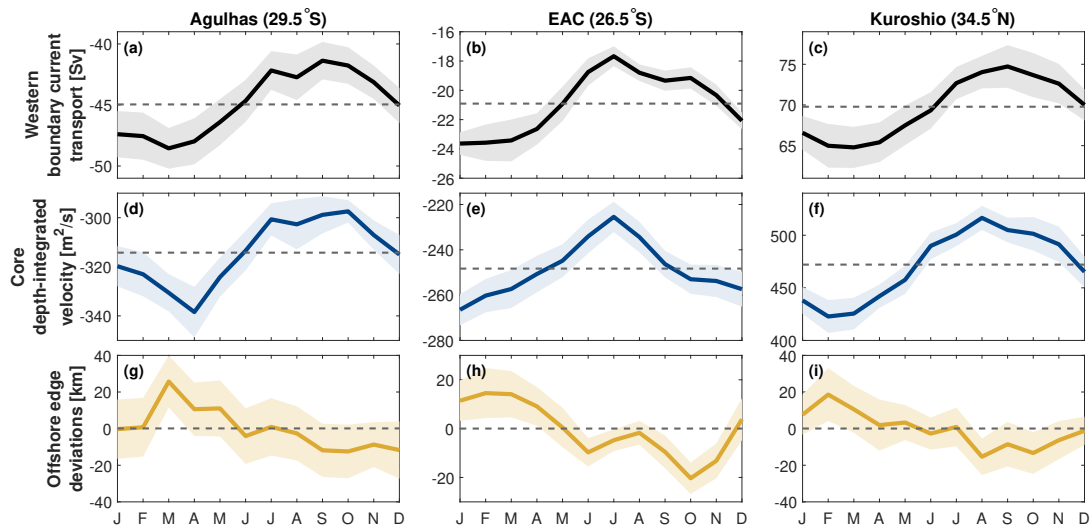


**Figure 1.3.** Annual cycles in the Agulhas Current (left), East Australian Current (EAC, middle), and Kuroshio (right) for: (a–c) western boundary current transport (positive values northward); (d–f) core depth-integrated velocity (positive values northward); (g–i) offshore edge deviations (positive values eastward). Shading is  $\pm 1$  standard error. Dashed line is the 2004–2019 mean.

Similarities between the WBC transport and core depth-integrated velocity annual cycles, and the lack of any clear annual cycle in offshore edge deviations, suggest that, for all three WBCs, seasonality in WBC transport is driven more by corresponding changes in the speed of the WBC core rather than the width of the WBC. In other words, when the core of the WBC is flowing faster in the summer, the volume transport of the WBC is larger. The converse is true in winter. Whether the similar transport annual cycles are driven by similar forcing mechanisms

remains unclear. In the Agulhas, the transport annual cycle is driven by baroclinic adjustment to near-field winds, with the wind-driven barotropic component small (Hutchinson et al. 2018). In the Kuroshio, the annual cycle of velocity above 500-m is dominated by local wind stress, with wind stress curl west of the Izu Ridge (Figure 1.1d) controlling the barotropic response (Lee et al. 2001; Zhang et al. 2021). The relationship between the EAC annual cycle and wind forcing remains poorly understood (Kerry and Roughan 2020), although given the similarities in the annual cycles between the three WBCs we may expect local wind stress to be important.

### 1.5.3 Temporal Variability in the Location of the WBC

Large offshore displacements in the core of the Agulhas Current occurred irregularly at IX21 (Figure 1.2a). Following previous studies (e.g. Eliot and Beal 2015; Krug and Tournadre 2012; Leber and Beal 2014; Rouault and Penven 2011), we defined Natal Pulses (NPs) as when the core longitude meandered offshore by more than 1 standard deviation from the mean (Figure 1.4a). The SLA composite for months in which NPs were identified (Figure 1.4e) shows an anomalous cyclonic circulation near the coast and an anomalous anticyclonic circulation offshore. Twenty-one NPs were identified over the 16-year record, varying between 0–3 events per year and with an average of 1.3 per year. This rate is slightly lower than the average of 1.5–2 per year further downstream (Eliot and Beal 2015; Krug and Tournadre 2012; Rouault and Penven 2011), but slightly higher than the approximately 1 per year near IX21 (Rouault and Penven 2011). Our velocity cross-section composites at IX21 (Figures 1.4b–d) show poleward flow in the Agulhas is stronger and closer to the coast under normal conditions (maximum poleward velocity of  $0.66 \text{ m s}^{-1}$ ; Figure 1.4c) compared to when a NP is present (maximum poleward velocity of  $0.51 \text{ m s}^{-1}$ ; Figure 1.4b). In the NP composite (Figure 1.4b) there are two separate cores with poleward velocities greater than  $0.1 \text{ m s}^{-1}$  down to 950-m depth. This two-core structure is likely an artefact of the monthly sampling resolution, as any given month may experience both NP and non-NP conditions. For example, Eliot and Beal (2015) found NPs took between 23–44 days to cross their mooring array. The surface-intensified recirculation centered around  $36^\circ\text{E}$  is likely

tied to the anticyclonic surface anomaly (Figure 1.4e). Under normal conditions (Figure 1.4c), poleward velocities greater than  $0.1 \text{ m s}^{-1}$  reached 1000-m depth.

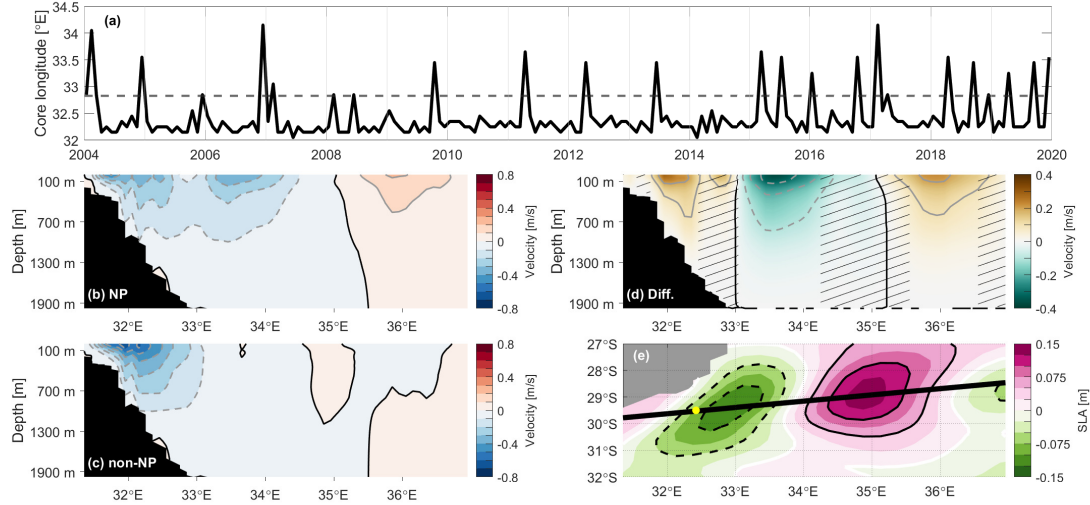


**Figure 1.4.** (a) Monthly time series of Agulhas Current core longitude. Dashed line indicates  $+1$  standard deviation from the mean. (b) Absolute cross-transect geostrophic velocity composite for Natal Pulse (NP) events. Negative velocities are poleward. (c) As in (b) but for non-NP periods. (d) Difference between the two composites (NP minus non-NP). Hatching indicates where differences are not significant at the 95% confidence level. For (b–d) the black contour denotes  $0 \text{ m s}^{-1}$  and the solid and dashed grey contours are at intervals of  $+0.1$  and  $-0.1 \text{ m s}^{-1}$ . (e) Composite of monthly sea level anomaly (SLA) for NP months. The black line is the IX21 nominal transect and the yellow marker the mean location of the Agulhas Current core. The white SLA contour denotes 0-m and the solid and dashed black SLA contours are at intervals of  $\pm 0.05\text{-m}$  and  $-0.05\text{-m}$ .

In the North Pacific, the Kuroshio-Kuroshio Extension (KE) system is known to vary between dynamically stable and unstable states on decadal time scales due to a negative feedback with the North Pacific wind stress curl (Qiu and Chen 2005, 2010; Qiu et al. 2020, 2014). Qiu et al. (2014) introduced the Kuroshio Extension Index (KEI; Figure A1.6), which uses satellite altimetry to provide a single measure of this low frequency variability in the KE. Satellite observations suggest that the Kuroshio typically passes through a gap in the Izu Ridge (Figure 1.1d) closer to the coast during a stable dynamic state (positive KEI) and over the ridge further offshore during an unstable dynamic state (negative KEI) (Qiu and Chen 2005). Our composites

of the velocity cross-section at PX40, downstream of the Izu Ridge, show that the structure of the poleward-flowing Kuroshio is similar during both positive and negative KEI states (Figure 1.5). These similarities are indicative of the convergence of the different Kuroshio pathways downstream of the Izu Ridge (Kawabe 1995). Likewise, both WBC transport and maximum poleward velocities were statistically similar (at the 95% confidence level) between the two composites ( $70.5 \text{ Sv}$  and  $0.89 \text{ m s}^{-1}$  for the positive KEI compared to  $72.9 \text{ Sv}$  and  $0.83 \text{ m s}^{-1}$  for the negative KEI). The largest differences occurred further offshore, with significantly stronger equatorward velocities between  $144.05\text{--}145.05^\circ\text{E}$  and poleward velocities between  $145.85\text{--}147.45^\circ\text{E}$  in the negative KEI composite (Figures 1.5b and 1.5c). In an unstable dynamic state the KE is located further south, therefore closer to PX40, and exhibits greater meandering (Qiu and Chen 2010; Qiu et al. 2014). As such, meanders in the KE more readily intersect PX40. The opposite occurs during a stable dynamic state.

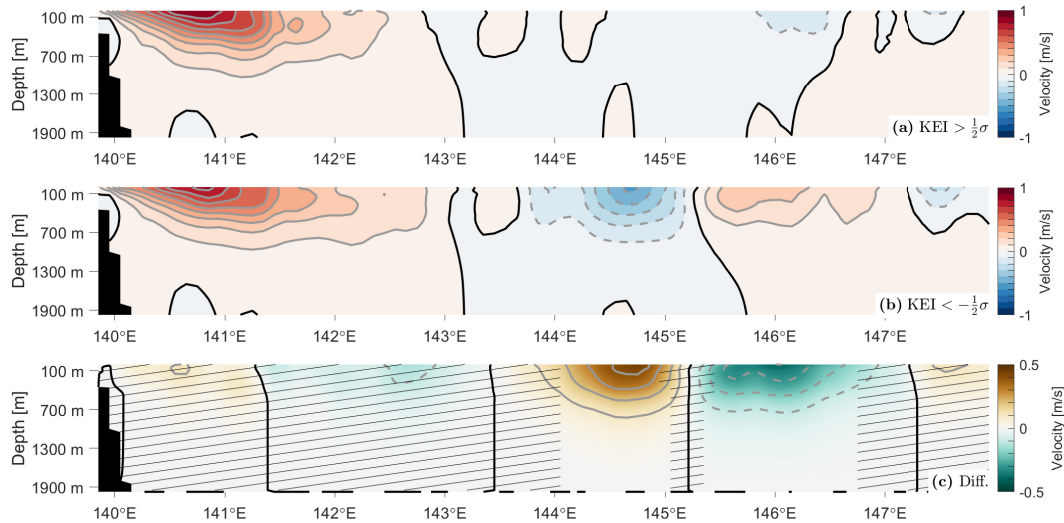


**Figure 1.5.** (a) Absolute cross-transect geostrophic velocity composite for periods when the Kuroshio Extension Index (KEI) is positive ( $> \frac{1}{2}\sigma$ ). Positive velocities are poleward. (b) As in (a) but for negative KEI ( $< -\frac{1}{2}\sigma$ ). (c) Difference between the two composites (positive minus negative). Hatching indicates where differences are not significant at the 95% confidence level. For (a–c) the black contour denotes  $0 \text{ m s}^{-1}$  and the solid and dashed grey contours are at intervals of  $+0.1$  and  $-0.1 \text{ m s}^{-1}$ .

In contrast to both the Agulhas and Kuroshio, the location of the EAC core (Figure 1.2b) was relatively stable at the location of PX30 which coincides with where the EAC jet is most coherent (Kerry and Roughan 2020).

## 1.6 Conclusions

We examined seasonal-to-decadal variability in the subsurface signature of the Agulhas Current, EAC, and Kuroshio using 16-year time series produced from sustained ocean observations. Few other observational studies of these WBCs span time periods of a similar length or longer (e.g. Beal and Elipot 2016; Liu et al. 2021; Oka et al. 2018; Ridgway et al. 2008; Wei et al. 2015). Uniquely, our application of a consistent methodology permits direct comparison of velocity and transport variability in the upper 1975-m of WBCs. Given the sparse distribution of Argo data, we are unable to resolve any trends or variability in the barotropic signal using Argo trajectories and therefore a constant reference level was used. However, the envisioned increase in Argo sampling density in WBC regions (Roemmich et al. 2019a) may allow for a time-varying reference level that addresses these limitations in the future.

Decreased Kuroshio transport and no significant change in EAC or Agulhas transport were observed over 2004–2019. As noted above, there are relatively few long time series that can provide comparisons with these observed trends. Our time series provide a baseline for studying future changes and therefore contribute toward addressing this long-term observations knowledge gap. Transport annual cycles were remarkably similar in all three WBCs, with poleward transport stronger in the summer and weaker in the winter. Our results suggest that this summertime transport maximum is driven by an increase in current speed rather than current width. Importantly, the length of our time series provide enhanced confidence in the robustness of these observed annual cycles.

Incorporating subsurface observations allows us to expand upon sea surface satellite observations of variability in the path of WBCs (e.g. Krug and Tournadre 2012; Qiu and Chen

2005, 2010; Qiu et al. 2014; Rouault and Penven 2011). Observing the vertical structure of velocity down to 1975-m depth provides context for these satellite altimetry studies as the subsurface flow is not required to follow the surface expression. Variability in the Agulhas core longitude was dominated by NPs that occurred at an average rate of 1.3 per year. The subsurface velocity structure showed that, during NPs, the Agulhas was slower near the coast and faster offshore, with differences of  $0.1 \text{ m s}^{-1}$  as deep as 800-m when compared with normal conditions. At PX40, the poleward-flowing Kuroshio was found to be similar during both positive and negative KEI states, however differences in the meandering of the KE were evident further offshore with  $0.1 \text{ m s}^{-1}$  differences also extending to 800-m depth. Variability in WBC location may influence ocean temperature advection and air-sea interactions, with important implications for both ocean temperature and regional weather patterns (e.g. Oliver et al. 2021; Sugimoto et al. 2021).

Our work demonstrates the ability of the Zilberman et al. (2018) method to provide a consistent procedure for examining and comparing subsurface variability in WBCs. The time series we produced are longer than most other observations in these WBCs and therefore provide enhanced confidence in the robustness of observed variability. Because the high spatial resolution observations needed to observe WBCs are provided by HR-XBT transects, which are present in all ocean basins (Goni et al. 2019), this method can be applied to illuminate variability in other boundary currents. Furthermore, incorporating autonomous underwater gliders - which provide sustained and high spatial resolution observations from the surface down to 1000-m depth (Rudnick 2016; Testor et al. 2019) - in place of HR-XBT transects could allow the method to be applied in other regions. These long-term observations of WBCs will be important for studying the impact of WBC variability on, for example, marine heatwaves and local sea-level variability.

## **1.7 Open Research**

The HR-XBT data is made available by the Scripps Institution of Oceanography HR-XBT program (IX21 - <http://www-hrx.ucsd.edu/ix15.html>; PX30 - <http://www-hrx.ucsd.edu/px31.html>; PX40 - <http://www-hrx.ucsd.edu/px40.html>). The Argo data is collected and made available by the International Argo Program and the national programs that contribute to it (<https://doi.org/10.17882/42182>). The Argo temperature and salinity climatologies are available from [http://sio-argo.ucsd.edu/RG\\_Climatology.html](http://sio-argo.ucsd.edu/RG_Climatology.html). The satellite altimetry products are available from the EU Copernicus Marine Service (<https://doi.org/10.48670/moi-00148>). Bathymetry data is available through the NOAA National Centers for Environmental Information (<https://doi.org/10.7289/V5J1012Q>). The first surface mode deformation radius dataset is available from [https://figshare.com/articles/dataset/Rossby\\_Deformation\\_Radius/14336759](https://figshare.com/articles/dataset/Rossby_Deformation_Radius/14336759). Data from the Kuroshio Extension System Study can be accessed through the program websites ([http://www.po.gso.uri.edu/dynamics/kess/CPIES\\_data.html](http://www.po.gso.uri.edu/dynamics/kess/CPIES_data.html) and <https://uskess.whoi.edu/overview/dataproducts/>). Scripts for building the velocity estimates and conducting the analysis are publicly available at MC's GitHub ([https://github.com/mlchandler/wbc\\_sustained\\_obs](https://github.com/mlchandler/wbc_sustained_obs)). The velocity time series produced from this research are permanently available through Zenodo (<https://doi.org/10.5281/zenodo.5851311>).

## **1.8 Acknowledgements**

The authors thank Lisa Lehmann and Megan Scanderbeg for their assistance with some of the data processing, Bo Qiu for providing the KEI, Kathleen Donohue for providing data from the Kuroshio Extension System Study, and Bernadette Sloyan for providing the EAC mooring array data. The authors also thank two anonymous reviewers for their comments which helped to improve the manuscript. This study was supported by NOAA's Global Ocean Monitoring and Observing Program. NZ and JS were supported by the NOAA Global Ocean Monitoring and Observing Program through Award NA20OAR4320278. NZ was supported by NOPP (NOAA

grant NA18OAR0110434). MC received financial support from Fulbright New Zealand.

This chapter, in full, is a reprint of the material as it appears in ‘Chandler, M., Zilberman, N. V., and Sprintall, J. (2022). Seasonal to decadal western boundary current variability from sustained ocean observations. *Geophysical Research Letters*, 49, e2022GL097834, <https://doi.org/10.1029/2022GL097834>’. The dissertation author was the primary investigator and author of this paper.

## 1.A Supplementary Figures for Chapter 1

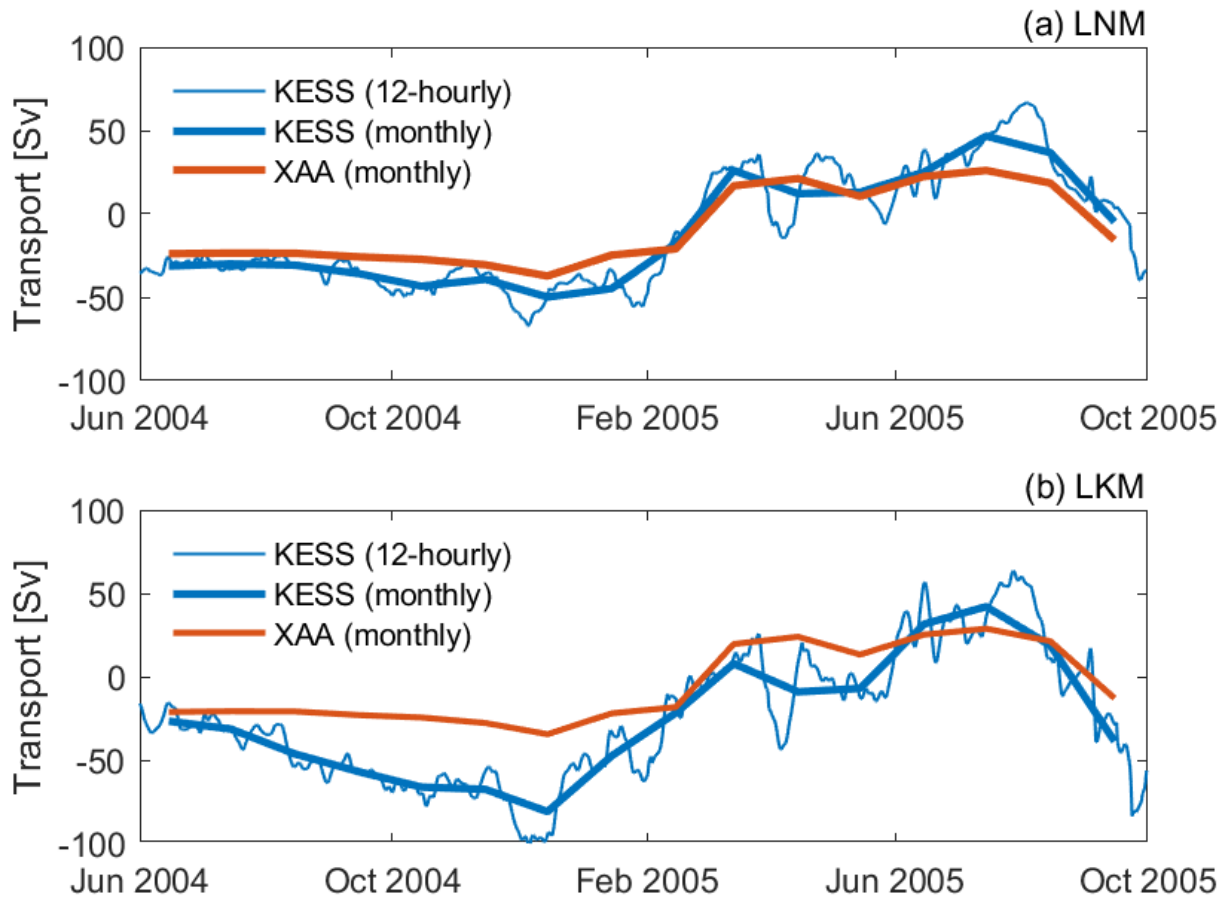


**Figure A1.1.** Cross-transect volume transport across transect PX40 between 0–1975-m and 143.95–148.35°E from our monthly estimates (XAA) and from the Kuroshio Extension System Study (KESS, 12-hourly and monthly) computed using **(a)** geostrophic velocity relative to a level-of-no-motion (LNM) at 1975-m, and **(b)** absolute geostrophic velocity referenced to a level-of-known-motion (LKM) determined using Argo trajectories at 1000-m (XAA) and bottom velocities from current meters (KESS). Positive values are northward.

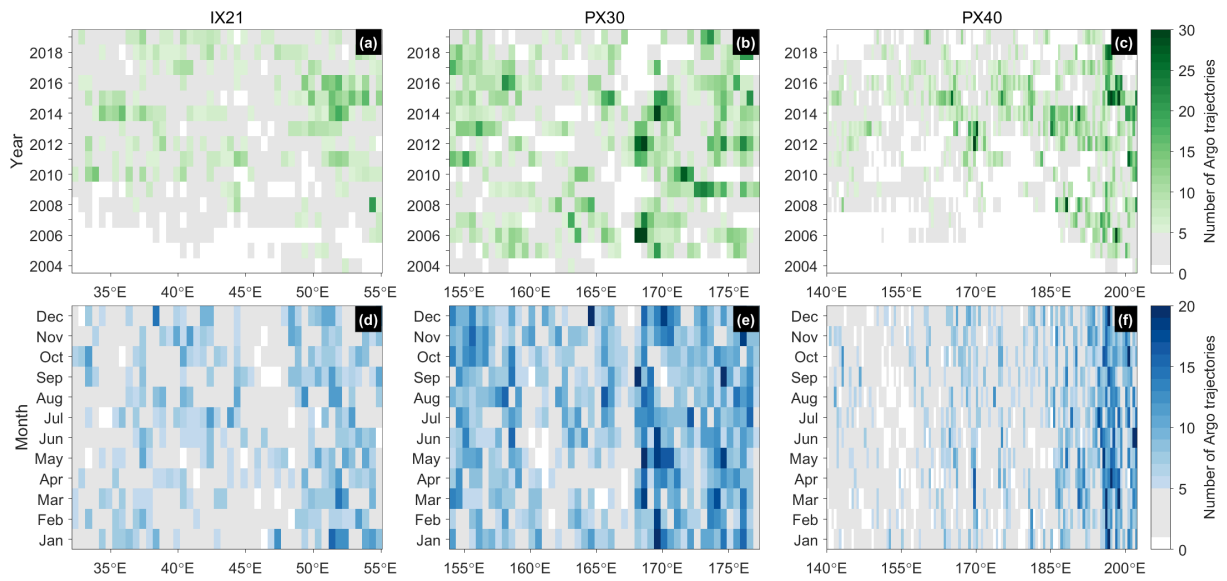


**Figure A1.2.** (a–c) Number of Argo trajectory measurements between 900–1100-dbar each year in each bin for HR-XBT transects (a) IX21, (b) PX30, and (c) PX40. (d–f) Number of Argo trajectory measurements between 900–1100-dbar each month over the full 2004–2019 period in each bin for HR-XBT transects (d) IX21, (e) PX30, and (f) PX40. Bins with no measurements are coloured white and bins with less than 5 measurements are coloured grey.

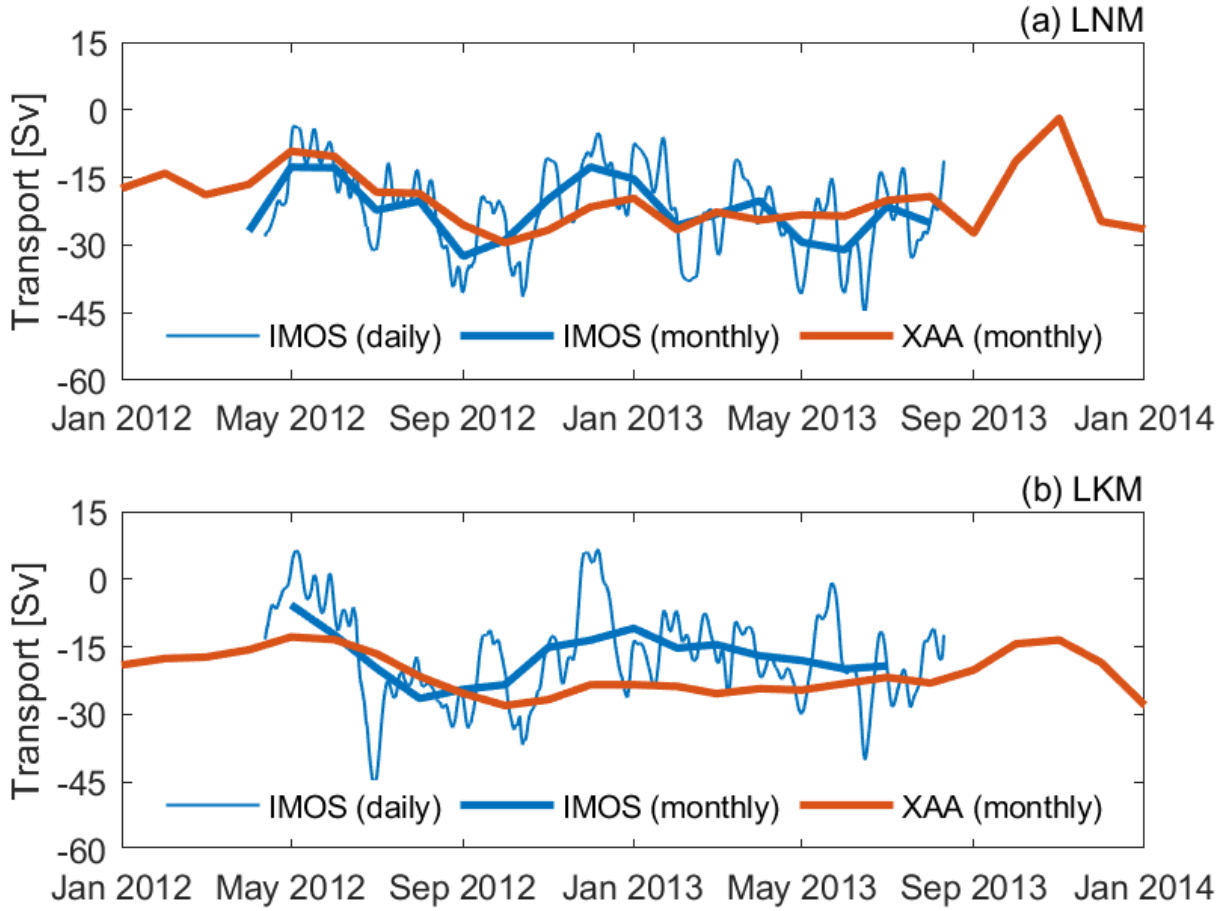


**Figure A1.3.** (a) Comparison between our monthly estimates of geostrophic volume transport between  $153.75\text{--}155.25^\circ\text{E}$  across transect PX30 (XAA) and total volume transport between  $153.77\text{--}155.30^\circ\text{E}$  across a mooring array at  $27^\circ\text{S}$  (IMOS, daily and monthly-averaged). Both XAA and IMOS transports are computed using velocities normal to transect PX30 between 0–1975-m and relative to a level-of-no-motion (LNM) at 1975-m. Negative values are southward. Mooring data is from Sloyan et al. (2016). (b) As for (a) but both monthly time series are smoothed using a 3-month boxcar filter and computed using velocities referenced to a level-of-known motion (LKM) determined using Argo trajectories at 1000-m (XAA) or from direct measurements (IMOS).

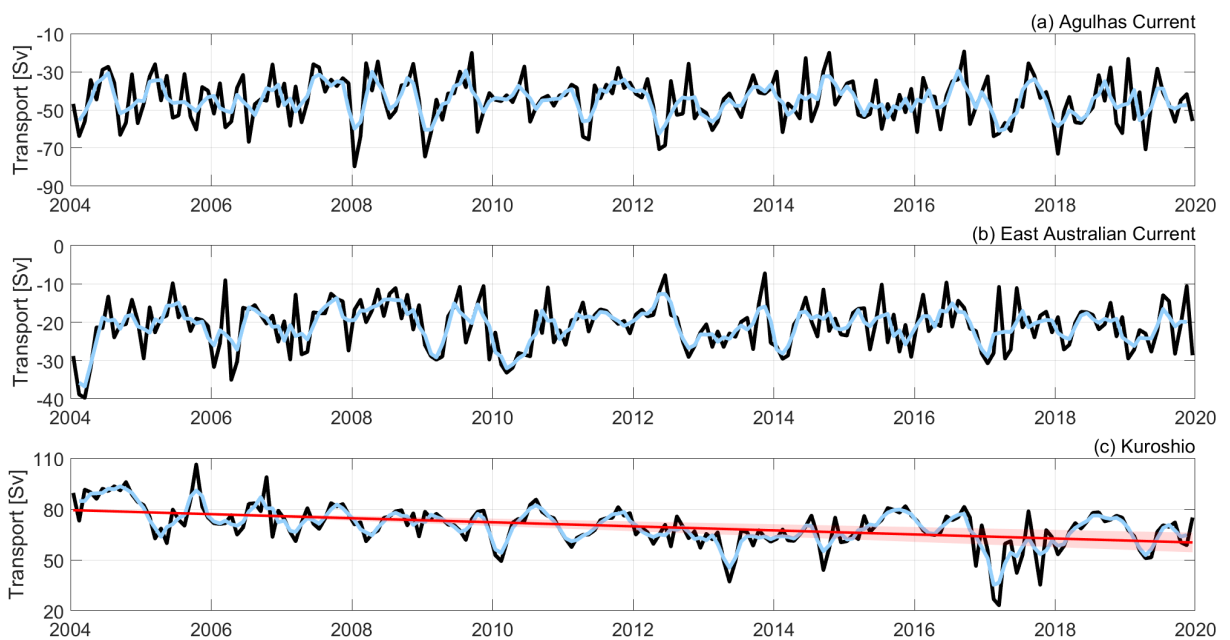


**Figure A1.4.** Time series of monthly western boundary current transport (black) and monthly western boundary current transport smoothed using a 3-month boxcar filter (blue) between the surface and 1975-m computed using absolute geostrophic velocities for the (a) Agulhas Current, (b) East Australian Current, and (c) Kuroshio. Positive transport is northward. Trend (red line with 95% confidence interval shading) is shown for the Kuroshio, where a significant weakening transport trend was found ( $-1.20 \pm 0.36 \text{ Sv yr}^{-1}$ ). Transport trends were not significant for the Agulhas Current or East Australian Current.

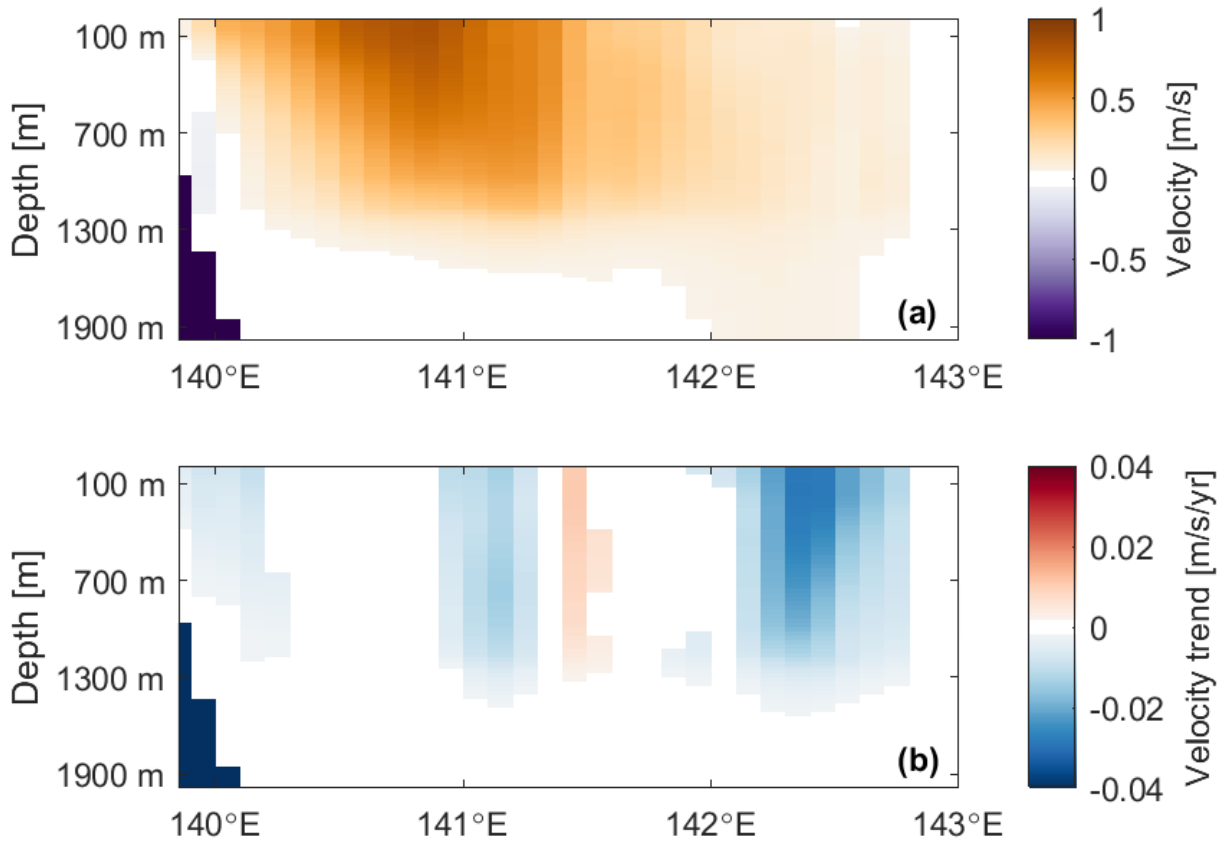


**Figure A1.5.** Cross-transect absolute geostrophic velocity **(a)** time-mean and **(b)** trend over 2004–2019 in the poleward-flowing Kuroshio across transect PX40. Trends are only shown where they are significant at the 95% confidence interval. Positive values are northward.

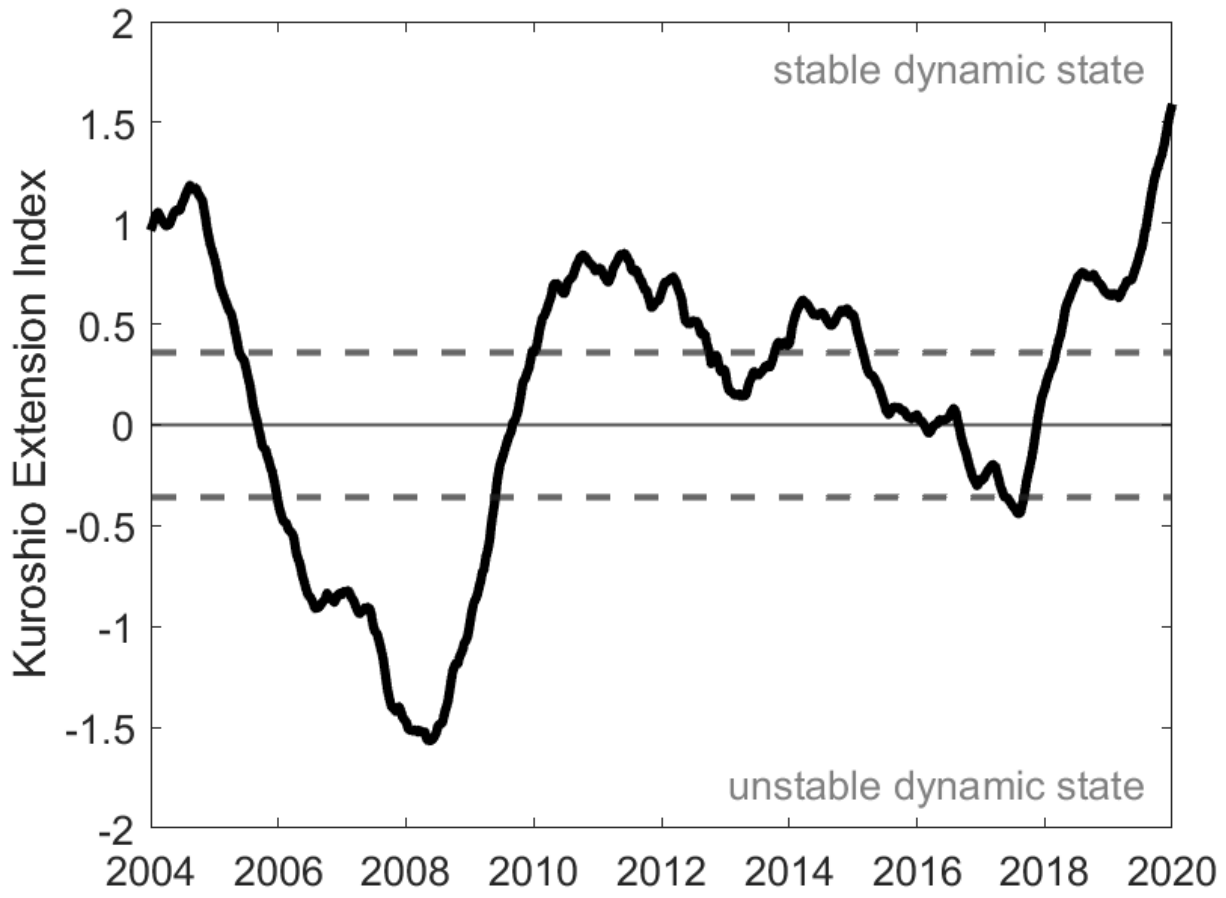


**Figure A1.6.** Weekly time series of the Kuroshio Extension Index smoothed using a 53-week boxcar filter. Dashed lines represent  $\pm \frac{1}{2}$  standard deviation.

# **Chapter 2**

## **ENSO Influences Subsurface Marine Heatwave Occurrence In The Kuroshio Extension**

### **2.1 Abstract**

Extreme ocean temperature events, also known as marine heatwaves (MHWs), can have devastating consequences for ecosystems, communities, and economies. However, the ability to understand and predict MHWs beneath the sea surface is limited by a scarcity of subsurface observations. Here, we combined in situ temperature observations from a High-Resolution eXpendable BathyThermograph (HR-XBT) transect in the Northwest Pacific Ocean with satellite observations to produce a multi-decadal (1993 to 2022) subsurface temperature time series with 10-day temporal resolution. This novel time series was used to examine MHWs between the surface and 800-m deep in the Kuroshio-Kuroshio Extension region east of Japan. The length of this 30-year time series also permitted exploration of long-term trends and interannual variability in subsurface temperature. Variability in the Kuroshio-Kuroshio Extension system is found to exert a strong control on the occurrence of MHWs along this transect. Throughout the water column, Kuroshio warming drove a significant increase in Kuroshio MHW days per year. Notably, the largest mean MHW event intensities were observed in the subsurface at every location along the transect rather than at the surface. Strengthening of the Kuroshio Extension

and its Southern Recirculation Gyre during El Niño drove a significant increase in subsurface MHWs where the intensified current system intersected the transect. In contrast, surface MHW occurrence along the transect was not influenced by the El Niño-Southern Oscillation (ENSO). Clearly, relying only on sea surface temperature observations does not provide the full picture of MHWs in this region.

## 2.2 Plain Language Summary

Marine heatwaves (MHWs) – the ocean equivalent to the atmospheric heatwaves experienced on land – are periods of unusually warm water. These events have the potential to cause devastating economic impacts. Although MHWs occur throughout the ocean, most studies have focussed only on events at the sea surface due to the availability of long-term satellite measurements. Fewer long-term time series exists beneath the sea surface. Here, we combined long-term satellite measurements of the surface with repeated subsurface temperature measurements collected along a shipping route in the Northwest Pacific Ocean to produce a new temperature time series between the surface and 800-m deep. This multi-decadal time series was used to examine subsurface MHWs in the Kuroshio and Kuroshio Extension – strong ocean currents east of Japan. We found that, since 1993, warming temperatures in the Kuroshio have caused an increase in the number of subsurface MHW days per year. In addition, subsurface MHWs occurred more often during El Niño conditions due to a strengthening of the Kuroshio Extension. Knowledge that subsurface MHWs along this route occur more often during El Niño could aid in designing and implementing MHW adaptation plans.

## 2.3 Introduction

Marine heatwaves (MHWs) are prolonged periods of anomalously warm water (Hobday et al. 2016). These events can have devastating consequences for marine ecosystems (Cavole et al. 2016; Mills et al. 2013; Smale et al. 2019; Smith et al. 2023, 2021). Such extreme ocean

temperatures can also impact regional weather by influencing surface air temperature, humidity, winds, and/or precipitation (Pathmeswaran et al. 2022; Sugimoto et al. 2021; Tochimoto and Iizuka 2022). The potential economic impacts of MHWs can thus reach into the billions of dollars (Smith et al. 2021).

Due to the extensive spatial and temporal coverage provided by sea surface temperature (SST) observations, most MHW studies have focussed only on events at the sea surface. Yet SST variability is often not representative of subsurface temperature variability. Differences between surface and subsurface temperature arise, in part, because of the different forcing mechanisms driving temperature variability, and consequently MHWs, at the surface and in the subsurface (e.g. Elzahaby et al. 2021; Großelindemann et al. 2022; Xu et al. 2024). As such, subsurface MHWs can occur independently of an anomalous warming signal at the sea surface, and can have greater intensities compared to surface MHWs (Hu et al. 2021; Schaeffer and Roughan 2017; Schaeffer et al. 2023). Subsurface-intensification is also thought to be a common feature of surface MHWs in western boundary current (WBC) regions (Elzahaby and Schaeffer 2019; Zhang et al. 2023). Ecosystem impacts of these MHWs are therefore often amplified at depth where many commercially-important species are found (e.g. Cai et al. 2020; Mills et al. 2013). As such, the ability to observe, understand, and predict MHW events below the sea surface is a priority for the MHW community (Oliver et al. 2021).

In this study, we focus on MHWs in the Kuroshio, the WBC of the North Pacific Ocean. The Kuroshio holds cultural, economic, and climatic importance for nearby countries (Ando et al. 2021) as it is an important spawning and nursery area for fish (Fujioka et al. 2018; Kitagawa et al. 2010; Yatsu 2019) and exerts an important influence on regional weather and climate (Bond and Cronin 2008; Nonaka and Xie 2003; Qiu et al. 2014; Sasaki et al. 2012; Sugimoto et al. 2021). Over recent decades, warming has been observed at the surface along the path of the Kuroshio (Wang et al. 2016) and in the subsurface at 137°E (Oka et al. 2017). This warming has occurred despite a decreasing trend in Kuroshio mass transport (Chandler et al. 2022a; Liu et al. 2021; Wang et al. 2016), with surface warming instead being driven by warming of source

waters (Wang et al. 2016). Surface warming is projected to drive an increase, relative to a fixed baseline, in surface MHW occurrence within the Kuroshio and Kuroshio Extension over the course of the century (Kawakami et al. 2024). However, comparable trends in subsurface MHWs have yet to be demonstrated. The El Niño-Southern Oscillation (ENSO) has also been shown to influence MHW occurrence in the North Pacific Ocean (e.g. Gregory et al. 2024). Although recent studies indicate essentially no relationship between ENSO and surface MHW occurrence in the Kuroshio-Kuroshio Extension region (Gregory et al. 2024; Holbrook et al. 2019; Sen Gupta et al. 2020), it is unknown whether this same weak relationship extends into the subsurface.

Multi-decadal and high-resolution measurements are essential for observing, understanding, and predicting MHWs. Yet such time series are rare in the ocean's subsurface. The High-Resolution eXpendable BathyThermograph (HR-XBT) network provides measurements of ocean temperature between the surface and more than 800-m deep along fixed transects, with some transects having been occupied for more than 30 years (Goni et al. 2019). These subsurface temperature observations are at high spatial resolutions ( $O(1\text{--}10)\text{-km}$ ), but relatively low temporal resolutions (nominally four occupations per year). However, HR-XBT and sea level anomaly (SLA) observations have a close relationship that can be exploited to enhance the temporal resolution of these subsurface temperature time series (Chandler et al. 2022a; Gilson et al. 1998; Ridgway et al. 2008; White and Tai 1995; Willis et al. 2003).

Here, we examine the occurrence of subsurface MHWs along a HR-XBT transect intersecting the Kuroshio and Kuroshio Extension using a novel 30-year synthetic temperature time series. This new time series is produced from complementary HR-XBT and satellite observations (Section 2.4.2). Along the transect, warming trends in the Kuroshio (Section 2.5.1) have led to an increase in surface and subsurface MHW days per year (Section 2.5.2). The largest mean MHW intensities and durations along the transect occur at depth (Section 2.5.3). Subsurface MHWs are more common during El Niño where an intensified Kuroshio Extension intersects the transect (Section 2.5.4). In contrast, surface MHW occurrence along the transect is not influenced by ENSO (Section 2.5.4). We conclude in Section 2.6 with a summary and implications of this

work.

## 2.4 Data and Methodology

### 2.4.1 Data

Subsurface temperature observations were obtained from HR-XBT measurements along transect PX40, which runs between Yokohama, Japan and Honolulu, Hawai'i. This transect crosses the Kuroshio at approximately 34.5°N, just south of where the Kuroshio separates from the coast to form the Kuroshio Extension (Figure 2.1). To focus on the WBC system, only observations west of 150°E were used. HR-XBT temperatures were objectively mapped onto a 10-m depth grid between the surface and 800-m and a 0.1° along-transect longitudinal grid (Roemmich 1983). At the time of this study, PX40 had been occupied 41 times since 2012.

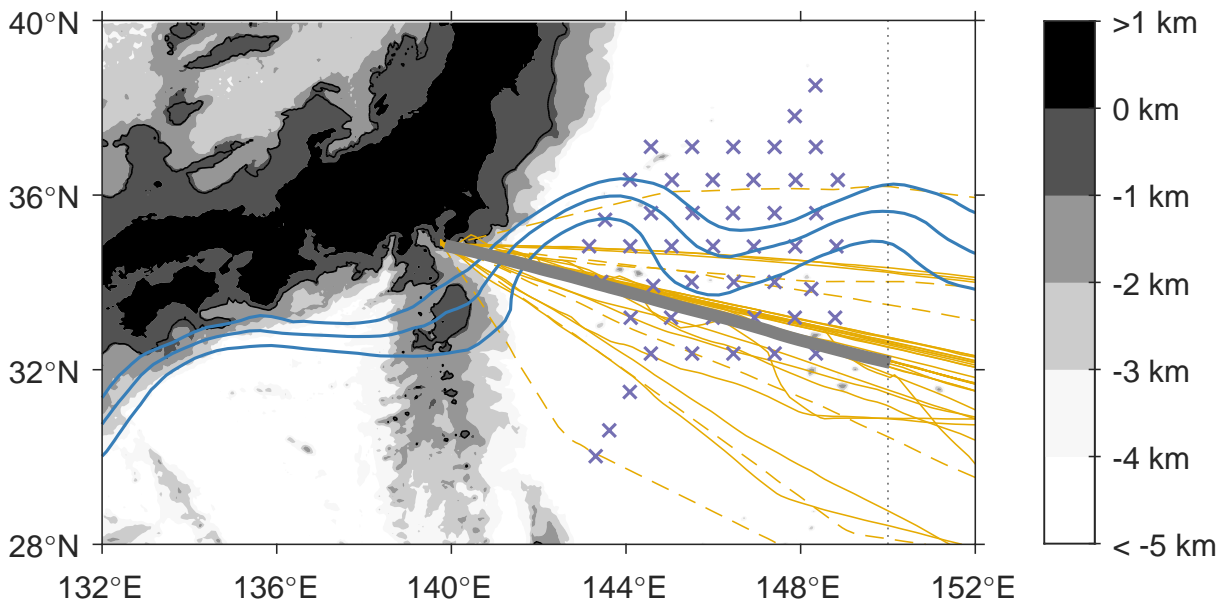


**Figure 2.1.** PX40 nominal transect (thick grey line) overlain on the bathymetry of the northwest Pacific Ocean. Black contour line is the 800-m isobath. Gold lines show the paths of all individual PX40 transects (dashed transects were not used in this study due to being either too far from the nominal transect or more recent than available satellite altimetry observations). Purple crosses locate the PIES/CPIES deployed during the Kuroshio Extension System Study (2004 to 2006). Blue lines are the 0.9-m, 1.1-m, and 1.3-m absolute dynamic topography contours averaged over 1993 to 2022 and indicate the mean path of the Kuroshio and Kuroshio Extension. The thin dotted line is at 150°E.

The 2015 to 2022 temperature climatology from the  $1/4^{\circ}$  World Ocean Atlas 2023 (Locarnini et al. 2024) was used to adjust PX40 observations onto the mean transect. This climatology covers a similar time period as the PX40 observations. World Ocean Atlas 2023 has up to 102 standard depth levels of varying resolution and was therefore linearly interpolated onto the same 10-m depth grid as the HR-XBT temperature data.

Daily SLA was from the  $1/4^{\circ}$  Global Ocean Gridded L4 Sea Surface Heights and Derived Variables Reprocessed product (CMEMS 2024a). Daily SST was from the  $1/4^{\circ}$  NOAA Daily Optimum Interpolation Sea Surface Temperature version 2.1 product (Huang et al. 2021). This SST product is independent of HR-XBT observations (Huang et al. 2021; Willis et al. 2003). Both the SLA and SST time series spanned the period 1 Jan 1993 to 30 April 2023.

The maximum climatological surface mixed layer depth along PX40 was obtained from the  $1^{\circ}$  Mixed Layer Depth Climatology Computed with a Density Threshold Criterion of 0.03  $\text{kg m}^{-3}$  from 10-m Depth Value product (de Boyer Montégut et al. 2004).

The Oceanic Niño Index (ONI) was used to identify El Niño ( $\text{ONI} > +0.5^{\circ}\text{C}$ ) and La Niña ( $\text{ONI} < -0.5^{\circ}\text{C}$ ) periods between 1993 and 2022. ONI is computed based on the 3-month running mean of SST anomalies in the Niño 3.4 region and, here, was taken to represent the central month of each 3-month average. These same processing steps were applied to the Niño 3 index used to identify Eastern Pacific El Niño conditions and the Niño 4 index used to identify Central Pacific El Niño conditions (e.g. Capotondi et al. 2015; Wang et al. 2024).

Monthly zonal and meridional velocities from the  $1/12^{\circ}$  Global Ocean Physics Reanalysis 12V1 product (GLORYS; Lellouche et al. 2021) were used to provide spatial context for the state of the Kuroshio Extension system between 1993 and 2020. GLORYS was validated against monthly PX40 cross-transect velocities from Chandler et al. (2022a) between 2004 and 2019 (Text 2.B; Figure 2.2). The two velocity products agreed well, although the core of the Kuroshio was shifted slightly offshore at depth in GLORYS.

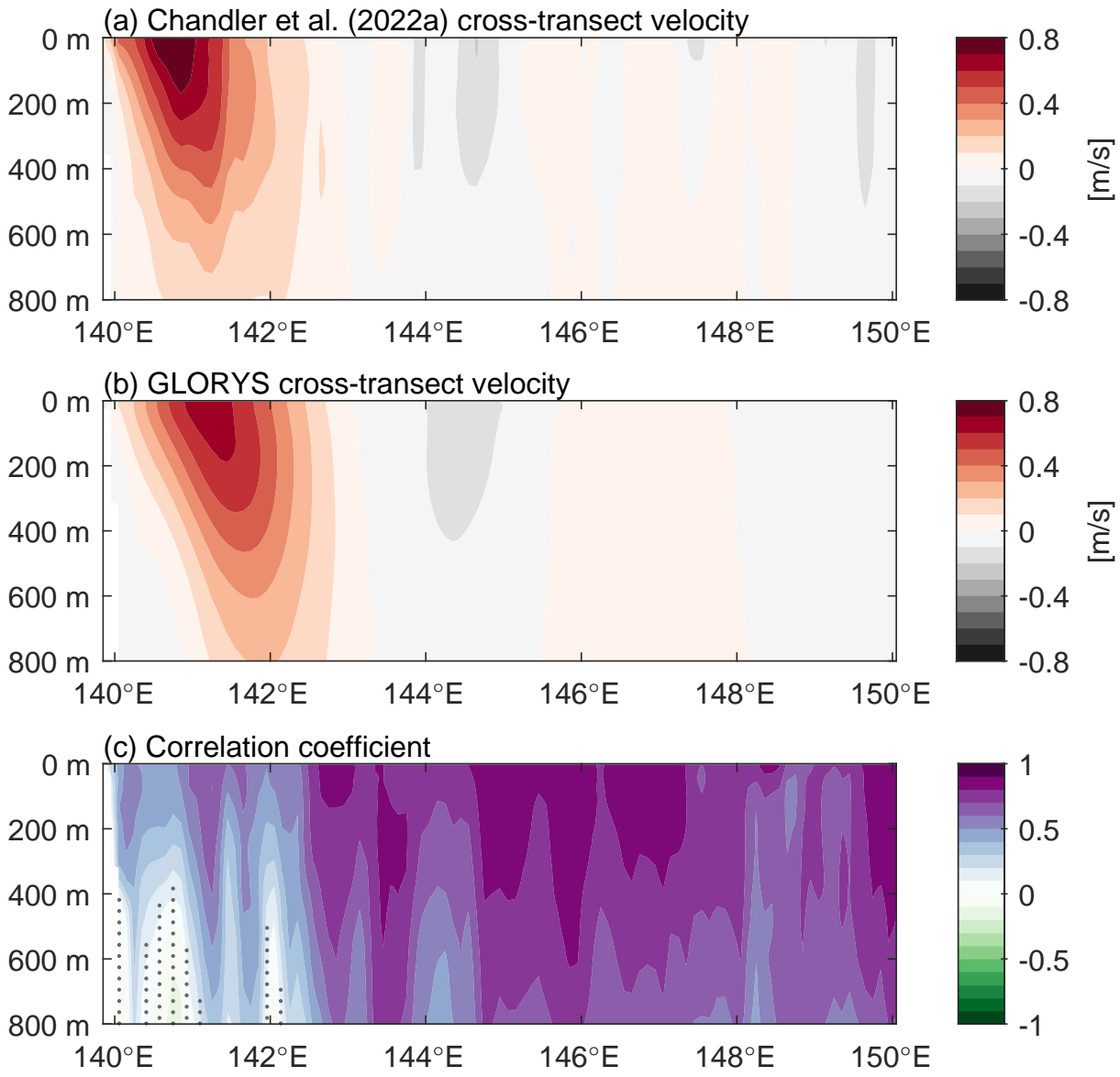


**Figure 2.2.** Time-mean of the 2004 to 2019 monthly cross-transect velocity time series from (a) Chandler et al. (2022a) and (b) GLORYS. A positive velocity is northward. (c) Correlation coefficients between the Chandler et al. (2022a) and GLORYS velocity anomalies. Stippling identifies where correlations are not significant at the 95% significance level (effective degrees of freedom computed following Von Storch and Zwiers (1999)).

## 2.4.2 Synthetic Temperature Time Series Development

All 41 individual occupations of PX40 were averaged to obtain a first guess of the mean location of the PX40 transect. Individual transects that reached a maximum latitudinal distance of more than  $4^{\circ}$  from the mean transect were removed and the mean was recalculated until all remaining transects were within  $4^{\circ}$  of latitude. Three occupations were removed through this procedure. A further three occupations after April 2023 were also removed as, at the time of analysis, SLA data was not yet available. This study therefore utilised 35 occupations of PX40 between November 2012 to March 2023. Every month of the year had at least one occupation. Each ENSO phase (El Niño, La Niña, neutral) had at least eight occupations.

Individual transects do not exactly follow the mean PX40 transect (Figure 2.1). Therefore, for each occupation, the difference in climatological temperature between the occupied transect and the mean transect was used to correct for variability in ship tracks (Chandler et al. 2022a; Zilberman et al. 2018).

Daily SLA and SST were interpolated onto the mean transect and averaged over the 10 days following the start date of each PX40 occupation. A 10-day temporal resolution is consistent with the cycle duration of the satellite altimetry reference missions. The 35-transect seasonal cycle, computed via least-squares fitting an annual harmonic, semi-annual harmonic, and mean, was removed to obtain temporal anomalies ( $T'(z)$ ,  $SLA'$ ,  $SST'$ ) that were all referenced to the same time period (November 2012 to March 2023). Comparison of these PX40-period SLA and SST seasonal cycles against those computed using the full (January 1993 to April 2023) time-series confirmed that the temporal coverage of the 35 PX40 occupations was able to resolve the seasonal cycle.

A strong relationship exists between  $SLA'$  and  $T'(z)$  below the surface mixed layer along PX40, while  $SST'$  is better correlated with surface and near-surface temperature anomalies (not shown, see also Willis et al. 2003). Therefore, to take advantage of their individual strengths, the 10-day averaged  $SLA'$  and  $SST'$  were fit to observed  $T'(z)$  at the times of the 35 PX40

occupations using a multiple linear regression (e.g. Ridgway et al. 2008; Willis et al. 2003):

$$T'(x, z, t) \approx \alpha(x, z) \cdot SLA'(x, t) + \beta(x, z) \cdot SST'(x, t) \quad (2.1)$$

where  $x$  is location along the transect,  $z$  is depth,  $t$  is time, and  $\alpha$  and  $\beta$  are regression coefficients.

The full (January 1993 to April 2023) SLA and SST time series were then averaged every 10 days and the PX40-period seasonal cycles removed. The regression coefficients ( $\alpha$  and  $\beta$ ) were applied (Equation 2.1) to these 10-day averaged  $SLA'$  and  $SST'$  time series to obtain estimates of 10-day averaged synthetic  $T'(z)$  from 0-m down to 800-m deep over the full January 1993 to April 2023 time period.

### 2.4.3 Synthetic Temperature Time Series Validation

A leave-one-out approach, where regression coefficients ( $\alpha$  and  $\beta$ ; Equation 2.1) were recalculated using all PX40 occupations except one and a synthetic estimate was computed for the withheld occupation, was used to validate the method (e.g. Gilson et al. 1998). This procedure was repeated 35 times, such that all PX40 occupations were withheld once. The resulting 35 synthetic estimates compared favourably with the 35 HR-XBT observations, albeit with reduced variability and with small discrepancies in the surface mixed layer (Figure 2.3). Standard deviations demonstrated a similar structure (Figures 2.3a and 2.3b) but with smaller values for the synthetic estimates compared to observations. Correlations between synthetic and observed  $T'(z)$  were significant ( $p < 0.05$ ) almost everywhere, except for some near-surface regions and at the very western edge (Figure 2.3c). Likewise, the root-mean-square signal of observed  $T'(z)$  was greater than the root-mean-square-error (RMSE) between synthetic and observed  $T'(z)$  except for a few regions near the surface and at the western edge (Figure 2.3d). Averaged over the entire section, RMSE between synthetic and observed  $T'(z)$  was  $1.12^\circ\text{C}$ .

To validate the ability of the method to be extended back in time through use of the satellite record prior to PX40 observations (i.e. January 1993 to October 2012), synthetic  $T'(z)$

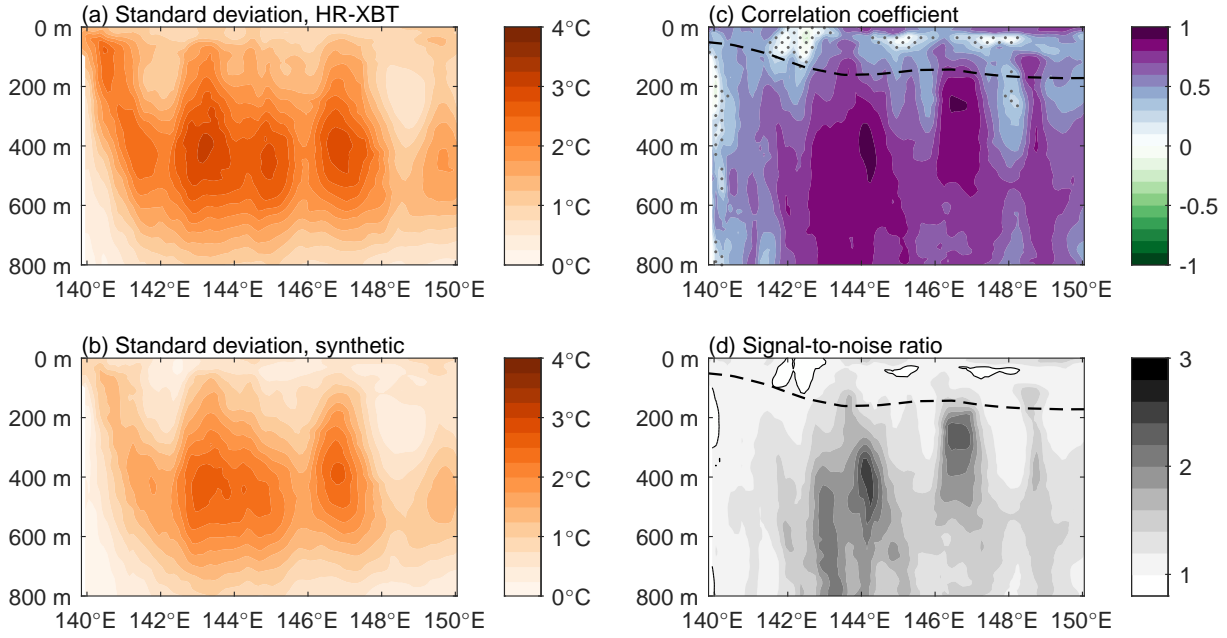


**Figure 2.3.** Standard deviations of (a) HR-XBT observed temperature anomalies and (b) synthetic temperature anomalies at the times of PX40 occupations. (c) Correlation coefficients between HR-XBT observed and synthetic temperature anomalies. Stippling is where correlations are not significant at the 95% significance level (each occupation considered independent). (d) Ratio of the root-mean-square signal of HR-XBT observed temperature anomalies to the root-mean-square-error between HR-XBT observed and synthetic temperature anomalies. Black contour identifies a ratio of 1. Black dashed line in (c) and (d) is the maximum climatological mixed layer depth.

was compared against independent observations from the Kuroshio Extension System Study (KESS). During KESS, an array of 46 PIES/CPIES were deployed in the Kuroshio Extension east of Japan (Figure 2.1) for 16 months between 2004 and 2006 (Donohue et al. 2010). Here, the objectively mapped subsurface temperature fields from KESS (Donohue et al. 2010) were interpolated onto the same PX40 transect and 10-m depth grid as synthetic  $T'(z)$ , averaged into 10-day periods, and de-seasoned by subtracting the PX40-period seasonal cycle. KESS and synthetic  $T'(z)$  were compared over the longitude range that provided the longest time period (June 2004 to September 2005) of consistently good quality KESS data, and were found to compare favourably (Figure 2.4). The RMSE between KESS and synthetic  $T'(z)$  averaged over the entire section was 1.16°C, similar to the 1.12°C between HR-XBT and synthetic  $T'(z)$ . This validation therefore provided confidence that satellite observations could indeed be used to

extend the synthetic  $T'(z)$  time series back in time prior to PX40 observations. However, there is no guarantee that these same regression coefficients will continue to hold in the future given expected climate shifts and resulting non-stationarity (e.g. Litzow et al. 2020).

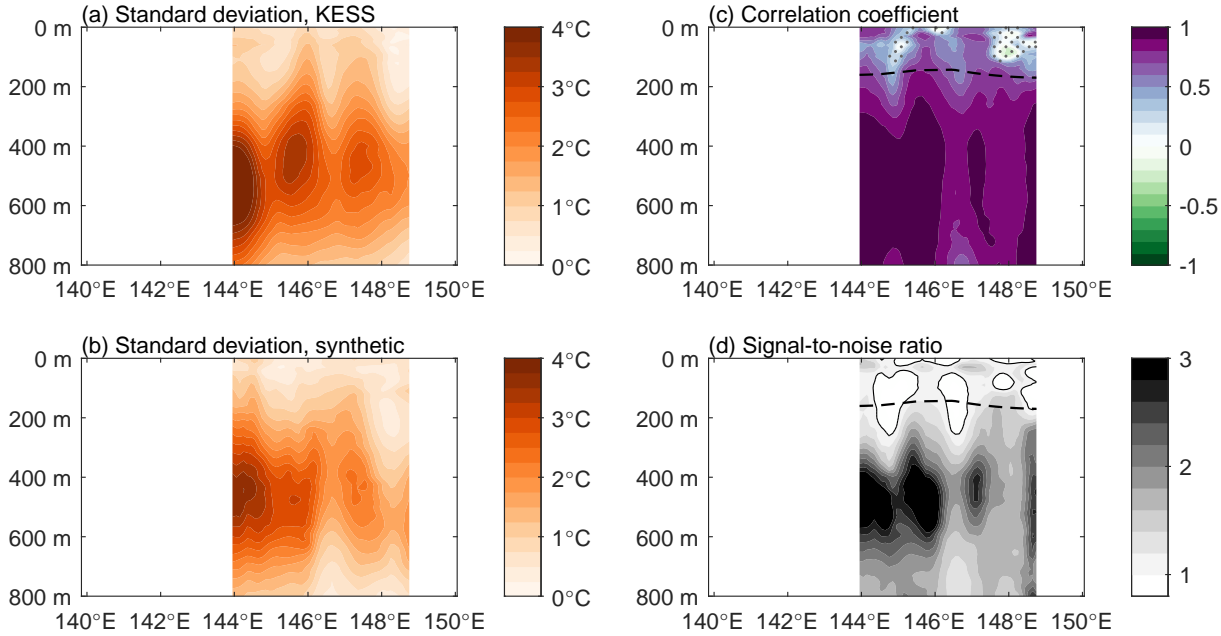


**Figure 2.4.** Standard deviations of (a) Kuroshio Extension System Study (KESS) temperature anomalies and (b) synthetic temperature anomalies between June 2004 and September 2005. (c) Correlation coefficients between KESS and synthetic temperature anomalies. Stippling is where correlations are not significant at the 95% significance level (effective degrees of freedom computed following Von Storch and Zwiers (1999)). (d) Ratio of the root-mean-square signal of KESS temperature anomalies to the root-mean-square-error between KESS and synthetic temperature anomalies. Black contour identifies a ratio of 1. Black dashed line in (c) and (d) is the maximum climatological mixed layer depth.

#### 2.4.4 Marine Heatwave Identification

The synthetic  $T'(z)$  time series (re-referenced to the 1993 to 2022 time-mean) was used to examine extreme ocean temperature events (i.e. MHWs) between the surface and 800-m deep over the 1993 to 2022 time period.

Qualitatively, a MHW is defined as a prolonged period of anomalously warm water at a particular location (Hobday et al. 2016). One commonly used quantitative definition is where daily ocean temperatures are warmer than the 90th percentile climatology for a period of five or

more days, with events separated by two or less days considered as a single event (Hobday et al. 2016). However, the qualitative definition offers flexibility, including in the temporal resolution of the time series (Farchadi et al. 2025; Hobday et al. 2016; Oliver et al. 2021). For example, numerous studies have used monthly resolution temperature time series where MHWs are thus defined as extreme events lasting at least one month (e.g. Gregory et al. 2024; Jacox et al. 2022, 2020; Scannell et al. 2016; von Kietzell et al. 2022; Zhou et al. 2024).

Here, MHWs were defined as when synthetic  $T'(z)$  was above the 90th percentile threshold. This temperature anomaly threshold varied with  $x$  and  $z$  but, because the seasonal cycle had already been removed from the temperature time series, was constant in time. Due to the 10-day resolution of the synthetic time series, MHW conditions occurred during 10% of the study time period. MHW conditions occurring in consecutive 10-day periods were considered a single MHW event.

Following Hobday et al. (2016), MHW intensity was defined as  $T'(z)$ , i.e. the temperature anomaly relative to the 1993 to 2022 time-mean. Only mean event intensity was considered here as the reduced variability in the synthetic temperature time series compared to observations (Figures 2.3 and 2.4) meant that maximum event intensity was likely underestimated. Higher temporal resolution observations (e.g. daily) have more variability, and typically larger maximum values, than those based on longer (e.g. 10-day or monthly) time means (e.g. Hobday et al. 2016).

To examine whether there had been a change in MHW occurrence over the 30-year time series, linear trends were fit at every grid point ( $x, z$ ) to the number of MHW days per year. Trend significance was assessed using a two-tailed t-test (Draper and Smith 1998) where each year was considered independent. Linear trends were also computed for the synthetic  $T'(z)$  time series with significance assessed using a two-tailed t-test where the effective degrees of freedom was calculated using the integral timescale (Emery and Thomson 2001). Temperature trends were found to impact MHW identification along PX40 (see Section 2.5.2) therefore MHWs were also identified using the detrended synthetic  $T'(z)$  time series so that the influence of factors other than long-term ocean warming could be examined.

To examine the influence of one such factor, ENSO, on MHW occurrence along the transect, the percentage of time that MHW conditions were experienced during El Niño and La Niña was examined. Because synthetic  $T'(z)$  demonstrated limited ability in reproducing near-surface temperature anomalies (Figures 2.3 and 2.4), the detrended synthetic  $T'(z)$  time series was used to examine MHW occurrence in the subsurface (i.e. below the maximum climatological surface mixed layer depth) only. Detrended and 10-day averaged  $SST'$  were instead used to examine MHW occurrence at the surface, while MHW occurrence within the surface mixed-layer during ENSO was not considered. A chi-squared test was used to determine if MHW occurrence was significantly different from the expected 10% occurrence rate during each ENSO phase.

## 2.5 Results and Discussion

### 2.5.1 Temperature Trends

The 30-year length of the synthetic temperature time series allows multi-decadal subsurface temperature trends along transect PX40 to be estimated with a high degree of confidence (Figures 2.5a and 2.5c). Over 1993 to 2022, there was a significant warming trend at PX40 between 139.9°E to 142.9°E that extended throughout the upper 800-m, reaching  $0.09^{\circ}\text{Cyr}^{-1}$  within the subsurface (Figure 2.5a). The location of this significant warming coincides with the mean location of the Kuroshio jet (Figure 2.2). Kuroshio warming at the surface was typically reduced compared to the subsurface, although still significant, with a mean warming trend of  $0.02^{\circ}\text{Cyr}^{-1}$ . The observed surface and subsurface warming trends along PX40 became non-significant offshore of the Kuroshio then switched to a non-significant cooling trend east of approximately 146.8°E (Figure 2.5a).

The surface warming rate in the Kuroshio at PX40 (Figure 2.5a) is consistent with SST warming trends in the upstream Kuroshio over 1993 to 2013 (Wang et al. 2016), and with projected SST warming trends over the course of this century in the Kuroshio-Kuroshio Extension region from a high-resolution ocean model ( $1/11^{\circ}$  longitude  $\times$   $1/10^{\circ}$  latitude; Kawakami et al.

2024). However, there are very few other long time series of subsurface temperature in the Kuroshio. One of these time series is the 137°E repeat hydrographic transect that intersects the Kuroshio south of Japan, upstream of PX40, which has been occupied annually since 1967 then semi-annually since 1972 (Oka et al. 2018, 2017). Using wintertime observations over the period 1967 to 2016, Oka et al. (2017) found a warming trend in the Kuroshio at 137°E that, much like our result at PX40 (Figure 2.5a), was largest in the subsurface between roughly 200-dbar to 600-dbar. However, Kuroshio warming trends at 137°E between 1967 and 2016 were roughly half those observed at PX40 between 1993 and 2022. The larger subsurface temperature trends in our more contemporary data set therefore suggest an acceleration of subsurface warming within the Kuroshio.

Oka et al. (2017) attributed Kuroshio subsurface warming at 137°E to a decrease in Kuroshio large-meander occurrence. However, large-meander events (Yoshida et al. 2006) have minimal impact on the path of the Kuroshio at PX40 (e.g. Kawabe 1985, 1995). Additionally, the Kuroshio has been in an ongoing large-meander state since August 2017 (Qiu et al. 2023; Yoshida et al. 2006), coinciding with some of the warmest subsurface temperature anomalies at PX40 (Figure 2.5c). Decreasing large-meander occurrence therefore cannot explain the significant subsurface warming trend between 1993 and 2022 at PX40. Strengthening of advective heat transport within the Kuroshio also seems an unlikely driver of subsurface warming given that Kuroshio mass transport has decreased over 2004 to 2019 at PX40 (Chandler et al. 2022a) and over 1998 to 2013 further upstream at the Tokara Strait (Liu et al. 2021). This decrease in mass transport has been driven by vertical pycnocline displacement (i.e. heave) caused by wind stress curl changes over the North Pacific Ocean (Liu et al. 2021). Heaving of isotherms, which produces large temperature changes where vertical temperature gradients are steep, could be driving subsurface warming in the Kuroshio. For the 1993 to 2022 time-mean temperature along PX40, the sloping shape of the steep vertical temperature gradient in the Kuroshio (Figure 2.5b) coincided with, and was replicated by, the sloping shape of the strong warming trend in the Kuroshio (Figure 2.5a). However, because the largest Kuroshio temperature trends at

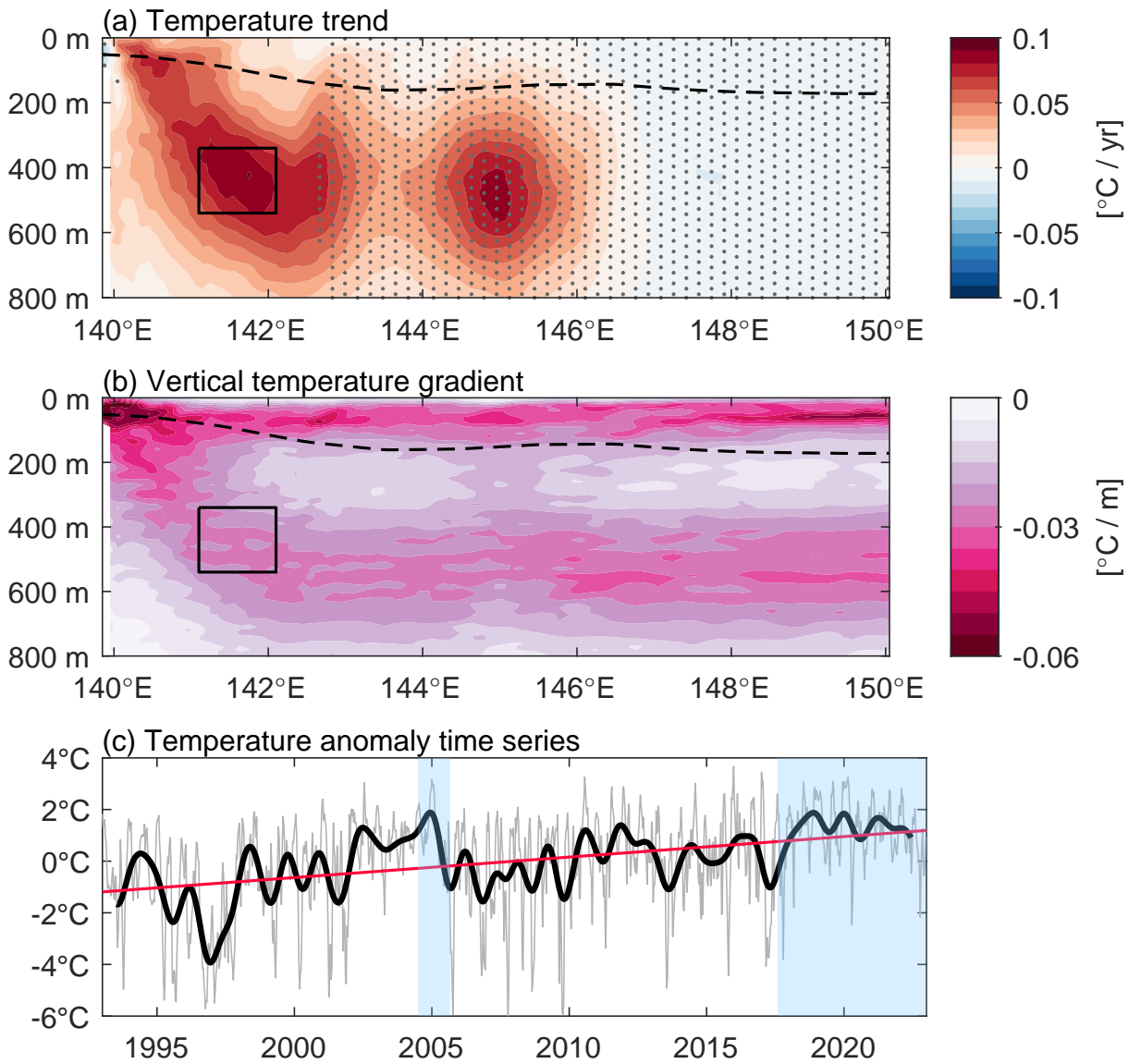


**Figure 2.5.** (a) Temperature trends over 1993 to 2022. Stippling is where trends are not significant at the 95% significance level. (b) Vertical temperature gradients in the 1993 to 2022 time-mean temperature. The black dashed line in (a) and (b) is the maximum climatological mixed layer depth and the black box indicates the region plotted in (c). (c) Temperature anomaly time series over 1993 to 2022 area-averaged in the region where Kuroshio warming trends were largest. Thin grey line is the raw (10-day) time series, thick black line is the annually low-pass filtered time series, red line is the trend. Light blue shading identifies Kuroshio large-meander periods.

PX40 (around 141.8°E and 420-m deep) do not coincide with the steepest vertical temperature gradients (Figures 2.5a and 2.5b), we hypothesise that additional factors likely also contribute to the observed subsurface warming trends in the Kuroshio at PX40.

### 2.5.2 Trends in Marine Heatwave Occurrence

Over the 30-year time series, a positive trend in the number of MHW days per year was observed throughout the water column from close to the coast out to around 146.5°E (Figure 2.6a). This trend was significant within the Kuroshio, between 139.9°E to 142.9°E, increasing by as much as 4.2 days per year. If these significant trends are maintained through to the end of the century (i.e. 2100) then, relative to a fixed baseline, the number of subsurface Kuroshio MHW days per year at PX40 would increase by between 120 to 330 days. Similar increases in surface MHW days per year are projected for this same region and time period based on a high-resolution ocean model (Kawakami et al. 2024). Further offshore, east of 146.5°E, the observed trend in MHW days per year at PX40 became weakly negative and was not significant (Figure 2.6a).

Long-term changes in MHWs can be caused by changes in the temperature mean and/or temperature variability. Here, as in many other MHW studies (e.g. Du et al. 2022; Kawakami et al. 2024; Oliver 2019; Oliver et al. 2019, 2018), trends (or lack thereof) in the number of MHW days per year were largely due to trends in ocean temperature causing a change in the mean temperature. In particular, the significant Kuroshio warming trend occurred in the same location (139.9°E to 142.9°E) as the significant increase in the number of MHW days per year (Figures 2.5a and 2.6a). In contrast, there were no significant increasing trends in MHW days per year when the temperature trend was removed before identifying MHWs (Figure 2.6b). In fact, a significant decrease in the number of MHW days per year (reaching as large as -2 days per year) was instead found between 140.8°E to 142.3°E. This decrease in MHW days at the offshore edge of the Kuroshio was likely due to the decreased variability here during the second half of the time series compared to the first half (Figure A2.1). Decreases in variance were also

evident in both daily SLA (comparing 1993 to 2007 with 2008 to 2022) and monthly GLORYS depth-integrated velocity eddy kinetic energy (comparing 1993 to 2007 with 2008 to 2020). Trends in MHW days per year were not significant elsewhere along the transect when using the detrended temperature anomaly time series (Figure 2.6b).

Due to the influence of the Kuroshio warming trend on MHW identification and occurrence, we detrended the synthetic temperature time series before identifying MHWs for the analyses in the following sections. Detrending allowed us to examine the influence of other physical processes independent of this long-term background warming.

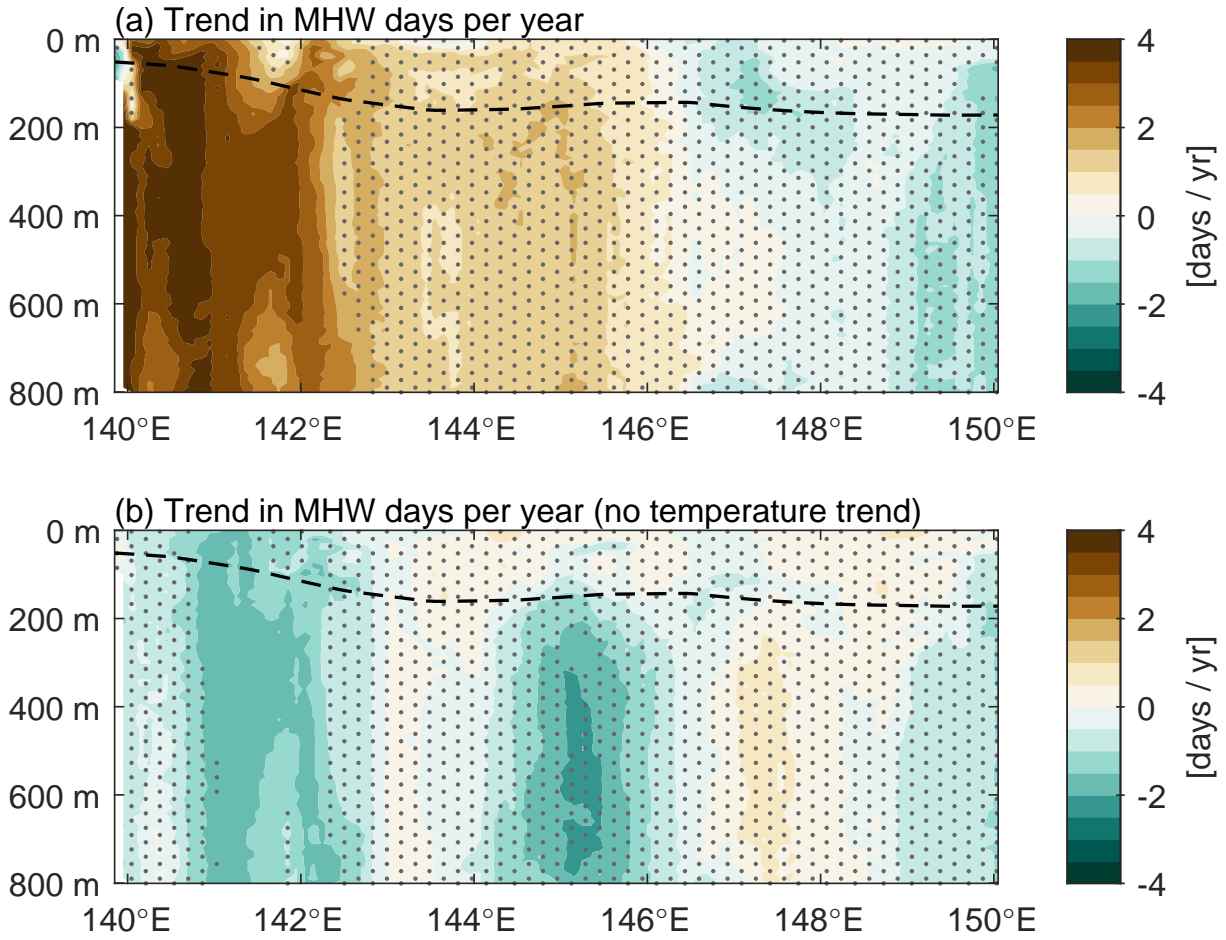


**Figure 2.6.** Trends over 1993 to 2022 in (a) marine heatwave (MHW) days per year, and (b) MHW days per year when the 1993 to 2022 temperature trend is removed. Stippling is where trends are not significant at the 95% significance level. Black dashed line is the maximum climatological mixed layer depth.

### 2.5.3 Marine Heatwave Primary Metrics

Reporting of standardised MHW metrics helps facilitate comparisons between different events, locations, and times (Hobday et al. 2016). Here, we present the primary MHW metrics of intensity and duration averaged over all events between 1993 and 2022. As noted above, the synthetic temperature anomaly time series was detrended before these primary metrics were computed.

At every longitude along the transect, the largest mean event intensities were found below the sea surface (Figure 2.7a). Similar subsurface intensification has been observed by studies examining subsurface MHWs in the tropical western Pacific Ocean (Hu et al. 2021) and coastal southeastern Australia (Schaeffer and Roughan 2017). Additionally, along PX40, the largest mean event intensities ( $4.1^{\circ}\text{C}$ ) occurred around 500-m deep at approximately  $145^{\circ}\text{E}$  (Figure 2.7a). This longitude coincides with where the Kuroshio Extension meanders most closely to PX40 (Figures 2.1 and 2.2). Variability in the position of the Kuroshio Extension, which is known to be sizeable here (Donohue et al. 2010; Qiu et al. 2014), likely drives these large mean event intensities along PX40 at  $145^{\circ}\text{E}$ .

Mean event durations (Figure 2.7b) followed a different pattern than mean event intensities (Figure 2.7a). The shortest mean durations (13.3 days) were found at the western boundary, consistent with the shorter durations that are typical of surface MHWs in WBC regions (Holbrook et al. 2019; Sen Gupta et al. 2020). Mean MHW durations then increased moving east along the transect, with the longest mean durations (35.5 days) occurring around approximately  $144^{\circ}\text{E}$  at depths below 400-m (Figure 2.7b). MHWs at this depth are most likely advection-driven by Kuroshio Extension variability (e.g. Xu et al. 2024), and we hypothesise that strengthening of the Kuroshio Extension could be a key driver of the longer MHW durations here. Indeed, when averaging monthly GLORYS depth-integrated velocities for the longest (>30-day) duration events over 1993 to 2020 at  $144.05^{\circ}\text{E}$  and 440-m deep (i.e. the grid-point along the transect where mean event duration was longest), the Kuroshio, Kuroshio Extension, and first

quasi-stationary meander recirculation were all significantly stronger compared to the mean state (Figure A2.2). Further east along the transect, mean event durations tended to decrease again (Figure 2.7b).

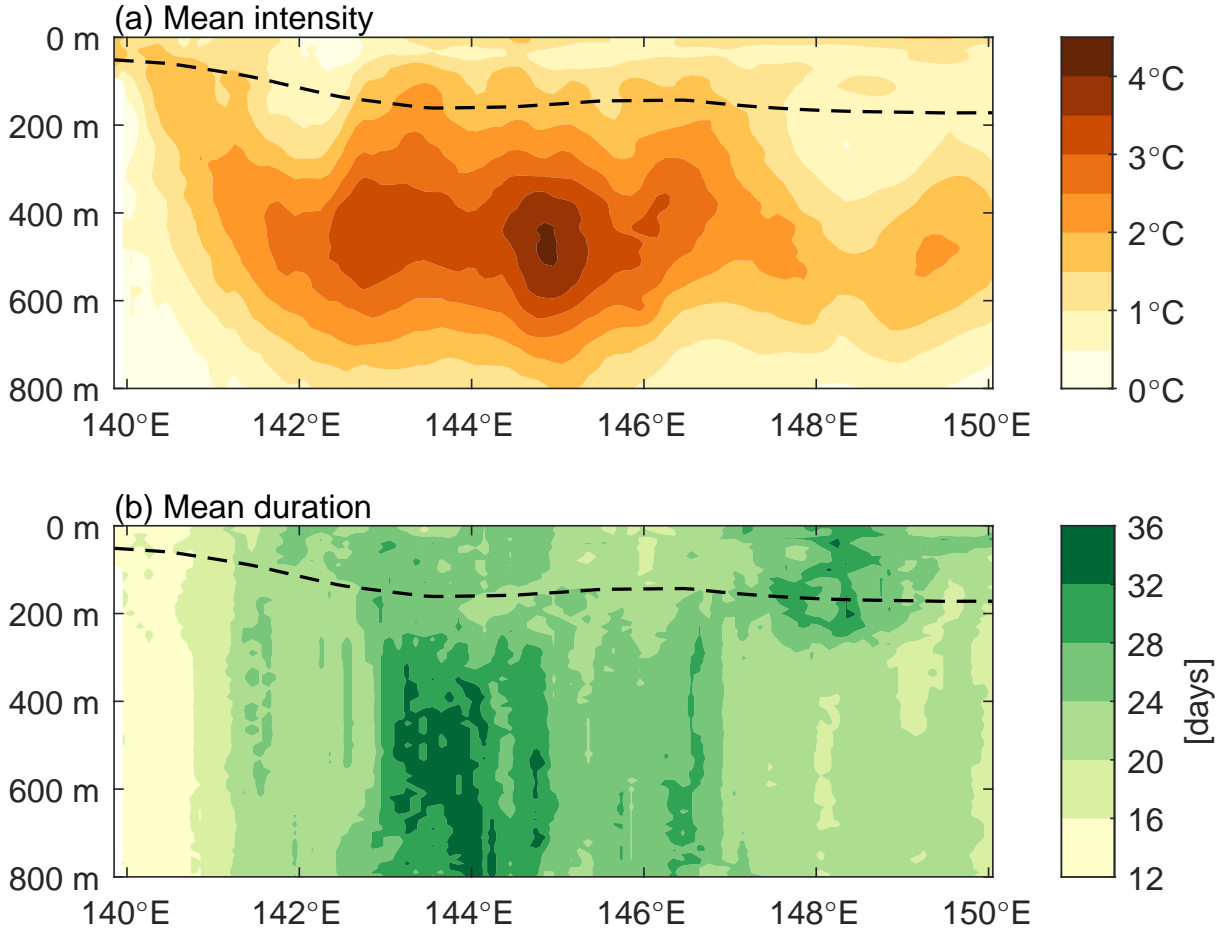


**Figure 2.7.** Mean **(a)** intensity and **(b)** duration averaged over all marine heatwave events between 1993 and 2022. Black dashed line is the maximum climatological mixed layer depth.

Relatively longer mean durations were also evident near the surface (shallower than 250-m) around 148°E. We are unsure of what unique physical processes may be driving the increased MHW duration in this region compared to elsewhere in the near-surface. However, this region coincides with where the synthetic time series most poorly reproduced observed temperature variability (Figures 2.3c and 2.4c). The increased mean duration (and slightly decreased mean intensity) at this location may therefore reflect limitations in the method's ability to reproduce temperature variability in the surface mixed-layer to a high degree of accuracy (e.g.

Willis et al. 2003).

#### 2.5.4 Influence of ENSO on Marine Heatwave Occurrence

Based on the 90th percentile temperature anomaly threshold used, MHW conditions would occur around 10% of the time during El Niño and La Niña (and neutral) periods if ENSO did not impact MHW occurrence along the transect. Surface MHW occurrence along PX40 was not significantly different from this expected 10% occurrence rate (Figures 2.8a and 2.8c), consistent with the weak correlation between the Niño 3.4 index and SST in this region (e.g. Talley et al. 2011). Holbrook et al. (2019), Sen Gupta et al. (2020), and Gregory et al. (2024) also show essentially no relationship between ENSO and surface MHW occurrence in the PX40 region east of Japan. However, in contrast to the surface, subsurface MHW occurrence along PX40 shows a strong relationship with ENSO (Figure 2.8). Relying only on SST observations would therefore lead to incomplete conclusions being drawn about the influence of ENSO on MHW occurrence along PX40.

During El Niño, subsurface MHWs along PX40 occurred significantly more often in a western region between approximately 141.4°E to 144.6°E and an eastern region between approximately 147.5°E to 148.6°E (Figures 2.8a and 2.8b). At both locations, the increased MHW occurrence was evident from the base of the surface mixed layer down to 800-m deep. In contrast, subsurface MHWs during La Niña occurred significantly less often between approximately 144°E to 146.6°E and from approximately 147.6°E out to the eastern end of the transect (Figures 2.8c and 2.8d). This decreased MHW occurrence was also typically evident from the base of the surface mixed layer down to 800-m deep, although there were some regions where it did not extend all the way up to the base of the surface mixed layer.

Recently, Wang et al. (2024) demonstrated that surface and near-surface velocities in the Kuroshio and Kuroshio Extension strengthen during El Niño due to a strengthening of the mid-latitude westerlies driving a more negative wind stress curl over the subtropical North Pacific Ocean. Given that the strength of the Kuroshio Extension and its Southern Recirculation Gyre

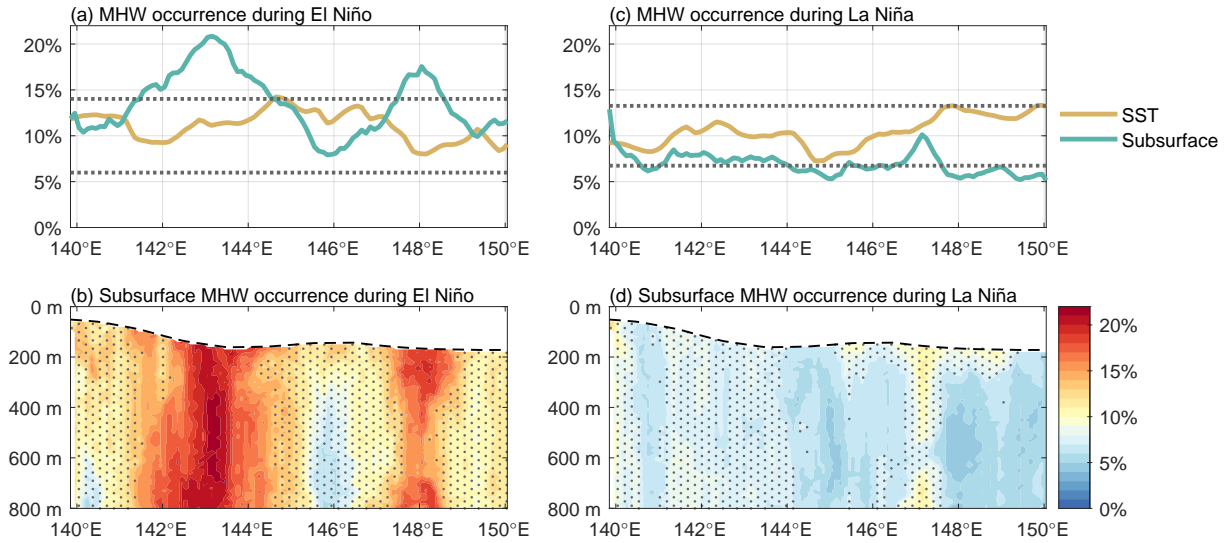


**Figure 2.8.** Percentage of time that marine heatwaves (MHWs) occurred along PX40 during (a,b) El Niño and (c,d) La Niña over the 1993 to 2022 time period. (a) and (c) show MHW occurrence depth-averaged below the maximum climatological mixed layer depth (subsurface, green) and at the surface from sea surface temperature (SST, brown). Dotted lines bound where occurrence is not significantly different from 10% of the time at the 95% significance level. (b) and (d) show MHW occurrence below the maximum climatological mixed layer depth (black dashed line). Stippling is where occurrence is not significantly different from 10% of the time at the 95% significance level.

tend to vary roughly in phase (Qiu et al. 2014), we may expect both to strengthen during El Niño periods. Indeed, using the GLORYS eddy-resolving ocean reanalysis, both the Kuroshio Extension and its Southern Recirculation Gyre were found to strengthen during El Niño (Figure 2.9b), thereby transporting more warm subtropical-origin water. Mean subsurface temperatures along PX40 were therefore warmer during El Niño, compared to the 1993 to 2022 time-mean, where the strengthened Southern Recirculation Gyre intersected the transect (Figure 2.10a). These warmer mean temperatures led to the increased subsurface MHW occurrence observed in both regions along the transect (141.4°E to 144.6°E and 147.5°E to 148.6°E) during El Niño (Figures 2.8b and 2.10a).

The stronger Kuroshio Extension and Southern Recirculation Gyre during El Niño was also associated with a more coherent (less variable) Kuroshio Extension jet (Figure 2.9), consistent with the inverse relationship between Kuroshio Extension strength and path length

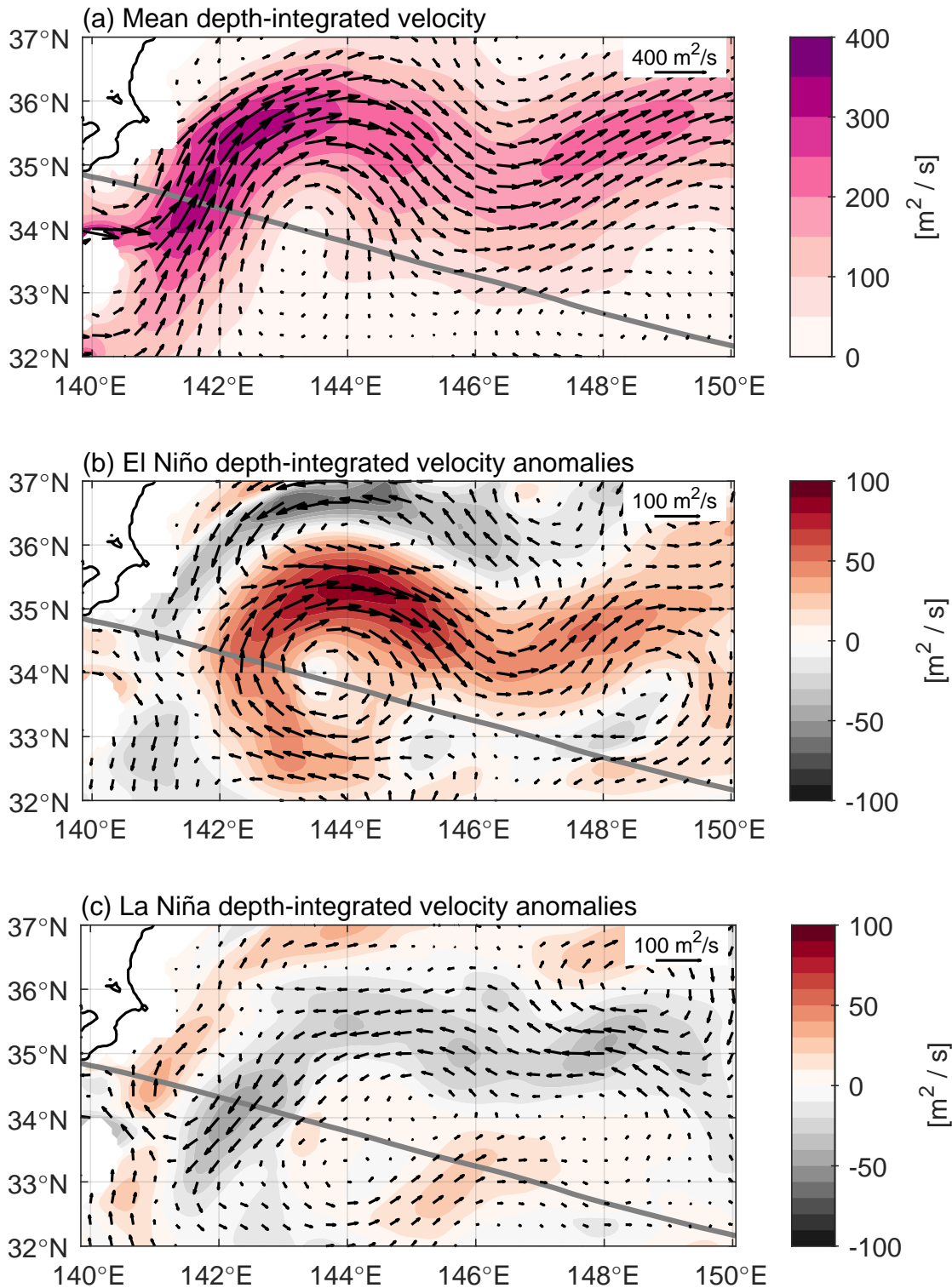


**Figure 2.9.** GLORYS depth-integrated (0-m to 800-m) velocity (a) 1993 to 2020 time-mean, and anomalies averaged during (b) El Niño and (c) La Niña. Scale arrows are in the top right of each panel, but note the different scale for (a) compared to (b) and (c). Thick grey line is PX40. Black contour is the Japan coastline (0-m isobath).

shown by Qiu et al. (2014). Reduced variability in the path of the Kuroshio Extension resulted in reduced temperature variability along PX40 between 142.1°E to 148.1°E during El Niño periods compared to the full 1993 to 2022 time period (Figure 2.10b). Decreased variance produces a narrower distribution of temperature anomalies and therefore less extreme values. Between approximately 144.6°E to 147.5°E, the reduction in temperature variability during El Niño (Figure 2.10b) was substantial enough to oppose the positive shift in the temperature anomaly distribution from the increase in mean temperature during El Niño (Figure 2.10a). The net result was no significant change in subsurface MHW occurrence at this location along the transect (Figures 2.8b, 2.10a, and 2.10b).

Changes in subsurface MHW occurrence along PX40 during La Niña did not mirror changes in occurrence during El Niño (Figure 2.8). During La Niña, the Kuroshio Extension and its Southern Recirculation Gyre were both weaker (Figure 2.9c), resulting in reduced transport of warm subtropical-origin water and, importantly, reduced recirculation of this warm water across PX40. Slightly cooler mean subsurface temperatures compared to the 1993 to 2022 time-mean were therefore found along much of PX40 (Figure 2.10c). The path of the Kuroshio Extension also appeared to be less tightly defined during La Niña, resulting in a more diffuse mean state of the Kuroshio Extension (Figure 2.9). As such, decreases in subsurface MHW occurrence along PX40 during La Niña tended to be found where there were compounding effects of both a decrease in mean temperature and a decrease in temperature variability compared to the full 1993 to 2022 time period (Figures 2.10c and 2.10d). This slight negative shift and slight narrowing of the temperature anomaly distribution combined to produce less extreme positive temperature anomalies.

When considering El Niño diversity (Capotondi et al. 2015), similar significant increases in subsurface MHW occurrence were found along PX40 irrespective of whether Central Pacific or Eastern Pacific El Niño conditions existed (Figure 2.11). However, the increased subsurface MHW occurrence was significant over more of the PX40 cross-section during Central Pacific El Niño conditions compared to Eastern Pacific El Niño conditions. These differences likely arise

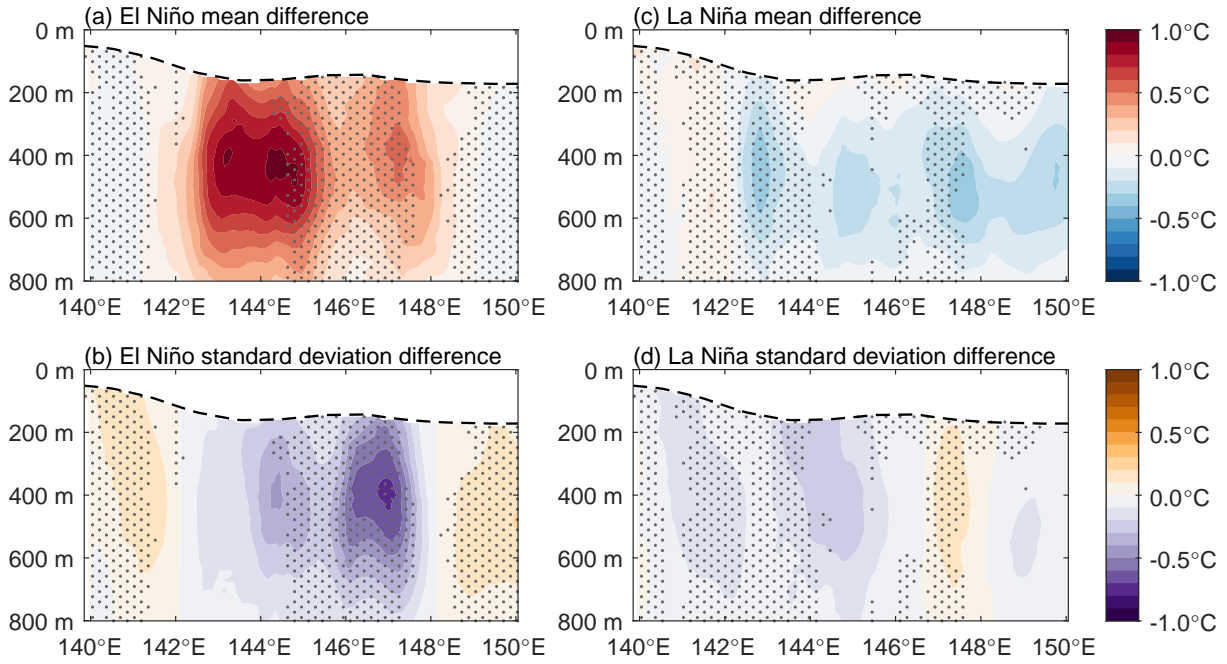


**Figure 2.10.** Difference in temperature anomaly **(a,c)** mean and **(b,d)** standard deviation between **(a,b)** El Niño compared to the full 1993 to 2022 time series (red indicates warmer temperatures and purple indicates smaller standard deviations during El Niño) and **(c,d)** La Niña compared to the full 1993 to 2022 time series (blue indicates cooler temperatures and purple indicates smaller standard deviations during La Niña). Stippling is where MHW occurrence below the maximum climatological mixed layer depth (black dashed line) is not significantly different from 10% of the time at the 95% significance level (see Figure 2.8).

because, although Central Pacific and Eastern Pacific El Niño conditions both drive strengthening of the Kuroshio and Kuroshio Extension, the strengthening is typically greater during a Central Pacific El Niño than an Eastern Pacific El Niño (Wang et al. 2024).

We have defined MHWs as when synthetic subsurface temperature anomalies were above the 90th percentile threshold for at least 10 days. However, results are rather insensitive to the choice of duration threshold (Figures A2.3 and A2.4). When using a 20-day duration threshold, subsurface MHWs occurred significantly more often than expected during El Niño in the same regions along PX40 as for the 10-day duration threshold (Figure A2.3a). Likewise, subsurface MHW occurrence was reduced during La Niña periods, although significant over a substantially smaller cross-sectional area of the transect when using a 20-day duration threshold compared with the 10-day duration threshold (Figure A2.3b). Surface MHWs along PX40 also did not

occur at a significantly different rate than expected during El Niño or La Niña when using a 20-day duration threshold, nor when the Hobday et al. (2016) definition was applied to daily SST observations (Figure A2.4). For these different duration thresholds, MHWs no longer occurred 10% of the time. Therefore, confidence intervals were assessed using a Monte Carlo approach (with  $1 \times 10^4$  iterations) where the start dates of observed MHW events were randomly assigned (observed durations and intensities were retained).

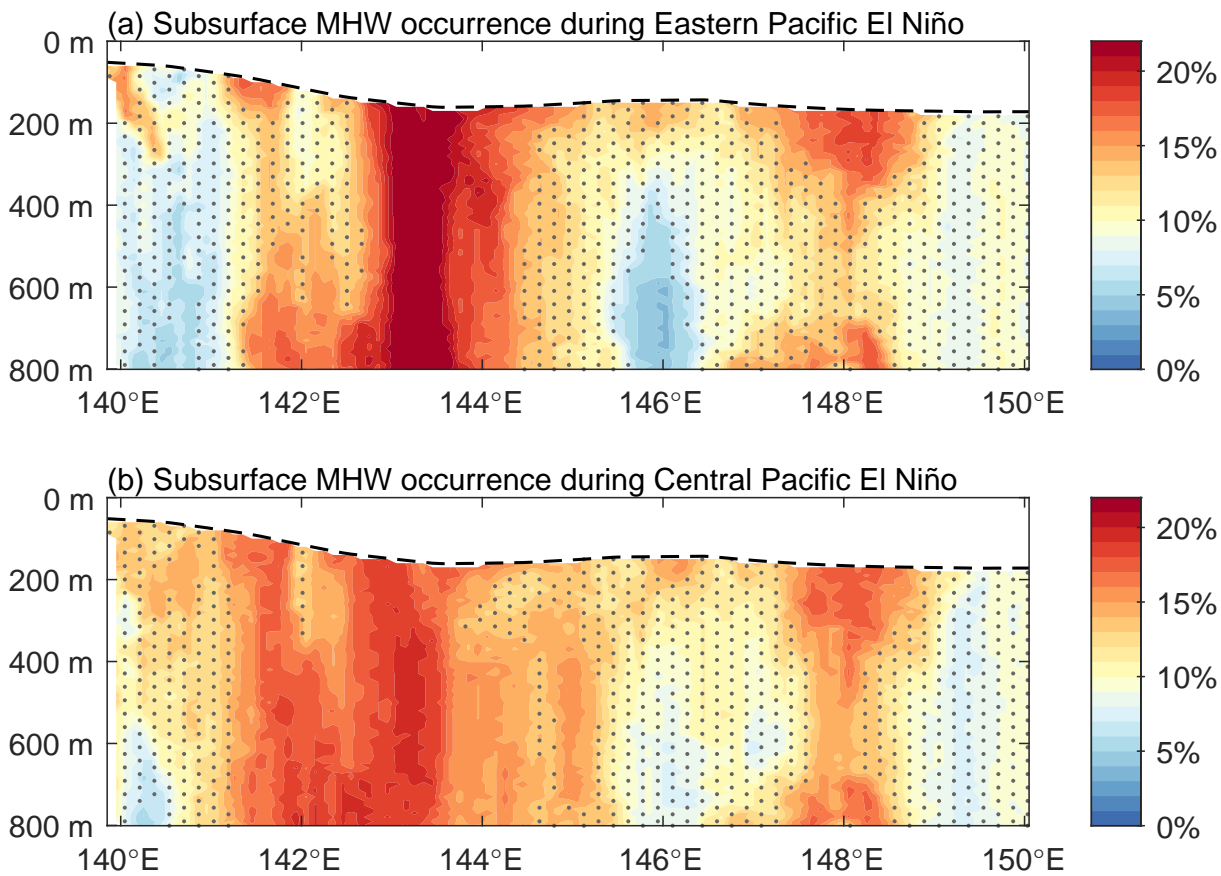


**Figure 2.11.** Percentage of time that subsurface marine heatwaves (MHWs) occurred along PX40 during (a) Eastern Pacific El Niño conditions (identified using the Niño 3 region) and (b) Central Pacific El Niño conditions (identified using the Niño 4 region) over 1993 to 2022. Black dashed line is the maximum climatological mixed layer depth. Stippling is where occurrence is not significantly different from 10% of the time at the 95% significance level.

## 2.6 Conclusions

Here, we have produced a novel 30-year time series of synthetic subsurface temperature anomalies at the western end of a HR-XBT transect that intersects the Kuroshio and Kuroshio Extension east of Japan. This time series has a 10-day temporal resolution, representing the 10-day average temperature. MHWs were defined as when the temperature anomaly was above the 90th percentile. All identified MHW events were therefore at least 10 days long. Nevertheless, our conclusions are rather insensitive to the duration threshold used to identify MHWs. The largest mean MHW event intensities were found to occur in the subsurface at every longitude along the transect, with the strongest mean intensity signal associated with variability in the path of a Kuroshio Extension meander around 145°E. At the western edge of the transect, in the Kuroshio, the number of MHW days per year significantly increased between 1993 and 2022. This increase in Kuroshio MHW days was caused by a significant warming trend in the Kuroshio, which appears to be predominantly driven by heaving of isotherms (e.g. Liu et al. 2021). When using the detrended temperature anomaly time series to identify MHWs, ENSO was found to influence the occurrence of subsurface MHWs along PX40. During El Niño, a more negative wind stress curl over the subtropical North Pacific Ocean (Wang et al. 2024) strengthens the Kuroshio Extension and its Southern Recirculation Gyre, thereby producing warmer mean subsurface temperatures where the current intersects the transect. As such, subsurface MHWs occurred significantly more often during El Niño periods where the strengthened Southern Recirculation Gyre of the Kuroshio Extension intersected the transect. This increase in subsurface MHW occurrence was broadly similar under both Central Pacific and Eastern Pacific El Niño conditions. In contrast, subsurface MHWs along PX40 occurred less often during La Niña periods.

Despite influencing subsurface MHW occurrence, ENSO did not significantly influence the occurrence of surface MHWs along the transect. MHW occurrence at the sea surface therefore differed from that below the surface mixed layer, reflecting the different forcing mechanisms (e.g. Elzahaby et al. 2021; Großelindemann et al. 2022; Xu et al. 2024). These differences at PX40

further emphasise that both surface and subsurface observations are needed to fully understand MHW events and their impacts. In practice, subsurface MHW identification is often not feasible as the sufficiently long time series required to identify MHWs are rare in the subsurface, and SST alone is not representative of temperatures below the surface mixed layer. Yet HR-XBT transects provide long-term observations of temperature between the surface and 800-m deep in all major ocean basins (Goni et al. 2019). The method we used here could thus be implemented to evaluate subsurface MHW properties along these other HR-XBT transects. However, WBCs typically extend much deeper than 800-m (Chandler et al. 2022a; Zilberman et al. 2023a). Because of the deep-reaching influence of the Kuroshio Extension (Chandler et al. 2022a; Jayne et al. 2009), we think it likely that the warmer subsurface temperatures and increased subsurface MHW occurrence observed along PX40 during El Niño will extend much deeper than 800-m and possibly as deep as 5000-m (e.g. Jayne et al. 2009).

The insignificant influence of ENSO on surface MHW occurrence along PX40 reflects the weak influence ENSO has on SST here (e.g. Talley et al. 2011). However, north of PX40, starting around 36°N, ENSO has a much stronger influence on SST. Cold SST anomalies occur during El Niño, driven by a deeper Aleutian Low and stronger midlatitude westerlies (Wang et al. 2024), with warm SST anomalies during La Niña. Nevertheless, the potential subsurface response in this northern region is unclear. ENSO predominantly drives a change in the strength of the Kuroshio Extension and its Southern Recirculation Gyre, rather than a meridional shift of the system (Figure 2.9). That being said, the Kuroshio Extension was typically a more defined jet during El Niño periods, with less transport occurring north of approximately 36°N (Figure 2.9b). Less warm subtropical-origin water would therefore be transported further north, which would be expected to decrease subsurface MHW occurrence. On the other hand, the Kuroshio and Kuroshio Extension are both generally weaker during La Niña (Figure 2.9c; Wang et al. 2024) which would also result in reduced transport of warm subtropical-origin water. The dominant influence on subsurface MHW occurrence in this northern region may instead stem from anticyclonic (warm-core) eddies spawned from the Kuroshio Extension (e.g. Elzahaby and

Schaeffer 2019; Großelindemann et al. 2022; Xu et al. 2024; Zhang et al. 2023). The potential impact of these eddies on subsurface MHWs north of PX40 is yet to be explored.

This work has clearly demonstrated that variability in the Kuroshio-Kuroshio Extension system exerts a strong control on subsurface temperature, and therefore subsurface MHW occurrence, along transect PX40. Due to the length of our novel 30-year synthetic temperature time series, we have largely focussed on the influence of ENSO. Yet other modes of climate variability, such as the Pacific Decadal Oscillation (PDO; Newman et al. 2016), also exhibit a relationship with the dynamics of the Kuroshio-Kuroshio Extension system. During a positive PDO, the westerly winds over the North Pacific Ocean tend to be stronger and located further south (Talley et al. 2011). As such, the phase of the PDO can influence, for example, the strength of the Kuroshio (e.g. Wang et al. 2016) and SST anomalies in the Kuroshio-Oyashio Extension region (e.g. Newman et al. 2016; Zhou et al. 2024). We therefore hypothesise that the PDO may also influence subsurface MHW occurrence along PX40. However, due to the canonically multidecadal periodicity of the PDO (as opposed to the interannual periodicity of ENSO), its impact on subsurface MHW occurrence along this transect has not been examined and remains unknown.

Lastly, present-day climate models struggle to predict the occurrence of monthly MHWs in the Kuroshio Extension (Zhou et al. 2024). This limited predictive skill is likely due to the coarser spatial resolution ( $\geq 1/4^\circ$ ) of these models (Hayashida et al. 2020; Zhou et al. 2024). There is therefore limited lead time to prepare for extreme ocean temperature events. Yet subsurface ocean temperatures can have a significant influence on fisheries in the Kuroshio-Kuroshio Extension region (e.g. Noto and Yasuda 1999; Yatsu 2019). Knowledge that subsurface MHWs along PX40 occur more commonly during El Niño periods should enhance MHW predictability in this region and thus aid in designing and implementing MHW adaptation plans (e.g. Pershing et al. 2018).

## 2.7 Open Research

HR-XBT data from transect PX40 was made available by the Scripps Institution of Oceanography HR-XBT program (<https://www-hrx.ucsd.edu/px40.html>). The World Ocean Atlas 2023 temperature climatology was obtained from NOAA NCEI at <https://doi.org/10.25921/va26-hv25> (Reagan et al. 2024). Sea surface height data (SLA and ADT) were obtained from the EU Copernicus Marine Service at <https://doi.org/10.48670/moi-00148> (CMEMS 2024a). Sea surface temperature data was obtained from NOAA NCEI at <https://doi.org/10.25921/RE9P-PT57> (Huang et al. 2024). Data from the Kuroshio Extension System Study was provided by Kathleen Donohue and can be accessed through the program website at <https://uskess.whoi.edu/overview/dataproducts/>. Bathymetry was from the 15 arcsecond GEBCO 2023 gridded bathymetry product (GEBCO Compilation Group 2023). The mixed layer depth climatology can be accessed at <https://doi.org/10.17882/91774> (de Boyer Montégut 2023). The Oceanic Niño Index (<https://www.cpc.ncep.noaa.gov/data/indices/oni.ascii.txt>) and Niño 3 and Niño 4 indices (<https://www.cpc.ncep.noaa.gov/data/indices/ersst5.Nio.mth.91-20.ascii>) were all obtained from NOAA CPC at <https://www.cpc.ncep.noaa.gov/data/indices/>. GLORYS12V1 velocity data was obtained from the EU Copernicus Marine Service at <https://doi.org/10.48670/moi-00021> (CMEMS 2024b). Cross-transect geostrophic velocity for transect PX40 can be accessed at <https://doi.org/10.5281/zenodo.5851311> (Chandler et al. 2022b). Dates of the Kuroshio large-meander events were obtained from JMA at [https://www.data.jma.go.jp/gmd/kaiyou/data/shindan/b\\_2/kuroshio\\_stream/kuroshio\\_stream.html](https://www.data.jma.go.jp/gmd/kaiyou/data/shindan/b_2/kuroshio_stream/kuroshio_stream.html). Colourmaps are from BrewerMap (<https://github.com/DrosteEffect/BrewerMap>). This work utilised some functions from the MATLAB Climate Data Toolbox (Greene et al. 2019). The objectively mapped HR-XBT observations and the synthetic temperature anomaly time series from this study are permanently and publicly available at <https://doi.org/10.5281/zenodo.14219180> (Chandler 2024b). The MATLAB script used to produce the synthetic temperature time series is also available through the above Zenodo link, as are implementations of this script in Julia and R (Chandler 2024b).

## **2.8 Acknowledgments**

We would like to thank the crews of the ships that collected these HR-XBT measurements (JRS Canis, Tacoma Trader, Cape Franklin, Undarum, and Tallahassee), and Kathleen Donohue for providing the Kuroshio Extension System Study data. The HR-XBT program data collection was supported by the NOAA Global Ocean Monitoring and Observing Program through Award NA20OAR4320278. MC, JS, and NZ were also supported by the NOAA Global Ocean Monitoring and Observing Program through Award NA20OAR4320278.

This chapter, in part, is currently being prepared for submission for publication of the material by Chandler, M., Sprintall, J., and Zilberman, N. V. The dissertation author was the primary investigator and author of this paper.

## 2.A Supplementary Figures for Chapter 2

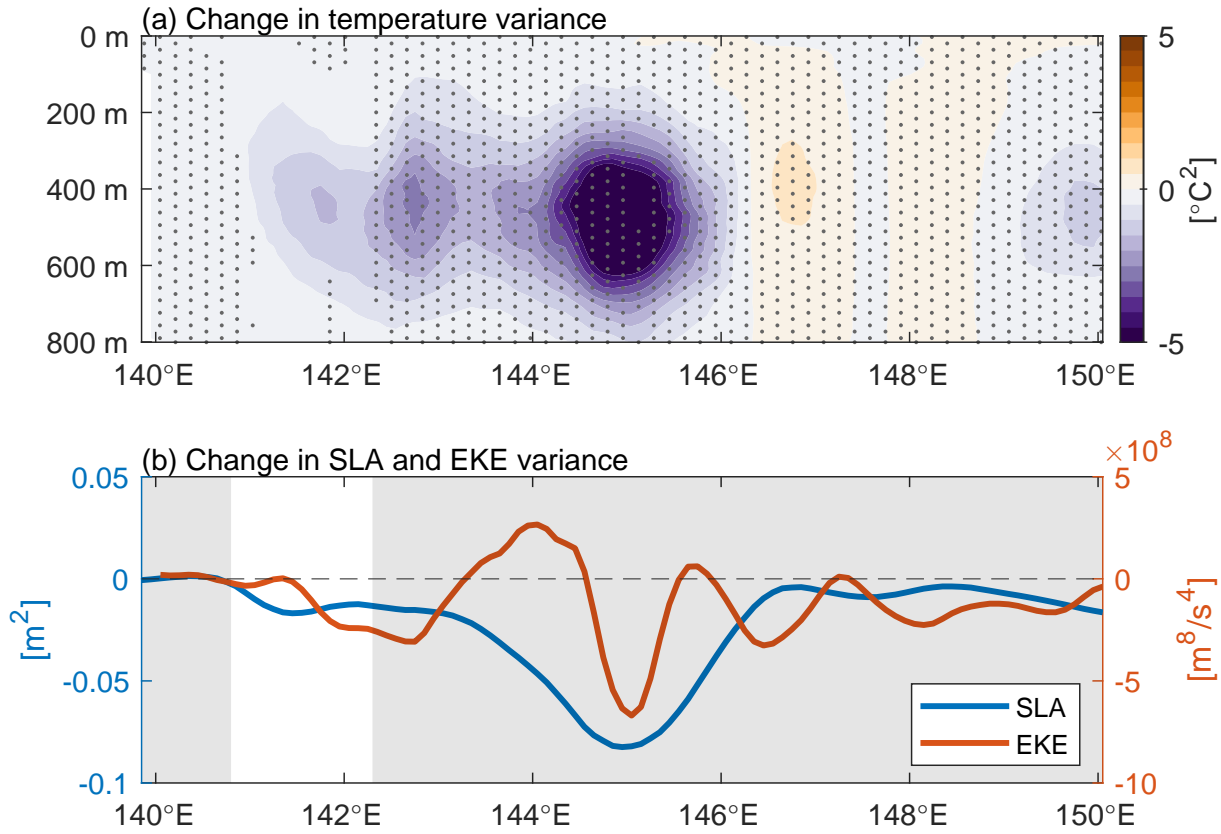


**Figure A2.1.** (a) Change in temperature anomaly variance between 1993 to 2007 and 2008 to 2022. Stippling is where the 1993 to 2022 trend in marine heatwave days per year (with temperature trend removed) is not significant at the 95% significance level (see Figure 2.6b). (b) Change in sea level anomaly (SLA, blue) variance between 1993 to 2007 and 2008 to 2022, and change in GLORYS depth-integrated velocity eddy kinetic energy (EKE, red) variance between 1993 to 2007 and 2008 to 2020. The non-shaded region is between 140.8°E and 142.3°E. For all plots, a negative value means decreased variance in the more recent time period.

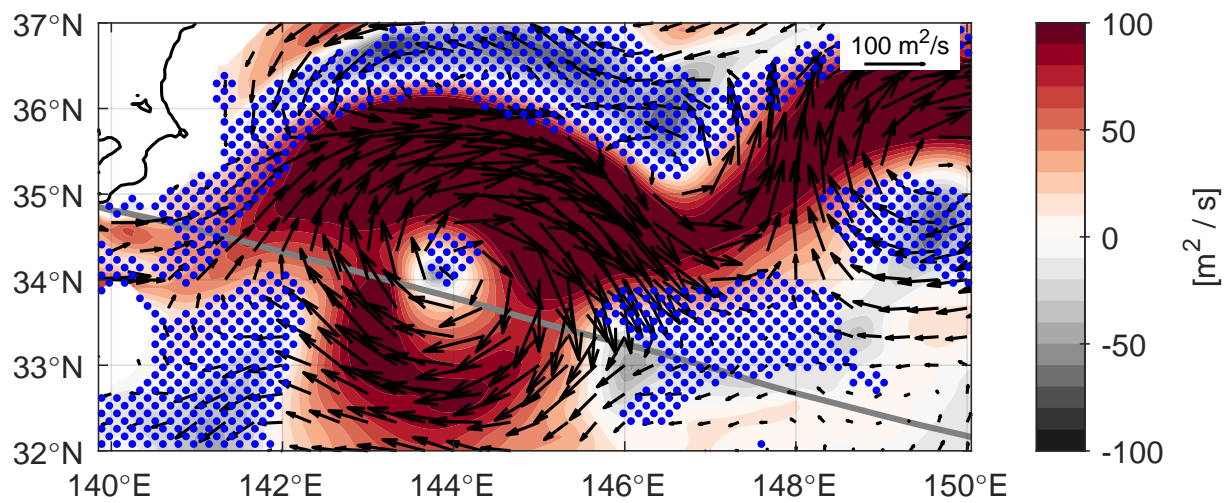


**Figure A2.2.** GLORYS depth-integrated (0-m to 800-m) velocity anomalies averaged during the longest duration (>30 days) MHW events at 144.05°E, 440-m depth. Colour and arrow scales are the same as in Figures 2.9b and 2.9c. Blue stippling is where depth-integrated speed is not significantly different from the 1993 to 2020 mean at the 95% significance level (effective degrees of freedom determined by the number of long-duration events). Thick grey line is PX40. Black contour is the Japan coastline (0-m isobath).

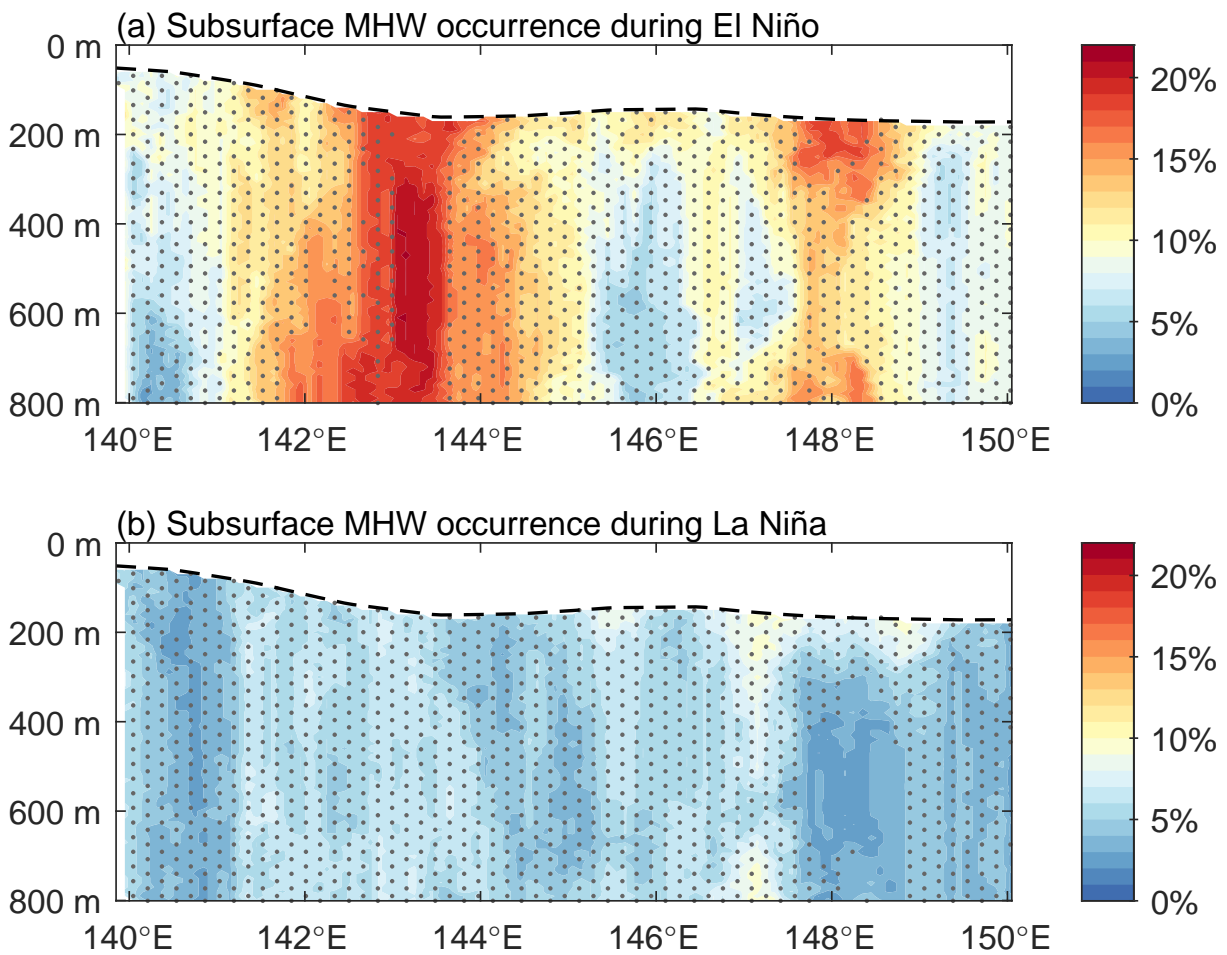


**Figure A2.3.** Percentage of time that subsurface marine heatwaves (MHWs) occurred along PX40 during (a) El Niño and (b) La Niña over the 1993 to 2022 time period when using a 20-day duration threshold. Stippling is where MHW occurrence is within the 95% confidence interval of occurrence due to chance. Black dashed line is the maximum climatological mixed layer depth.

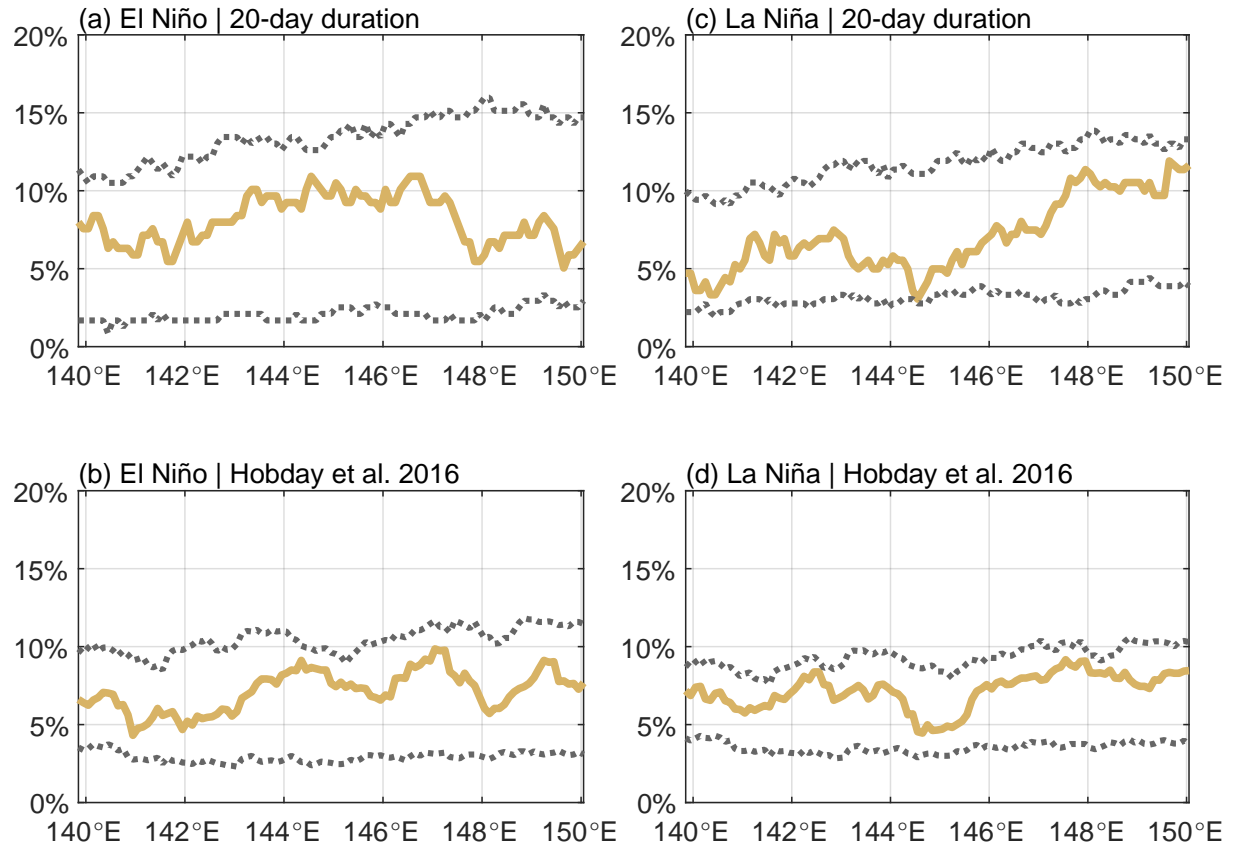


**Figure A2.4.** Percentage of time that surface marine heatwaves occurred along PX40 during (a,b) El Niño and (c,d) La Niña over the 1993 to 2022 time period when (a,c) using a 20-day duration threshold and (b,d) applying the Hobday et al. (2016) definition to daily observations. Dotted lines bound the 95% confidence interval of occurrence due to chance.

## **2.B Supplementary Text for Chapter 2**

To validate GLORYS, the reanalysis velocities were compared to monthly PX40 cross-transect absolute geostrophic velocities between 2004 and 2019 (Chandler et al. 2022a). Both GLORYS and the PX40 cross-transect velocities utilise SLA observations and are therefore not independent (Chandler et al. 2022a; Lellouche et al. 2021). Nevertheless, time-mean velocities between depths of 0-m to 800-m over the shared 2004 to 2019 period were similar in structure and magnitude, and the detrended and de-seasoned velocity time series were highly and significantly ( $p < 0.05$ ) correlated everywhere except at depth near the western boundary. This discrepancy near the western boundary appears to be caused by the core of the Kuroshio being located further offshore at depth in GLORYS. Such shifted WBC locations may be a common feature in ocean reanalyses (e.g. Zilberman et al. 2023a). Following validation, GLORYS velocities were depth-integrated between the surface and 800-m depth then detrended and de-seasoned (with time-mean retained).

# Chapter 3

## The Deep Western Boundary Current Of The Southwest Pacific Basin: Insights From Deep Argo

### 3.1 Abstract

The deep western boundary current (DWBC) of the Southwest Pacific Basin (SWPB) is the main pathway through which the deep and bottom waters formed around Antarctica are transported northward and distributed throughout the Pacific Ocean. However, historical observations of this current are sparse. Here, we used an unprecedented number of deep-ocean observations collected by Deep Argo floats since 2016 to examine temperature, salinity, and velocity in the DWBC of the SWPB. Deep Argo trajectory velocities were fastest along the western side of the Kermadec Trench, with an average velocity of  $0.057 \pm 0.012 \text{ ms}^{-1}$ . Trajectories confirmed the existence of a tight recirculation on the eastern side of the Kermadec Trench ( $-0.021 \pm 0.008 \text{ ms}^{-1}$ ). This recirculation was likewise seen in an independent eddy-resolving ocean reanalysis. For the DWBC within the northern Kermadec Trench ( $26\text{--}30^\circ\text{S}$ ), Deep Argo profiles and the ocean reanalysis demonstrated seasonal isopycnal heaving of the deep-ocean that was likely driven by local Ekman pumping and may influence seasonal DWBC transport. At the northern end of the Kermadec Trench, the deep-ocean salinity maximum was eroded as the DWBC exited the trench to the north through the Louisville Seamount Chain

collision zone, thus revealing a previously unidentified region of enhanced deep-ocean mixing. Although Deep Argo observations accurately estimated vertical turbulent diffusivity in the Samoan Passage ( $6.1 \times 10^{-3}$  to  $1.57 \times 10^{-2} \text{ m}^2 \text{ s}^{-1}$ ), mixing within the Louisville Seamount Chain collision zone was not due solely to vertical turbulent diffusivity. A global Deep Argo array could reveal wind-driven seasonal heaving and unexplored deep-ocean mixing hotspots in other DWBCs.

## 3.2 Plain Language Summary

The cold and dense seawater that fills the ocean interior is formed near the surface in polar regions. This seawater sinks and is transported away from the poles and throughout the ocean by deep western boundary currents. We used data collected by Deep Argo floats (freely drifting robots that measure temperature and salinity between the sea surface and seafloor) to examine the northward-flowing deep western boundary current in the Southwest Pacific Ocean, north-east of New Zealand. The pathway and speed of the current was identified using the horizontal movements of these floats. A clockwise circulation was evident over a deep-ocean trench (the Kermadec Trench), with some of the current's northward-flow returning southward. At the northern end of the Kermadec Trench, temperature and salinity demonstrated seasonal changes that extended at least 4000-m deep. These seasonal changes were likely caused by seasonal changes in surface winds, and may influence seasonal transport of water in the deep western boundary current. Saltier waters observed over the Kermadec Trench were not observed north of the trench, identifying the exit of the Kermadec Trench as a region of enhanced deep-ocean mixing. Implementing Deep Argo globally could reveal other unidentified regions of enhanced deep-ocean mixing.

### 3.3 Introduction

The Deep Western Boundary Currents (DWBCs) of the Southern Hemisphere are major ocean currents located on the western side of deep-ocean basins (e.g. Fukamachi et al. 2010; Purkey and Johnson 2012; Stommel and Arons 1959b; Warren 1981; Whitworth III et al. 1991, 1999). These DWBCs are the main conduit through which cold, dense water is transported away from Antarctica, filling the deep and abyssal ocean (Johnson 2008; Stommel and Arons 1959a). DWBCs are therefore a critical component of the lower cell of the meridional overturning circulation that redistributes heat, salt, carbon, nutrients, and oxygen (Sloyan et al. 2013; Talley 2013). Changes in deep and bottom water properties, due to climatic changes at high-latitude formation regions, are advected by these DWBCs, impacting climate variability (Purkey and Johnson 2010, 2013; Purkey et al. 2019), dissolved oxygen content (Gunn et al. 2023; Sloyan et al. 2013), and steric expansion and sea level (Desbruyères et al. 2016; Kouketsu et al. 2011; Purkey and Johnson 2010, 2013; Purkey et al. 2019).

Many studies of the deep-ocean have used shipboard measurements, such as those from quasi-decadal repeat hydrographic surveys (Sloyan et al. 2019). Yet observations of the deep-ocean are limited, with less than 10% of historical non-Argo temperature and salinity profiles extending below 2000-dbar (Roemmich et al. 2021). Such sparse measurements mean that DWBCs are one of the least observed large-scale circulation features in the global ocean. The recent implementation of Deep Argo floats that measure temperature, salinity, and pressure as they profile between the sea surface and as deep as 6000-dbar has afforded a new way of studying the deep-ocean (Roemmich et al. 2019a,b; Zilberman et al. 2023c). However, the spatial coverage of Deep Argo is presently restricted to a small number of regional pilot arrays (e.g. Desbruyères et al. 2022; Johnson 2022; Johnson et al. 2020, 2019; Petit et al. 2022; Racapé et al. 2019; Thomas et al. 2020; Zilberman et al. 2020).

This work is focused on the Southwest Pacific Basin (SWPB), the location of one of the pilot arrays that has been most densely sampled by Deep Argo floats. Historical studies have

suggested that the DWBC of the SWPB (Figure 3.1) flows equatorward along the Campbell Plateau, around the Chatham Rise, and through the Kermadec Trench (Reid 1986, 1997). The main DWBC pathway then becomes less clear, although the majority of flow appears to divert eastward (Warren and Voorhis 1970). Eventually, the DWBC exits the SWPB to the north, predominantly through the Samoan Passage (Roemmich et al. 1996). Velocities within the DWBC have been measured to be bottom-intensified in both the Kermadec Trench (Whitworth III et al. 1999) and Samoan Passage (Alford et al. 2013; Rudnick 1997; Voet et al. 2016, 2015).

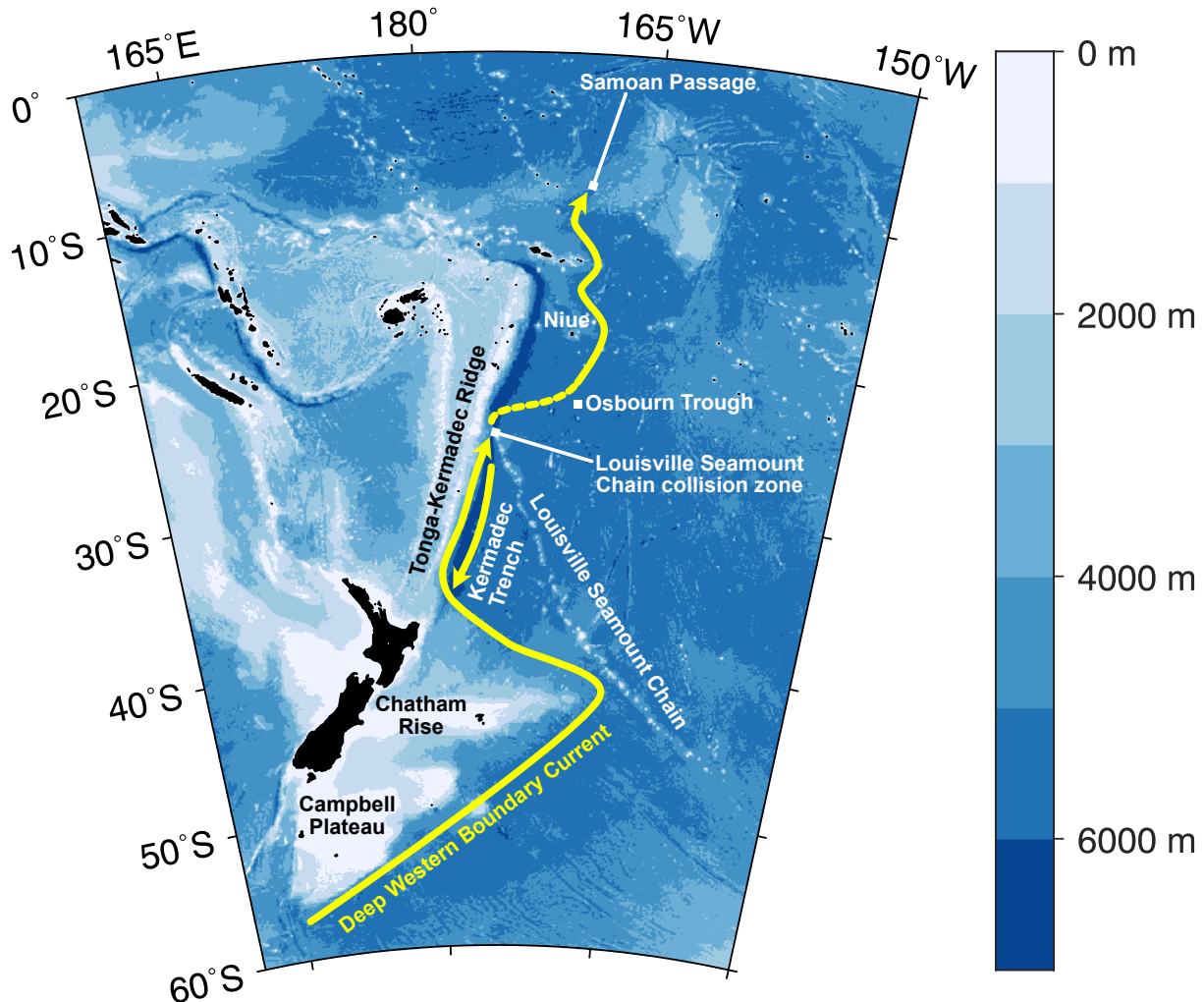


**Figure 3.1.** Bathymetry at the western boundary of the Southwest Pacific Basin with a schematic of the deep western boundary current pathway (yellow, dashed line represents an uncertain pathway). Key bathymetric features are labelled.

As there are no deep-water formation sites in the North Pacific Ocean, the SWPB DWBC

is the main pathway by which the deep and bottom waters formed around Antarctica make their way into the western South Pacific Ocean and North Pacific Ocean (Johnson 2008; Talley 2013). Specifically, this DWBC transports high oxygen and low nutrient Lower Circumpolar Deep Water (Whitworth III et al. 1999; Wijffels et al. 2001). In the SWPB, Lower Circumpolar Deep Water is composed primarily of relatively cold and fresh Antarctic Bottom Water, although a salinity maximum at shallower levels (depths of approximately 3000–4000-m at 32.5°S) reflects the influence of remnant North Atlantic Deep Water (NADW; Figure 3.2; Johnson 2008; Whitworth III et al. 1999; Wijffels et al. 2001). Above the Lower Circumpolar Deep Water lies a return flow of warmer, fresher, lower oxygen, and higher nutrient Pacific Deep Water (Whitworth III et al. 1999; Wijffels et al. 2001).

Whitworth III et al. (1999) measured the SWPB DWBC over 1991–1992 using a mooring array at 32.5°S and found a time-mean transport of 16.0 Sv ( $1 \text{ Sv} \equiv 1 \times 10^6 \text{ m}^3 \text{ s}^{-1}$ ) below 2000-m. Transport variability was large (standard deviation of 11.9 Sv), with dominant periods of variability between 40–100-days (Whitworth III et al. 1999). This large variability may be due to the influence of Rossby waves at the western boundary of the SWPB (Moore and Wilkin 1998). Further north, in the Samoan Passage, time-mean transport below 4000-m has been estimated from mooring arrays to be  $6.0 \pm 0.5$  Sv during 1992–1994 (Roemmich et al. 1996; Rudnick 1997) and  $5.4 \pm 0.6$  Sv during 2012–2013 (Voet et al. 2016). Both time series demonstrated large variability at tidal frequencies and sporadically at roughly 30-day periods, which may be related to resonance of the flow (Rudnick 1997). Roemmich et al. (1996) combined observations from the 1992–1994 mooring array with a full-depth hydrographic survey in 1994 to estimate a total mean northward transport out of the SWPB (including the Samoan Passage and other smaller transport pathways) of  $10.6 \pm 1.7$  Sv relative to the  $1.2^\circ\text{C}$  potential temperature ( $\theta$ ) surface. Transport out of the SWPB was therefore less than that measured by Whitworth III et al. (1999) in the DWBC at 32.5°S. At least part of this transport discrepancy is likely due to a broad return flow within the interior of the SWPB between 1800–4100-dbar (Zilberman et al. 2020).

Earlier studies have also hinted at a tight cyclonic circulation over the Kermadec Trench,

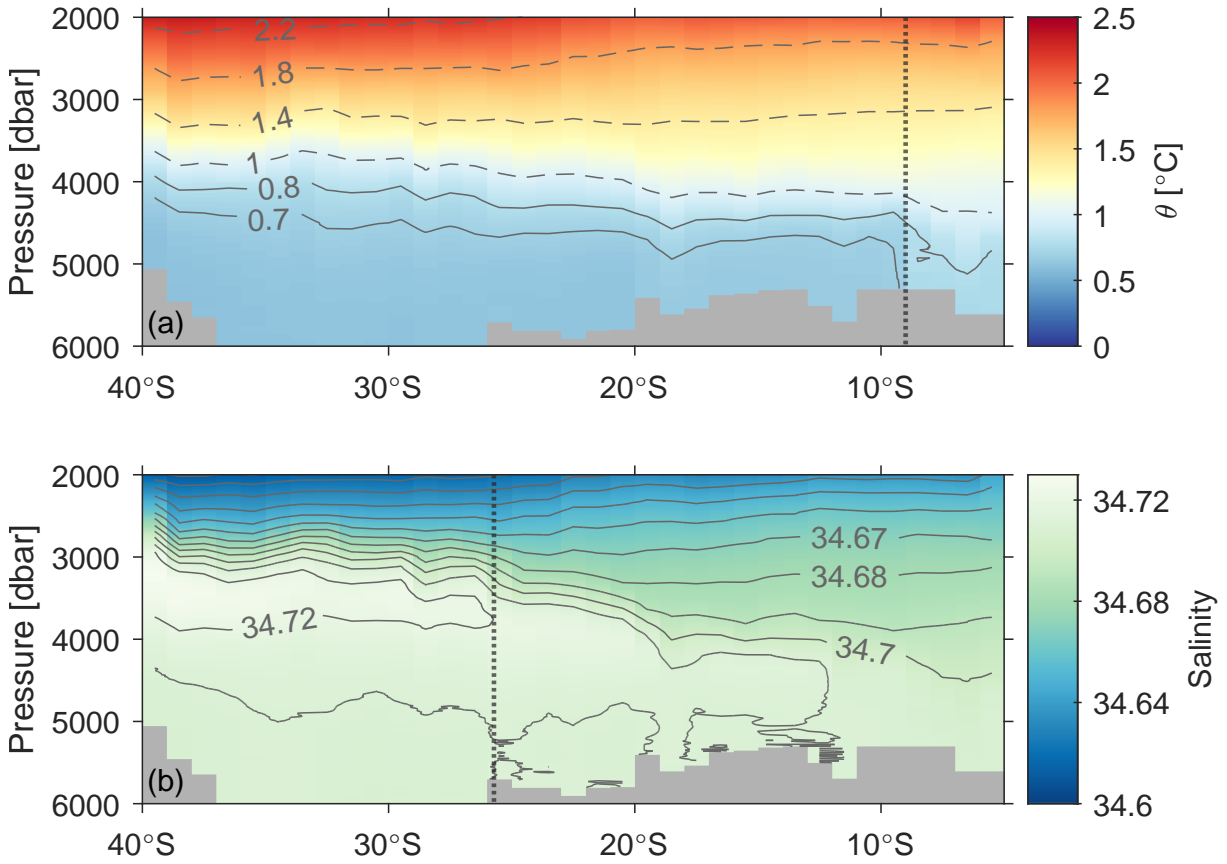


**Figure 3.2.** Meridional sections of (a) potential temperature ( $\theta$ ) and (b) salinity between 2000–6000-dbar from 1° zonal-averages of Deep Argo profiles collected at the western boundary of the Southwest Pacific Basin between June 2016 to January 2023 (see Figure 3.3 for profile locations and times). Vertical dotted lines mark the latitude of the (a) Samoan Passage ( $\sim 9^\circ\text{S}$ ) and (b) Louisville Seamount Chain collision zone ( $\sim 26^\circ\text{S}$ ).

consisting of the strong equatorward-flowing DWBC on the western flank and a weaker poleward-flowing recirculation on the eastern flank (Johnson 1998). Evidence for this recirculation has been largely based on hydrographic and velocity measurements at the  $32.5^\circ\text{S}$  mooring array, where time-mean meridional velocities on the eastern side of the trench were small but southward (on the order of  $-0.01 \text{ m s}^{-1}$ ; Whitworth III et al. 1999). A hydrographic survey at  $28^\circ\text{S}$  also suggested the presence of southward flow on the eastern side of the trench (Warren 1973), but the spatial extent of this recirculation is unresolved due to sparse historical observations. As yet, it is unknown whether the southward velocities on the eastern side of the Kermadec Trench are part of a cyclonic circulation that spans the entire trench.

As the DWBC exits the SWPB through the Samoan Passage, a large volume of water is forced over the complex bathymetry and series of sills (Alford et al. 2013). Vertical (or diapycnal) turbulent diffusivity in the Samoan Passage is therefore significantly larger than background levels in the deep-ocean ( $1 \times 10^{-5} \text{ m}^2 \text{s}^{-1}$ ; Toole et al. 1994) and the canonical basin-scale average ( $1 \times 10^{-4} \text{ m}^2 \text{s}^{-1}$ ; Munk 1966). Indeed, Roemmich et al. (1996) estimated diapycnal diffusivity in the Samoan Passage to be between  $5 \times 10^{-3}$  to  $5 \times 10^{-2} \text{ m}^2 \text{s}^{-1}$  below  $0.7^\circ\text{C}$ . More recently, Voet et al. (2015) estimated vertical turbulent diffusivities in the Samoan Passage of between  $3 \times 10^{-3}$  to  $5 \times 10^{-2} \text{ m}^2 \text{s}^{-1}$  averaged at the depth of the salinity maximum, and around  $6 \times 10^{-3} \text{ m}^2 \text{s}^{-1}$  below  $0.8^\circ\text{C}$ . However, turbulent mixing within the Samoan Passage is spatially heterogeneous (Alford et al. 2013; Voet et al. 2015), with diapycnal diffusivities as large as  $1 \times 10^{-1} \text{ m}^2 \text{s}^{-1}$  measured over the sills (Alford et al. 2013). This elevated deep-ocean turbulence mixes away the coldest and densest waters, erodes the higher salinities evident at the passage entrance, and thus sets the water mass properties of the abyssal North Pacific Ocean (Alford et al. 2013; Voet et al. 2015). We suspect there could be other such regions along the path of the SWPB DWBC where turbulent mixing is elevated, however, to the best of our knowledge, no specific locations have been identified.

Additionally, Deep Argo observations from the interior of the SWPB have suggested the presence of deep-ocean dynamic height (DH) seasonal cycles (Zilberman et al. 2020). These seasonal cycles differed between the subtropics ( $15$ – $32^\circ\text{S}$ ) and mid-latitudes ( $32$ – $46^\circ\text{S}$ ), and were hypothesised to be driven by regional Ekman pumping within the SWPB (Zilberman et al. 2020). It is unclear whether similar seasonal cycles occur in the DWBC as, at the time of Zilberman et al. (2020)'s study, there was insufficient Deep Argo coverage at the western boundary. Whitworth III et al. (1999) found no evidence of a seasonal cycle in DWBC transport at the  $32.5^\circ\text{S}$  mooring array, although the array was only deployed for 22-months. Furthermore, the array was located within the latitude range where the Ekman pumping seasonal cycle changes sign. Hence, if there is a DWBC seasonal cycle forced by Ekman pumping, it would likely not be evident at  $32.5^\circ\text{S}$ . Measurements from mooring arrays in the Samoan Passage have also been inconclusive as to the

presence of a seasonal cycle, with wavelet spectra of bottom water transport hinting at energy at the annual period (Voet et al. 2016), but again the short time series (17-months in the 1990s, 15-months in the 2010s) make determination of any seasonal cycle difficult.

Continued Deep Argo deployments in the SWPB have increased coverage of the western boundary in recent years. This blossoming data set can now be leveraged to provide new insights that were not previously feasible using sparse historical observations. In the present study we have examined flow pathways, turbulent mixing, and seasonality in the DWBC of the SWPB using 964 Deep Argo profiles and 711 Deep Argo trajectories collected since 2016. These observations allowed us to trace the path of the DWBC and, for the first time, clearly show the cyclonic recirculation over the entire Kermadec Trench. Deep Argo profiles revealed that the remnant NADW salinity maximum is eroded as the DWBC exits the Kermadec Trench to the north, marking the Louisville Seamount Chain collision zone as a previously unidentified deep-ocean mixing hotspot. We found seasonal isopycnal heaving in the northern Kermadec Trench, and suggest this deep-ocean heaving is forced by the local Ekman pumping seasonal cycle at the surface. In the remainder of this paper we outline the data and methods used (section 3.4), present our results (section 3.5), and discuss their implications (section 3.6).

## 3.4 Data and Methodology

### 3.4.1 Deep Argo Profiles and Trajectories

Data were collected by 10 Deep Argo floats profiling within the DWBC of the SWPB (Figure 3.3). All floats were the Deep SOLO model capable of profiling down to 6000-dbar (Roemmich et al. 2019b). Following initial diagnostic cycles on deployment (Roemmich et al. 2019b), these floats were set to 10-day or 15-day profiling cycles. Only delayed-mode profiles with adjusted temperature, salinity, and pressure flagged as ‘good’ or ‘probably good’ (Wong et al. 2022) were used in this study. Profiles shallower than 2000-db or outside of the latitudinal range 5–40°S were excluded, which resulted in a total of 964 profiles since June 2016 with the most

recent delayed-mode profile from January 2023. As the vertical resolution within and between float profiles varied (from near-continuous to 60-dbar), all profiles were linearly interpolated to a 10-dbar pressure grid (e.g. Foppert et al. 2021; Johnson et al. 2020). Temperature was converted to  $\theta$  (relative to the sea surface, i.e. 0-dbar).

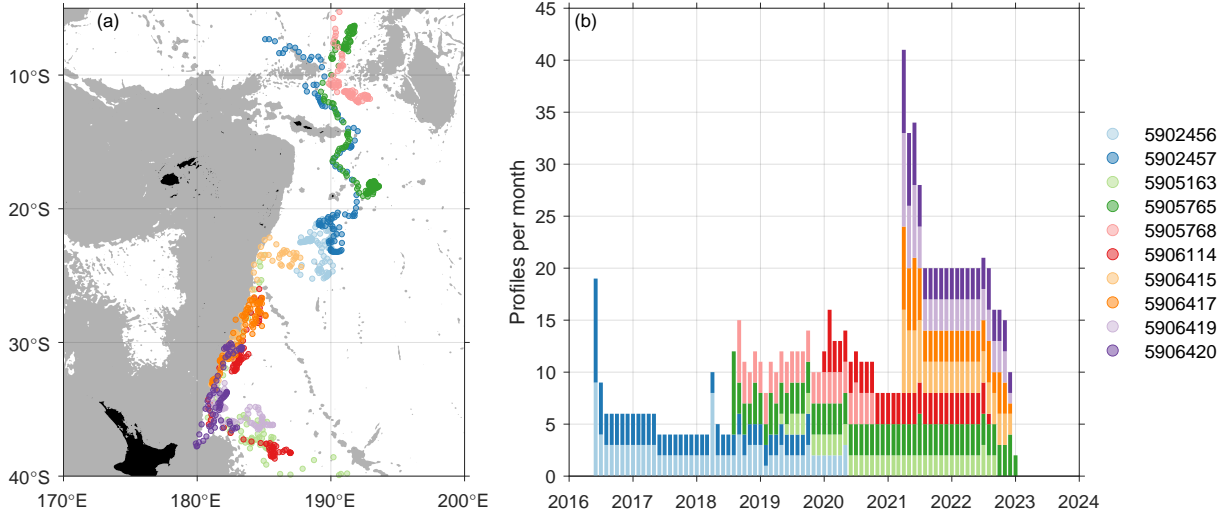


**Figure 3.3.** (a) Locations of Deep Argo profiles and (b) number of Deep Argo profiles per month, both coloured according to float WMO identification number. Grey shading is bathymetry shallower than 4000-m.

Deep Argo has target accuracies of  $\pm 3$ -dbar for pressure,  $\pm 0.001^\circ\text{C}$  for temperature, and  $\pm 0.002$  PSS-78 for salinity (Roemmich et al. 2019a). Efforts are ongoing to achieve these targets, with prior observations indicating that the SBE-61 CTDs carried by Deep SOLO floats have accuracies of  $\pm 4.5$ -dbar for pressure,  $\pm 0.001^\circ\text{C}$  for temperature, and  $\pm 0.005$  for salinity (Roemmich et al. 2019a). A compressibility correction of the conductivity cell that improves salinity accuracy to  $\pm 0.002$  (Foppert et al. 2021; Zilberman et al. 2023c) was applied to the delayed-mode profiles here.

The Scripps Argo Trajectory-Based Velocity Product provides trajectories for all delayed-mode quality-controlled Argo floats with parking pressures between 100–6200-dbar and profiling cycles between 5–25-days over the period 2001–2022 (Zilberman et al. 2023a). These subsurface trajectory velocities were computed based on the float's drift distance and duration each profiling

cycle (Zilberman et al. 2023a). This product was used to obtain trajectories for the 10 Deep Argo floats in the DWBC. Most of the 711 Deep Argo trajectories (at time of writing, the product did not contain delayed-mode trajectories for floats 5906417, 5906419, or 5906420) were from floats parked at pressures around 5000-dbar (75% were between 4500–5500-dbar). The shallowest trajectory parking pressure was 2520-dbar and the deepest was 5909-dbar.

### 3.4.2 Ocean Reanalysis

The  $1/12^{\circ}$  Global Ocean Physics Reanalysis (GLORYS12V1, hereafter GLORYS; Lellouche et al. 2021) was used for comparison with Deep Argo profiles of temperature and salinity and Deep Argo subsurface trajectory velocities in the Kermadec Trench. GLORYS assimilates reprocessed and quality-controlled satellite observations of sea level anomaly, sea surface temperature, and sea ice concentration, as well as in situ observations of temperature and salinity (Lellouche et al. 2021). Deep Argo observations are not yet included in the reanalysis, with (non-Argo) climatological temperature and salinity assimilated below 2000-m (Lellouche et al. 2018). As such, the Deep Argo and GLORYS data used here are independent of each other.

GLORYS can be used to examine variability from meso-scale to global-scale over time periods from days to decades (Lellouche et al. 2021). Previously, Song et al. (2023) used GLORYS to examine seasonality in the southward-flowing Philippine Trench DWBC and found that GLORYS successfully reproduced velocity variability, albeit with stronger velocities than observed. Here, monthly means of GLORYS  $\theta$  and salinity between depths of 1940–5730-m and in the region bounded by  $25\text{--}40^{\circ}\text{S}$ ,  $179\text{--}185^{\circ}\text{E}$  were downloaded for the period 1993–2020. The GLORYS time series therefore had limited overlap with the period of Deep Argo observations. Nevertheless, Deep Argo profiles and GLORYS  $\theta$  and salinity profiles (time-averaged for the month in which the corresponding Deep Argo profile was measured) were similar (Figure 3.4). Although, compared to Deep Argo observations, GLORYS underestimated the salinity maximum, overestimated salinity in the coldest waters, and had colder bottom waters. GLORYS zonal and meridional velocities at 5275-m (the depth level closest to the largest number of Deep Argo

trajectory parking pressures) were also downloaded for the same time period and region.

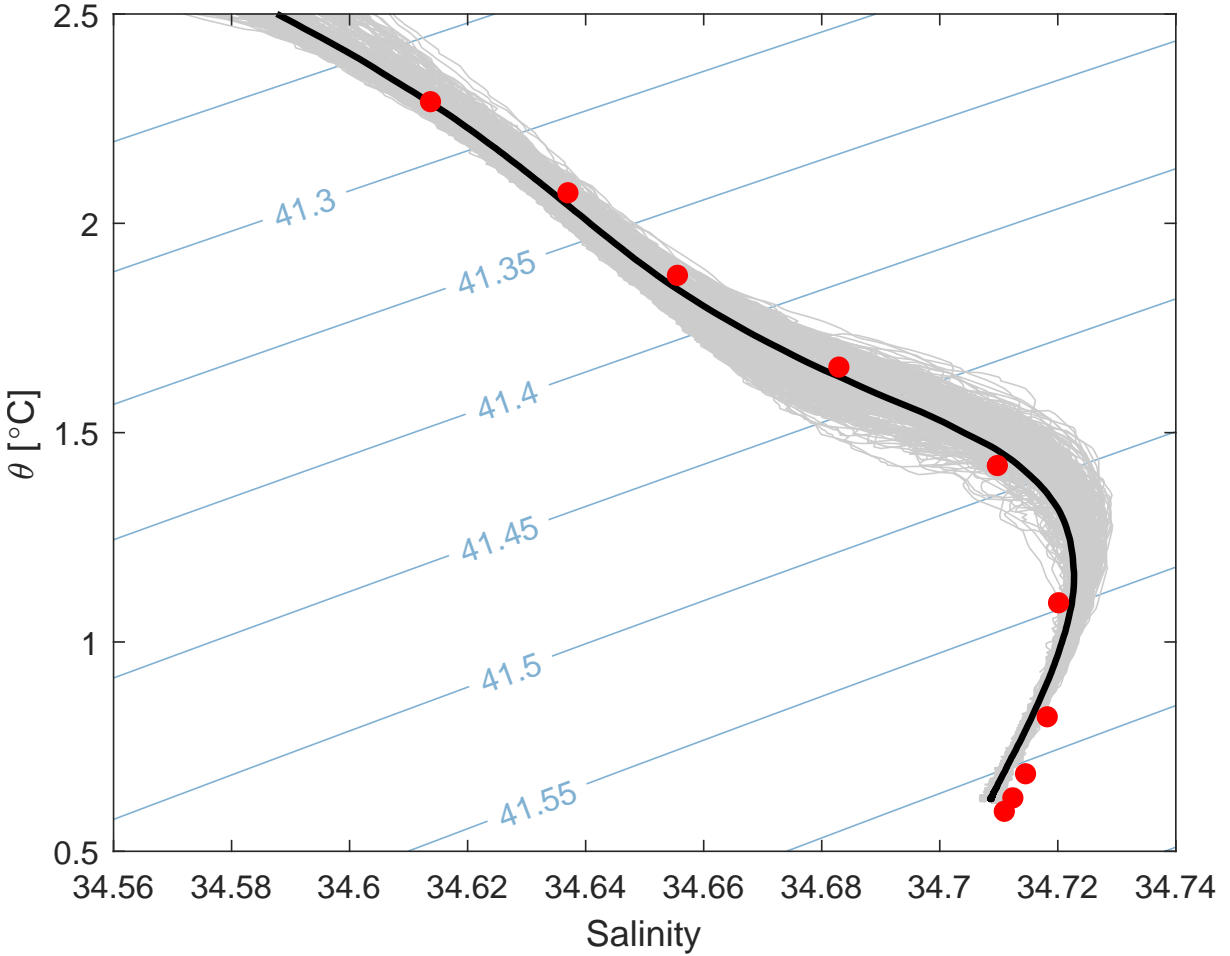


**Figure 3.4.** Potential temperature ( $\theta$ ) – salinity curves for all Deep Argo profiles in the Kermadec Trench (grey lines), the spatial-average of these Deep Argo profiles (black line), and the spatial-average of the GLORYS profiles interpolated to the locations of the Deep Argo profiles (red dots), with  $\sigma_3$  (potential density anomaly referenced to 3000-dbar;  $\text{kg m}^{-3}$ ) contours in blue. Each GLORYS profile was the 1993–2020 time-average for the month in which the corresponding Deep Argo profile (December 2019 to December 2022) was measured.

### 3.4.3 Ekman Pumping

Monthly ERA5 (Hersbach et al. 2020) wind stress was downloaded for 1993–2020, the same time period as GLORYS, and used to compute Ekman pumping ( $w_{Ek}$ ):

$$w_{Ek} = \frac{\frac{\partial \tau^y}{\partial x} - \frac{\partial \tau^x}{\partial y}}{\rho_0 f} \quad (3.1)$$

where  $\tau^y$  is meridional wind stress,  $\tau^x$  is zonal wind stress,  $x$  is zonal distance,  $y$  is meridional distance,  $\rho_0$  is a representative surface density ( $1025 \text{ kg m}^{-3}$ ), and  $f$  is the Coriolis parameter (e.g. Cushman-Roisin and Beckers 2011). Ekman pumping seasonal cycles were obtained by least-squares fitting annual and semi-annual harmonics and a mean, then subtracting the fitted mean.

### 3.4.4 Turbulent Mixing

Vertical turbulent diffusivity ( $\kappa_z$ ) was examined in the Samoan Passage and in the Louisville Seamount Chain collision zone. These two locations are bathymetric choke-points along the path of the DWBC (Figure 3.1) where substantial changes in water mass properties were observed (Figure 3.2). To estimate  $\kappa_z$ , the equation for conservation of a tracer  $C$  (either  $\theta$  or salinity), with no sources or sinks, small aspect ratio (vertical scale much smaller than horizontal scale), horizontal changes only in the along-flow direction (no  $x$ -direction terms), and constant vertical turbulent diffusivity was used (e.g. Ffield and Gordon 1992; Salmon 1998; Voet et al. 2015).

In a reference frame moving with the flow, the conservation equation becomes (Ffield and Gordon 1992):

$$\frac{\partial C}{\partial t} = \kappa_z \frac{\partial^2 C}{\partial z^2} \quad (3.2)$$

where  $t$  is time and  $z$  is depth. Following Voet et al. (2015), equation 3.2 was applied to the mean  $\theta$  and salinity profiles immediately upstream (within  $2.7^\circ$  of latitude) of each region and solved numerically using forward differencing. In the Samoan Passage,  $C$  was held constant at 3600-m and a no flux boundary condition applied at the bottom. In the Louisville Seamount Chain collision zone,  $C$  was held constant at both 2400-m and 3800-m. Model results depend on the spreading scale parameter  $\lambda = \sqrt{\kappa_z t^*}$ , where  $t^* = \frac{y}{v}$  is the transit time through the choke-point with  $y$  the distance between the mean location of downstream and upstream profiles and  $v$  the mean Deep Argo trajectory velocity within the choke-point. Here,  $\lambda$  was taken to be the value

that minimised the difference between the modelled  $\theta$ -salinity profile and the mean profile observed downstream.

In a stationary reference frame and assuming a steady-state, the conservation equation instead becomes:

$$v \frac{\partial C}{\partial y} = \kappa_z \frac{\partial^2 C}{\partial z^2} \quad (3.3)$$

Three of the terms in equation 3.3 ( $v$ ,  $\frac{\partial C}{\partial y}$ ,  $\frac{\partial^2 C}{\partial z^2}$ ) could be obtained from Deep Argo observations, allowing  $\kappa_z$  to be computed from direct observations. This calculation was only performed in the Samoan Passage, where the numerical model (equation 3.2) reproduced a  $\theta$ -salinity profile exceptionally similar to the mean observed downstream profile (Figure A3.1). Each term in equation 3.3 was averaged below 4000-dbar (about 1.1°C), where the observed  $\theta$ -salinity curves upstream and downstream of the Samoan Passage diverged, and  $\kappa_z$  was computed for both salinity and  $\theta$  observations. The calculation was not performed in the Louisville Seamount Chain collision zone as the modelled profile evolution did not match the mean  $\theta$ -salinity profile observed downstream (Figure A3.2), indicating that additional mixing processes other than just  $\kappa_z$  are important.

For both the numerical model and direct calculation, a bootstrapping approach was employed to compute 95% confidence intervals. Mean profiles, locations, and velocities were recomputed by sampling with replacement, and  $\kappa_z$  was recalculated using these new values. This procedure was repeated  $1 \times 10^4$  times and the 2.5th and 97.5th percentile values of  $\kappa_z$  taken to represent the 95% confidence interval.

### 3.4.5 Seasonality

Deep Argo profiles in the DWBC along the Kermadec Trench were used to examine  $\theta$ , salinity, and DH seasonal cycles in the deep-ocean. These profiles were identified using Deep Argo trajectories to select a region that encompassed just the northward flow on the western side of the trench (between 26–38°S). Profiles were spatially-averaged each month to

produce monthly time series for 2021–2022. To obtain seasonal cycles, annual and semi-annual harmonics and a mean were least-squares fit to the monthly time series. The mean was then subtracted from the least-squares fit. Seasonal cycles were computed between 2000–4000-dbar as 80% of profiles considered reached at least 4000-dbar. DH was thus computed relative to 4000-dbar and the 20% of profiles that did not reach 4000-dbar were excluded. No profiles were excluded from the  $\theta$  and salinity seasonal cycles. As such, the number of profiles contributing to the spatial-average each month ranged from 3–26 (average of 8.8 profiles) for  $\theta$  and salinity, and from 0–15 (average of 7.0, with 0 profiles only occurring for one month) for DH. Observed  $\theta$ , salinity, and DH seasonal signals were larger than Deep Argo measurement accuracies ( $\pm 0.002$  for salinity,  $\pm 0.001^\circ\text{C}$  for temperature,  $\pm 4.5$ -dbar for pressure, and  $\pm 0.043 \text{ m}^2 \text{s}^{-2}$  for DH at 2000-dbar relative to 4000-dbar).

To examine the cause of deep-ocean seasonality, the  $\theta$  seasonal cycle was decomposed into heave ( $\theta'_{\text{heave}}$ , i.e. changes on pressure surfaces due to isopycnal displacement) and spice ( $\theta'_{\text{spice}}$ , i.e. changes on isopycnal surfaces due to water mass property changes) components (Bindoff and McDougall 1994; Desbruyères et al. 2022; Häkkinen et al. 2015):

$$\theta' = \underbrace{\theta'_{\text{spice}}|_\rho}_{\theta'_{\text{spice}}} + \underbrace{\frac{d\theta}{dp} p'|_\rho}_{\theta'_{\text{heave}}} \quad (3.4)$$

where  $p$  is pressure, and  $X'|_\rho$  means the seasonal cycle of  $X$  on an isopycnal. Following Desbruyères et al. (2022), a  $\sigma_3$  (potential density anomaly referenced to 3000-dbar) vertical grid was constructed encompassing the depth range 2000–4000-dbar. For the spice component,  $\theta$  was linearly interpolated onto the  $\sigma_3$  grid and  $\theta'_{\text{spice}}$  computed. For the heave component,  $\frac{d\theta}{dp}$  and  $p$  were linearly interpolated onto the  $\sigma_3$  grid and  $p'|_\rho$  was multiplied by the  $\frac{d\theta}{dp}$  seasonal cycle (with mean retained) to obtain  $\theta'_{\text{heave}}$ . Both  $\theta'_{\text{spice}}$  and  $\theta'_{\text{heave}}$  were linearly interpolated back to the original pressure grid. The coefficient of determination ( $R^2$ ) was used to evaluate the contribution of each term to the total  $\theta$  seasonal cycle.

Seasonality was also computed using GLORYS interpolated to the locations of the Deep Argo profiles. The procedure was much the same as for Deep Argo, but every location had monthly  $\theta$ , salinity, and DH over 1993–2020. Therefore, after spatial-averaging, time series were detrended before seasonal cycles were computed. Additionally, as local  $w_{Ek}$  seasonal cycles changed sign within the meridional range of the Kermadec Trench, GLORYS was used to compute seasonal cycles of  $\theta$ , salinity, and DH along the DWBC in northern (26–30°S) and southern (32–36°S) trench regions.

## 3.5 Results

### 3.5.1 Deep Western Boundary Current Pathway

Deep Argo float trajectories illustrated the path of the DWBC through the SWPB in unprecedented detail (Figure 3.5). Beginning at 40°S, trajectories were northwest along the northern flank of the Chatham Rise (see Figure 3.1 for locations of bathymetric features) until reaching the Tonga-Kermadec Ridge, at which point they turned equatorward alongside the ridge. A clear recirculation of flow was evident over the Kermadec Trench, with poleward trajectories along the eastern side of the trench (Figure 3.5b). Continuing equatorward, trajectories exited the Kermadec Trench through the Louisville Seamount Chain collision zone. Trajectory directions were incoherent within the Osbourn Trough, suggesting the DWBC may break up into an eddy field here. On the northern side of the trough, around the latitude of Niue, trajectories re-coalesced into a coherent equatorward flow approximately following the 5000-m isobath before exiting the SWPB through the Samoan Passage (Figure 3.5c).

Trajectory velocities within the two coherent regions of equatorward flow were stronger in the Kermadec Trench than between Niue and the Samoan Passage, with an average velocity (over all parking pressures) of  $0.057 \pm 0.012 \text{ ms}^{-1}$  (95% confidence interval computed using a bootstrapping approach) compared to  $0.031 \pm 0.005 \text{ ms}^{-1}$ . The poleward-flowing recirculation over the Kermadec Trench ( $-0.021 \pm 0.008 \text{ ms}^{-1}$ ) was also weaker than the equatorward-

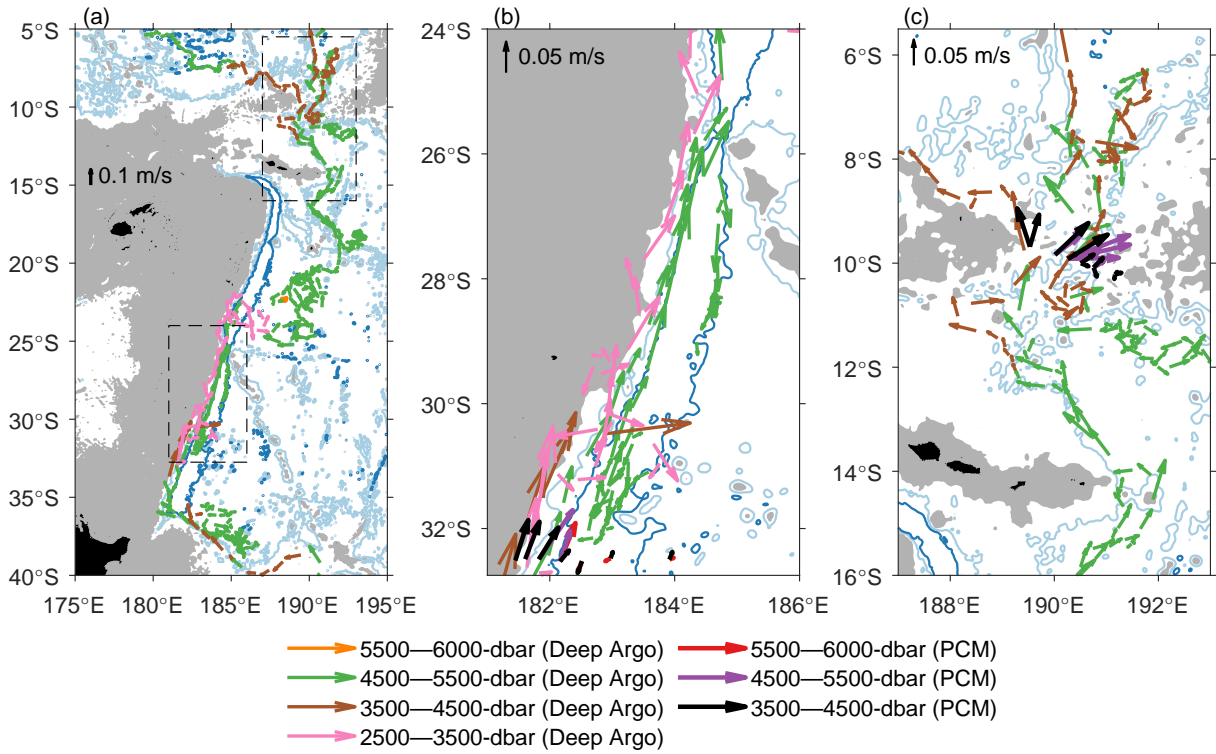


**Figure 3.5.** (a) Deep Argo trajectory velocities (July 2016 to December 2022) in the deep western boundary current of the Southwest Pacific Basin. Dashed boxes in (a) are presented in the following panels with Deep Argo trajectory velocities and historical time-mean velocities from WOCE mooring array (b) PCM9 (February 1991 to December 1992) in the Kermadec Trench and (c) PCM11 (September 1992 to February 1994) in the Samoan Passage. Velocities are grouped by depth (parking pressure for Deep Argo, instrument depth for mooring arrays). Note the 5500–6000-dbar Deep Argo trajectories are small and only located near 22°S. Bathymetry contours are 5000-m (light blue) and 6000-m (dark blue), grey shading is shallower than 4000-m.

flowing DWBC. The average velocity in the Samoan Passage was  $0.020 \pm 0.010 \text{ ms}^{-1}$ . Deep Argo trajectories were the same order of magnitude and consistent in direction with time-mean velocities from moored current meters at PCM9 in the Kermadec Trench over February 1991 to December 1992 (Figure 3.5b; Whitworth III et al. 1999) and PCM11 in the Samoan Passage over September 1992 to February 1994 (Figure 3.5c; Rudnick 1997).

The Kermadec Trench DWBC and recirculation were also present in an eddy-resolving ocean reanalysis. GLORYS time-mean velocities over 1993–2020 at 5275-m depth demonstrated strong equatorward velocities on the western side of the trench and weaker poleward velocities on the eastern side (Figure 3.6a), qualitatively similar to Deep Argo trajectory velocities over 2021–

2022 (Figures 3.5b and 3.6b). However, GLORYS tended to overestimate speed in the southern Kermadec Trench and underestimate speed in the northern Kermadec Trench (Figures 3.6b and 3.6c). This discrepancy in speed moving along the trench could be due to semi-permanent eddies or smaller recirculation features that were evident in the GLORYS time-mean DWBC velocity field (e.g. between roughly 35.2–34.4°S, 33.6–32.8°S, and 31.1–30.5°S). These features may produce localised recirculations of flow such that total mass transport decreases moving northward, which could present as a slowdown of the current. Indeed, the largest time-mean GLORYS meridional velocities were found at the southern end of the Kermadec Trench. The limited number of Deep Argo trajectories and the different time periods likely also contributed to the discrepancy between Deep Argo and GLORYS velocities.

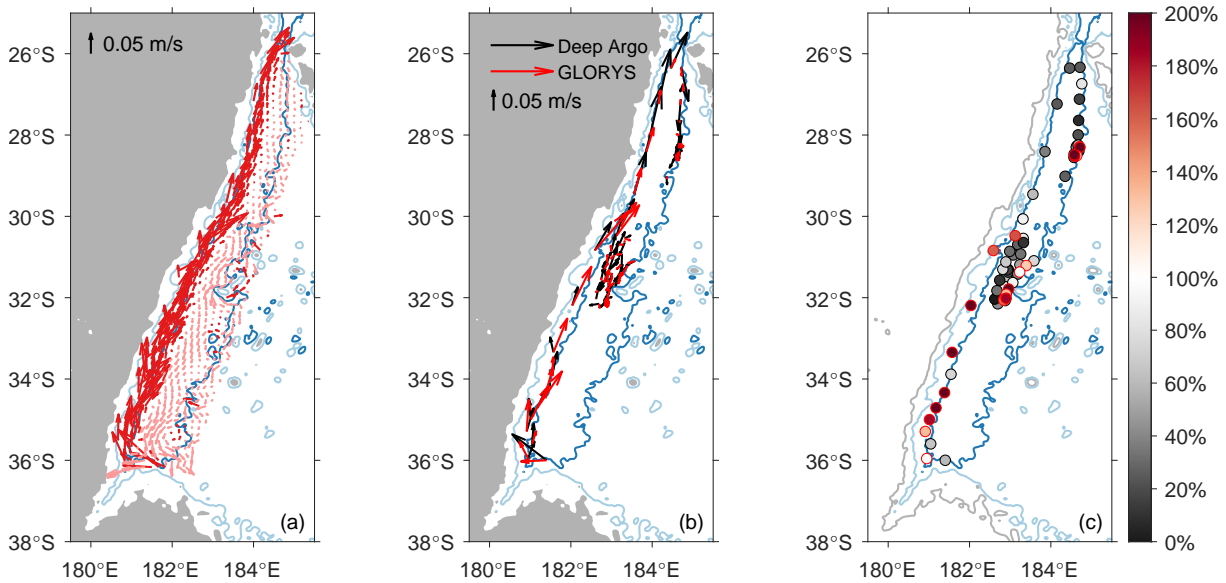


**Figure 3.6.** (a) GLORYS time-mean velocity in the Kermadec Trench over 1993–2020 at 5275-m (plotted at 1/6° resolution). Red arrows are positive meridional velocities, pink arrows are negative. (b) Comparison of Deep Argo trajectory velocity (black arrows) in the Kermadec Trench between 4500–5500-dbar over 2021–2022 and GLORYS velocity (red arrows) at 5275-m interpolated to the Deep Argo trajectory locations and time-averaged over 1993–2020 for the month in which the corresponding Deep Argo trajectory was obtained. (c) Comparison of the speed (magnitude only) of the Deep Argo trajectories and GLORYS velocities from (b) showing the percent that GLORYS speed is of Deep Argo trajectory speed (red means GLORYS is faster, black means Deep Argo is faster). Bathymetry contours are 4000-m (grey), 5000-m (light blue), and 6000-m (dark blue), with grey shading shallower than 4000-m.

### 3.5.2 Turbulent Mixing

Substantial changes in DWBC  $\theta$  and salinity properties were observed between Deep Argo profiles upstream (south) and downstream (north) of both the Louisville Seamount Chain collision zone and the Samoan Passage (Figure 3.2). The highest mean salinities in the DWBC ( $\geq 34.72$ ) were eroded away as the DWBC exited the Kermadec Trench through the Louisville Seamount Chain collision zone, with such high mean salinities not evident to the north (Figure 3.2b). The largest  $\theta$ -salinity differences at the collision zone occurred between roughly 1.2–1.7°C (approximately 2700–3500-dbar), where upstream profiles were substantially saltier at a given temperature than downstream profiles (Figure A3.2). This depth range is within the strong northward flow of the DWBC (Figure 3.5b; Whitworth III et al. 1999). Property changes through the Samoan Passage have been previously documented (e.g. Alford et al. 2013; Voet et al. 2015) and are therefore not discussed here.

The observed  $\theta$ -salinity changes at the Louisville Seamount Chain collision zone and Samoan Passage imply substantial deep-ocean mixing, which could be due to vertical turbulent diffusivity. In the Louisville Seamount Chain collision zone, the modelled (equation 3.2) evolution of the mean upstream  $\theta$ -salinity profile due to vertical turbulent diffusivity was rather different from the mean profile observed downstream (Figure A3.2). This mismatch between modelled and observed downstream profiles occurred for all spreading scales ( $\lambda$ ) and was not dependent on the upper and lower model boundary depths. However, in the Samoan Passage, the modelled evolution due to vertical turbulent diffusivity was exceptionally similar to downstream observations (Figure A3.1). A spreading scale of  $\lambda = 398\text{-m}$  provided the best match between the modelled and mean observed downstream  $\theta$ -salinity profiles, which, for a distance between mean upstream and downstream profile locations of 504.4-km and a mean Deep Argo trajectory velocity within the Samoan Passage of  $0.020 \text{ m s}^{-1}$ , resulted in a vertical turbulent diffusivity of  $6.2 \times 10^{-3} \text{ m}^2 \text{ s}^{-1}$  (95% confidence interval =  $2.9 \times 10^{-3}$  to  $1.00 \times 10^{-2} \text{ m}^2 \text{ s}^{-1}$ ). Consistent with the model, vertical turbulent diffusivity in the Samoan Passage (below 4000-

dbar) from Deep Argo observations (equation 3.3) was estimated to be  $1.57 \times 10^{-2} \text{ m}^2 \text{s}^{-1}$  ( $7.2 \times 10^{-3}$  to  $2.64 \times 10^{-2} \text{ m}^2 \text{s}^{-1}$ ) based on conservation of  $\theta$  and  $6.1 \times 10^{-3} \text{ m}^2 \text{s}^{-1}$  ( $2.1 \times 10^{-3}$  to  $2.32 \times 10^{-2} \text{ m}^2 \text{s}^{-1}$ ) based on conservation of salinity (Figure 3.7).

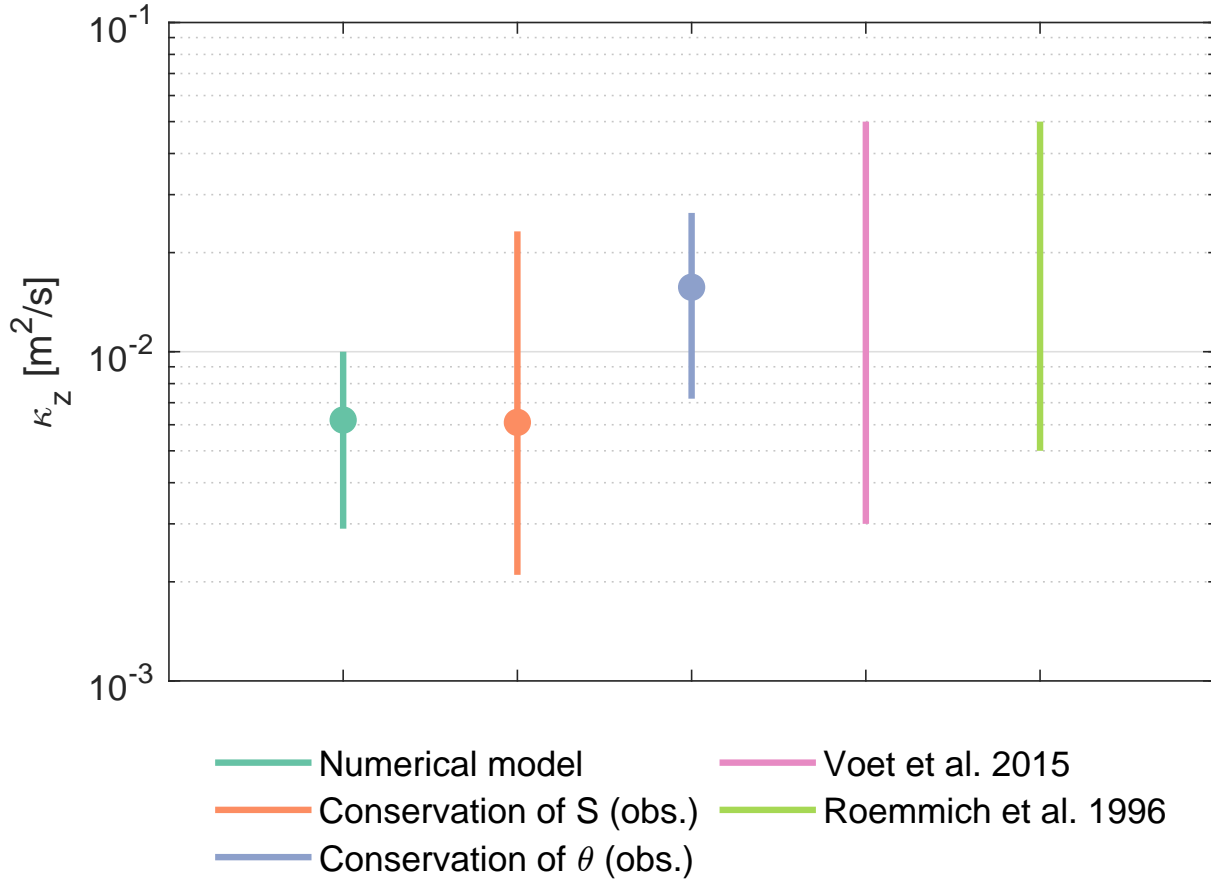


**Figure 3.7.** Estimates of vertical turbulent diffusivity ( $\kappa_z$ ) through the Samoan Passage from a numerical model applied to upstream Deep Argo observations (aquamarine), and computed from conservation of salinity (orange) and potential temperature (purple) using Deep Argo observations. Filled circles use all Deep Argo data, lines represent bootstrapped 95% confidence intervals. Pink and light-green lines are the range of  $\kappa_z$  estimates through the Samoan Passage from Voet et al. (2015) and Roemmich et al. (1996).

Deep Argo estimates of vertical turbulent diffusivity through the Samoan Passage (from both the numerical model and from direct observations) were also consistent with prior estimates in the Samoan Passage (Figure 3.7). Using a heat budget approach, Roemmich et al. (1996) estimated diapycnal turbulent diffusivity below  $0.7^\circ\text{C}$  to be between  $5 \times 10^{-3}$  to  $5 \times 10^{-2} \text{ m}^2 \text{s}^{-1}$ . Waters colder than  $0.7^\circ\text{C}$  were not present north of the Samoan Passage (Figure 3.2a), consistent

with these earlier observations, but below 4750-dbar (the depth closest to  $0.7^{\circ}\text{C}$  in the average profile south of the Samoan Passage) we estimated a vertical turbulent diffusivity of  $5.09 \times 10^{-2} \text{ m}^2 \text{ s}^{-1}$  ( $2.08 \times 10^{-2}$  to  $1.358 \times 10^{-1} \text{ m}^2 \text{ s}^{-1}$ ) based on conservation of  $\theta$  (equation 3.3). This estimate is at the upper bound of the estimate by Roemmich et al. (1996), but is not unrealistically large for the Samoan Passage (Alford et al. 2013). Voet et al. (2015) used a numerical model (equation 3.2) to estimate a vertical turbulent diffusivity of between  $3 \times 10^{-3}$  to  $5 \times 10^{-2} \text{ m}^2 \text{ s}^{-1}$  averaged over a depth range comparable to our estimate. Voet et al. (2015) also used Thorpe scales (Dillon 1982; Thorpe 1977) to estimate a diapycnal turbulent diffusivity of  $6 \times 10^{-3} \text{ m}^2 \text{ s}^{-1}$  below  $0.8^{\circ}\text{C}$ . Implementation of Thorpe scales was not feasible in the present study as Deep Argo profiles often had vertical resolutions of the same magnitude or coarser than the Thorpe length scales found in the Samoan Passage by Voet et al. (2015). However, we estimated vertical turbulent diffusivity below 4440-dbar (the depth closest to  $0.8^{\circ}\text{C}$  in the average profile south of the Samoan Passage) to be  $8.4 \times 10^{-3} \text{ m}^2 \text{ s}^{-1}$  ( $3.8 \times 10^{-3}$  to  $1.41 \times 10^{-2} \text{ m}^2 \text{ s}^{-1}$ ) based on conservation of  $\theta$  and  $4.4 \times 10^{-3} \text{ m}^2 \text{ s}^{-1}$  ( $1.3 \times 10^{-3}$  to  $2.35 \times 10^{-2} \text{ m}^2 \text{ s}^{-1}$ ) based on conservation of salinity, consistent with the estimate by Voet et al. (2015).

### 3.5.3 Kermadec Trench Seasonality

Deep-ocean seasonal cycles of DH, salinity, and  $\theta$  between 2000–4000-dbar were identified from the 2-year time series (2021–2022) of Deep Argo profiles spanning the length of the Kermadec Trench DWBC (between  $26\text{--}38^{\circ}\text{S}$ ). DH (Figure 3.8a) was negative (i.e. steric contraction) between January–July and positive (i.e. steric expansion) between July–January. The largest signals (at 2000-dbar relative to 4000-dbar) of  $-0.147 \text{ m}^2 \text{ s}^{-2}$  and  $0.129 \text{ m}^2 \text{ s}^{-2}$  occurred in April and November respectively. Salinity (Figure 3.8b) appeared to be influenced by the vertical movement of the remnant NADW salinity maximum (at approximately 3500-dbar in the annual average), causing both positive (i.e. saltier) and negative (i.e. fresher) signals to be present each month. The saltiest signal of 0.013 occurred in March and the freshest signal of  $-0.010$  occurred in November, both around 2900-dbar. Broadly speaking,  $\theta$  (Figure 3.8c)

was negative (i.e. colder) in February–June and positive (i.e. warmer) in July–January, with the coldest signal of  $-0.062^{\circ}\text{C}$  in April at approximately 3300-dbar and the warmest signal of  $0.042^{\circ}\text{C}$  in December at approximately 3200-dbar. The onset of the cold signal shifted later with decreasing pressure and there was also a cold signal evident around 2000-dbar in the midst of the warm months. These two features may be the result of noise in the 2-year time series that was constructed from scattered Deep Argo profiles.

Seasonal cycles observed by Deep Argo were consistent with expected changes due to seasonal heaving of the deep-ocean. Upward motion of the water column would raise isotherms (causing cooling on pressure surfaces) and shift the deep-ocean salinity maximum up (causing salinification at shallower pressures and freshening at deeper pressures). Downward motion of the water column would have the opposite effect (warming on pressure surfaces, freshening at shallower pressures, salinification at deeper pressures). Decomposing the  $\theta$  seasonal cycle into heave and spice components (equation 3.4) confirmed the dominance of heave, with seasonal changes due to heave extremely similar to the total seasonal cycle ( $R^2 = 0.89$ ; Figures 3.8c–e). The residual (and therefore error) of the decomposition was small ( $\text{RMSE} = 0.003^{\circ}\text{C}$ ;  $R^2 = 0.99$ ). Applying this heave/spice decomposition to salinity produced the same conclusion.

Changes due to heave are often wind-driven (e.g. Bindoff and McDougall 1994; Köhl 2014; Sun et al. 2022), and it has been hypothesised that deep-ocean seasonality in the SWPB interior is driven by Ekman pumping (Zilberman et al. 2020). However, the local Ekman pumping seasonal cycle over the DWBC changes sign between the subtropics and midlatitudes (not shown). This transition occurs between roughly  $31\text{--}36^{\circ}\text{S}$  (within the southern half of the Kermadec Trench). The Deep Argo profiles we used to determine the seasonal cycle in the Kermadec Trench DWBC (Figure 3.8) spanned the entire length of the Kermadec Trench, including this transition region, which complicated the evaluation of Ekman pumping as a possible forcing mechanism. Using Deep Argo profiles to examine a smaller latitude range within the Kermadec Trench DWBC that excluded the transition region was not feasible (but should become possible with sustained Deep Argo observations). Incorporating Deep Argo

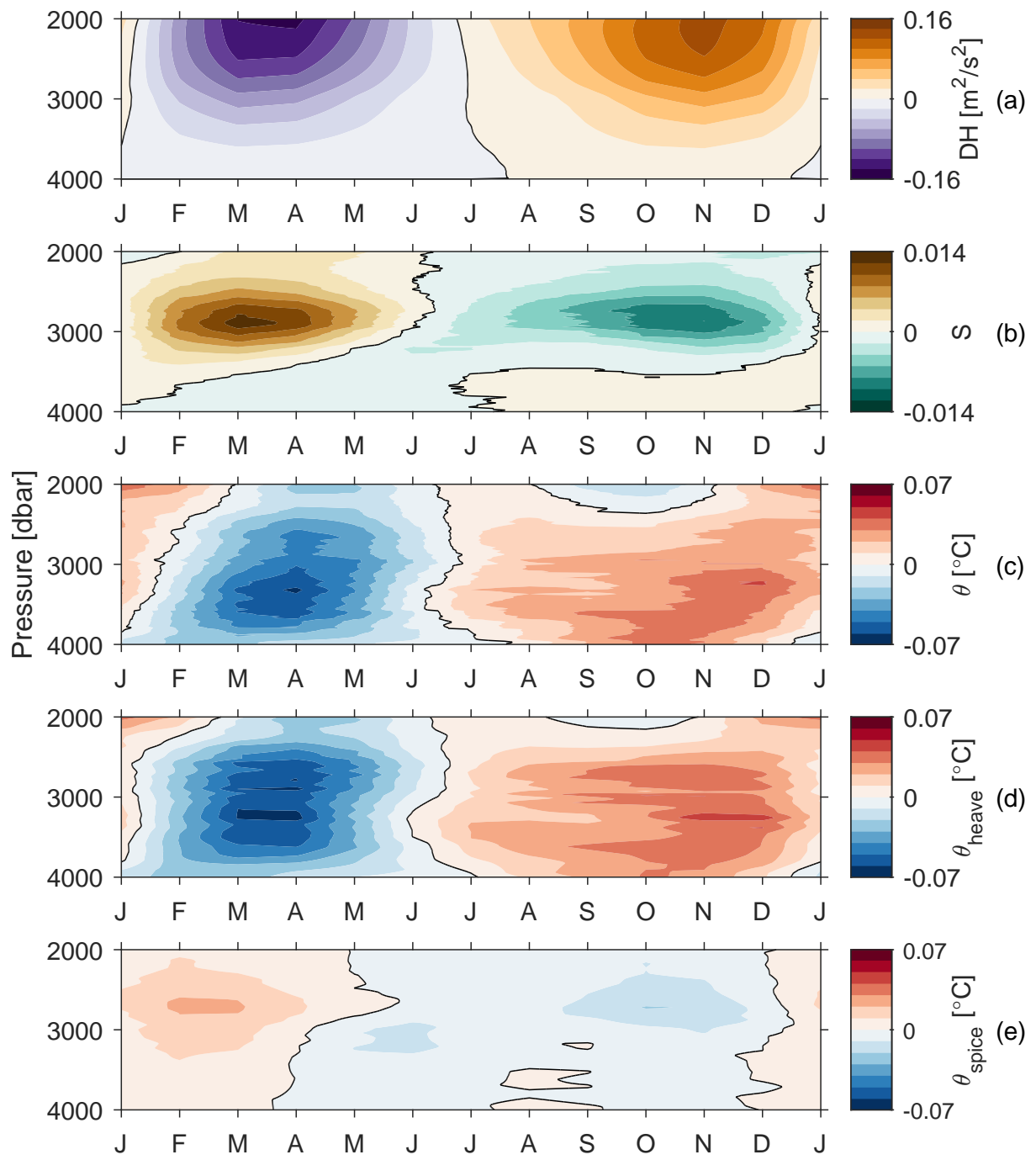


**Figure 3.8.** Seasonal cycles between 2000–4000-dbar from Deep Argo profiles in the Kermadec Trench DWBC (26–38°S) for (a) dynamic height relative to 4000-dbar ( $DH$ ), (b) salinity ( $S$ ), (c) potential temperature ( $\theta$ ), and potential temperature decomposed into (d) heave ( $\theta_{\text{heave}}$ ) and (e) spice ( $\theta_{\text{spice}}$ ) components. Black line is the 0 contour.

profiles from the DWBC north of the Kermadec Trench would introduce profiles with different  $\theta$ -salinity characteristics that could additionally confound results. We therefore used the GLORYS eddy-resolving ocean reanalysis to examine deep-ocean seasonality within the Kermadec Trench DWBC for each of these distinct Ekman pumping regions.

To first validate GLORYS, seasonal cycles of DH, salinity, and  $\theta$  (over the full 1993–2020 time series) were computed from GLORYS profiles interpolated to the locations of the Deep Argo profiles spanning the full length of the Kermadec Trench DWBC (i.e. the same Deep Argo profiles used for Figure 3.8). GLORYS DH (Figure 3.9a) demonstrated steric contraction between December–May and steric expansion between June–December, a difference of 1-month compared to Deep Argo observations. The largest salinity signals in GLORYS (Figure 3.9b) were observed around 2000-m, a feature not evident in the Deep Argo seasonal cycle. However, at 2866-m (a similar depth-level to the largest Deep Argo salinity signals) the saltiest signal occurred in March, at the same time as Deep Argo, and the freshest signal occurred in August, 3-months earlier than Deep Argo. GLORYS  $\theta$  (Figure 3.9c) changed sign earlier at shallower depths but, broadly speaking, was colder between December–May and warmer between May–November, a phase difference of 1–2-months compared to Deep Argo. This earlier change in sign at shallower depths was likely due to the different seasonal regimes in the northern and southern Kermadec Trench, and largely disappeared when only the northern Kermadec Trench DWBC was considered. Seasonal changes in deep-ocean  $\theta$  were predominantly due to heave ( $R^2 = 0.92$ ; Figures 3.9c–e), as was also found in Deep Argo observations. For all three variables, GLORYS seasonal cycles (Figure 3.9) were weaker than those observed by Deep Argo (Figure 3.8). Differences between GLORYS and Deep Argo may be related to the short Deep Argo time series, the uneven and changing distribution of Deep Argo profiles, the different Deep Argo and GLORYS time periods, GLORYS misrepresenting the true seasonal cycle, and/or GLORYS underestimating variability in the deep-ocean. Nevertheless, GLORYS provided a reasonable representation of the observed seasonal cycle phase (Figure 3.9a) and forcing mechanism (heave) in the Kermadec Trench DWBC. Hence, GLORYS was used to further explore deep-ocean

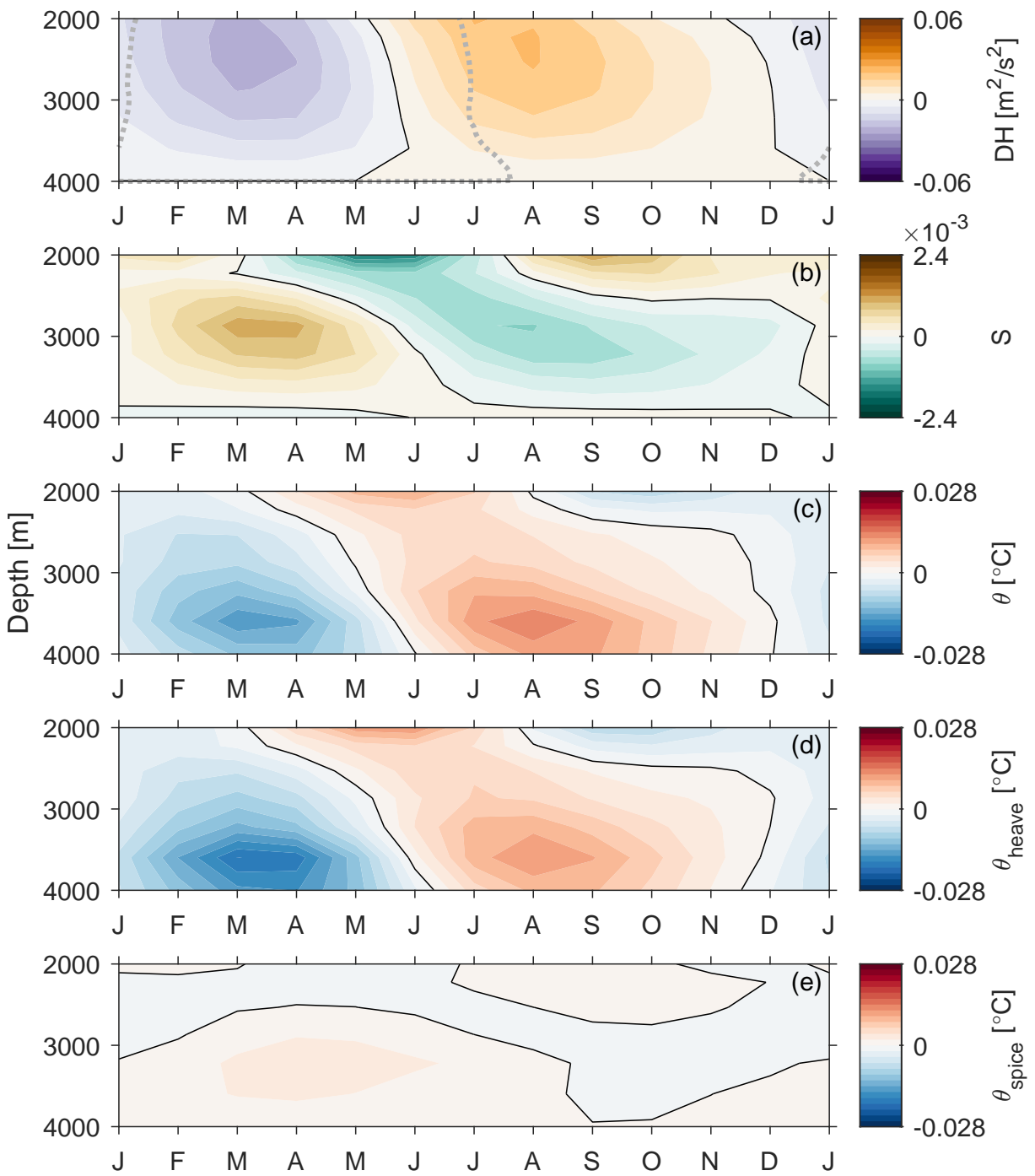


**Figure 3.9.** Seasonal cycles between 2000–4000-m computed from GLORYS (1993–2020) interpolated to the locations of Deep Argo profiles in the Kermadec Trench DWBC (26–38°S) for (a) dynamic height relative to 3992-m (DH), (b) salinity (S), (c) potential temperature ( $\theta$ ), and potential temperature decomposed into (d) heave ( $\theta_{\text{heave}}$ ) and (e) spice ( $\theta_{\text{spice}}$ ) components. Black line is the 0 contour. Grey dashed line in (a) is the 0 contour for the 2021–2022 Deep Argo DH seasonal cycle in the Kermadec Trench DWBC (see Figure 3.8, but note the different colour scale).

seasonality in the northern ( $26\text{--}30^{\circ}\text{S}$ ) and southern ( $32\text{--}36^{\circ}\text{S}$ ) Kermadec Trench regions that each experienced different Ekman pumping seasonal cycles.

ERA5 Ekman pumping and GLORYS DH, salinity, and  $\theta$  seasonal cycles were computed over 1993–2020 for the DWBC in northern (Ekman pumping and DH shown in Figure 3.10;  $\theta$  and salinity not shown) and southern (not shown) Kermadec Trench regions. The southern Kermadec Trench demonstrated no clear seasonal cycles, as expected given the transitional nature of the Ekman pumping seasonal cycle in this region, and was therefore not investigated further. In the northern Kermadec Trench, the Ekman pumping seasonal cycle (Figure 3.10a) was positive (i.e. upward) in December–April and negative (i.e. downward) in May–November. DH seasonal changes (steric contraction in December–May, steric expansion in June–November; Figure 3.10b) were largely consistent with expected changes if Ekman pumping was driving seasonal heaving of the deep-ocean. To confirm this relationship between local Ekman pumping and deep-ocean DH, a coherence analysis (utilising 6-year segments with a Hanning window applied and 50% overlap) was conducted between the monthly time series of detrended Ekman pumping and DH anomalies over 1993–2020 (Figure A3.3). The EOF first-mode principal component was used as a single representative DH time series (accounting for 98% of variance in the 1993–2020 monthly time series of detrended DH anomalies between 2000–4000-m). For simplicity in interpreting phase, the sign of the principal component was reversed. A statistically significant coherence of 0.83 (exceeding the 95% significance threshold) was found at the annual frequency (Figure 3.10c). Coherence was not statistically significant at most other frequencies. The phase (Figure 3.10d) at the annual frequency ( $-25\pm21^{\circ}$ ) indicated that Ekman pumping anomalies led DH anomalies by less than a month. A similar relationship was evident at almost every GLORYS depth level between the surface and 4000-m (Figure A3.4), with coherence between detrended Ekman pumping and DH monthly anomalies over 1993–2020 statistically significant at the annual period for all depths. Phase at the annual period was constant with depth (within uncertainties), except in the near-surface, and indicated that Ekman pumping anomalies led DH anomalies by less than a month.

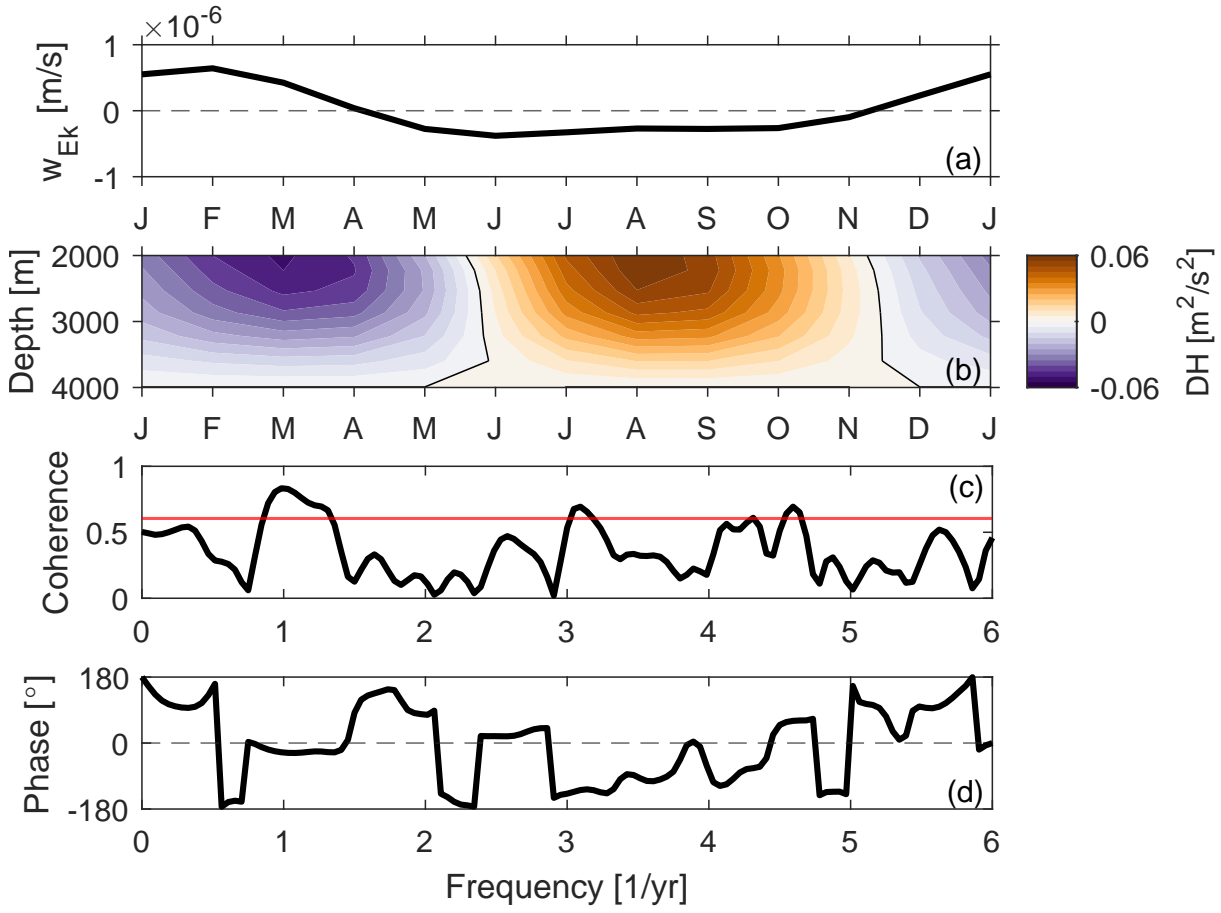


**Figure 3.10.** Seasonal cycles in the northern Kermadec Trench DWBC (26–30°S) for (a) Ekman pumping ( $w_{Ek}$ ) computed from ERA5 and (b) dynamic height relative to 3992-m (DH) computed from GLORYS (same colour scale as Figure 3.9a). (c) Coherence and (d) phase between 1993–2020 monthly anomalies of  $w_{Ek}$  and the DH first-mode principal component. Red line is the 95% significance threshold. A negative phase means  $w_{Ek}$  leads DH.

## 3.6 Discussion

The DWBC pathway identified from Deep Argo float trajectories between 5–40°S over the time period 2016–2022 broadly agrees with, and thus validates, the general pathway previously identified using historical hydrographic observations (Reid 1986, 1997). However, float trajectories resolved the DWBC pathway in much finer detail than was possible using historical observations. The apparent eddying behaviour within the Osbourn Trough does not seem to have been previously identified or characterised, although earlier maps show rather tortuous

deep flow pathways at a similar latitude (Reid 1986, 1997). A hydrographic section along 22°S (intersecting the Osbourn Trough) in 1969 suggested DWBC flow was concentrated alongside the Tonga-Kermadec Ridge and between 168–165°W (i.e. east of the Deep Argo trajectories in the Osbourn Trough; Warren and Voorhis 1970). The majority of northward transport across this hydrographic section occurred in the eastern region, although average velocities at 4200-m were weak ( $0.010\text{--}0.017\text{ ms}^{-1}$ ; Warren and Voorhis 1970). These earlier velocities were similar to the average Deep Argo trajectory velocity above 5500-dbar in the Osbourn Trough ( $0.007\pm0.013\text{ ms}^{-1}$ , the large uncertainty reflects the large velocity variability). In the low-latitude South Atlantic, the southward-flowing DWBC breaks up into a series of deep anticyclonic eddies around 8°S, with these eddies responsible for all of the DWBC transport across 11°S (Dengler et al. 2004; Schott et al. 2005). We wonder if the situation is similar here, with eddies contributing to DWBC transport across the Osbourn Trough. If so, it may be that the eastern region of DWBC flow measured by Warren and Voorhis (1970) was the northward velocity of an eddy or series of eddies. An examination of DWBC (and eddy) transport is beyond the scope of this study, with the Deep Argo pilot array not yet robust enough to undertake such work, but we note that 1993–2020 time-mean GLORYS velocities at 5275-m depth also demonstrated what appeared to be an eddy field within the Osbourn Trough. The breakdown of the southward-flowing South Atlantic DWBC into a series of eddies is caused by upstream instabilities (Dengler et al. 2004), likely barotropic instabilities (Brum et al. 2023). If a similar mechanism is operating in the SWPB, the abrupt change in bathymetry at the Louisville Seamount Chain collision zone could be a possible source of instabilities. Alternatively, the breakdown of coherent DWBC flow may be induced by the deeper and more uniform depth of the Osbourn Trough (typically 5500–6000-m deep) removing topographic steering constraints.

Deep Argo trajectories also confirmed the occurrence of a cyclonic circulation, consisting of equatorward-flowing DWBC and poleward-flowing recirculation, over the entire Kermadec Trench. The recirculation had previously been inferred based on limited hydrographic and mooring observations (Johnson 1998). In the early 1990s, three current meters on two moorings

at  $32.5^{\circ}\text{S}$  measured poleward velocities within the Kermadec Trench below 3000-dbar ( $-0.020 \text{ ms}^{-1}$  at 3970-m,  $-0.015 \text{ ms}^{-1}$  at 5800-m,  $-0.010 \text{ ms}^{-1}$  at 5915-m; Whitworth III et al. 1999). Deep Argo trajectory velocities along the eastern side of the Kermadec Trench measured a poleward recirculation with similar magnitude ( $-0.021 \pm 0.008 \text{ ms}^{-1}$ ). The similarity between these independent data sets from different time periods and with different spatial coverage indicates that the tight cyclonic circulation over the Kermadec Trench is a robust feature. Johnson (1998) postulated that cyclonic circulations are common to all deep-ocean trenches with closed  $\frac{f}{H}$  contours. A global Deep Argo array could potentially enable determination of whether these cyclonic circulations are indeed a ubiquitous feature of deep-ocean trenches, although such an array has been recommended to use a 1000-dbar parking pressure consistent with Core Argo (Zilberman et al. 2023c) and may therefore not provide deep-ocean trajectories.

Estimates of vertical turbulent diffusivity in the Samoan Passage from a numerical model ( $6.2 \times 10^{-3} \text{ m}^2 \text{ s}^{-1}$ ) and from conservation of  $\theta$  ( $1.57 \times 10^{-2} \text{ m}^2 \text{ s}^{-1}$ ) and salinity ( $6.1 \times 10^{-3} \text{ m}^2 \text{ s}^{-1}$ ) using direct observations were consistent with prior estimates of vertical turbulent diffusivity in the Samoan Passage ( $3 \times 10^{-3}$  to  $5 \times 10^{-2} \text{ m}^2 \text{ s}^{-1}$ ; Roemmich et al. 1996; Voet et al. 2015). Deep Argo was therefore able to accurately estimate vertical turbulent diffusivity through the Samoan Passage, a known site of enhanced deep-ocean mixing (Alford et al. 2013; Roemmich et al. 1996; Voet et al. 2015). We expect that Deep Argo observations and this model could be similarly used to evaluate vertical turbulent diffusivity at other sites of enhanced deep-ocean mixing.

Large changes in  $\theta$  and salinity properties were also observed at the Louisville Seamount Chain collision zone, with the NADW salinity maximum not present north of the collision zone. The Louisville Seamount Chain collision zone had not previously been identified as a site of enhanced deep-ocean mixing, and erosion of the remnant NADW salinity maximum at the collision zone would seem to answer the question posed by Whitworth III et al. (1999) of how this salinity maximum disappears between  $32.5^{\circ}\text{S}$  and the Samoan Passage. However, the modelled evolution of  $\theta$  and salinity profiles due to vertical turbulent diffusivity within the collision zone

was not consistent with the mean profiles observed downstream of the collision zone. As such, the observed change in water mass properties cannot be solely due to vertical turbulent diffusivity. Additional processes, such as horizontal turbulent diffusivity (along isopycnals), must also be important. It is difficult to confidently determine these processes as only two of the Deep Argo floats used in this study had passed through the collision zone.

A global Deep Argo array could reveal other regions of enhanced deep-ocean mixing and thus contribute to improving the representation and distribution of deep-ocean turbulence in climate models. Indeed, Johnson et al. (2022) used Deep Argo descent rates to show that, below 1000-m, internal wave activity tended to be higher around regions of rougher topography than over the abyssal plains. It is therefore recommended that the vertical resolution of Deep Argo measurements be increased to allow deep-ocean turbulence to be estimated via vertical strain (e.g. Johnson et al. 2022). Efforts are also being made to include microstructure turbulence sensors on Argo floats, including Deep Argo, though this work is yet to be implemented (Roemmich et al. 2019a).

Seasonal cycles of  $\theta$ , salinity, and DH between 2000–4000-dbar were observed by Deep Argo floats in the DWBC along the Kermadec Trench. These seasonal cycles were predominantly due to seasonal heaving of the deep-ocean. Upward heaving raised isotherms (causing cooling on pressure surfaces) and shifted the deep-ocean salinity maximum shallower (causing salinification at shallower pressures and freshening at deeper pressures), with the net result being steric contraction. Downward heaving had the opposite effect. For the DWBC in the northern Kermadec Trench (26–30°S), local Ekman pumping anomalies at the surface and GLORYS DH anomalies in the deep-ocean exhibited a statistically significant coherence and were essentially in-phase at the annual period, with downward Ekman pumping anomalies coincident with deep-ocean steric expansion and upward Ekman pumping anomalies coincident with deep-ocean steric contraction. Furthermore, the seasonal steric expansion and contraction, significant coherence, and in-phase relationship were evident throughout the water column (below the seasonal surface mixed layer and above 4000-m), as would be expected if local Ekman pumping

was driving seasonal heaving. Local Ekman pumping at the surface therefore appears to be the dominant forcing mechanism of the deep-ocean seasonal cycle in the northern Kermadec Trench. However, this relationship may not hold everywhere along the DWBC. For example, the subtropical (15–32°S) deep-ocean seasonal cycle in the interior of the SWPB (Zilberman et al. 2020) lags local Ekman pumping at the western boundary by 3-months. Continued Deep Argo measurements at the western boundary of the SWPB will enable determination of the deep-ocean seasonal cycle elsewhere along this DWBC.

Other forcing mechanisms seem less likely to be driving the deep-ocean seasonal cycle in the northern Kermadec Trench. Seasonal changes in the production or characteristics of deep-ocean water masses would have to propagate from their high-latitude source regions, and thus changes should be evident in both the southern and northern Kermadec Trench. However, no southern Kermadec Trench deep-ocean seasonal signal was found at the 32.5°S mooring array (Whitworth III et al. 1999), albeit from only a 22-month record, or in the longer 1993–2020 GLORYS output analysed here. Moore and Wilkin (1998) also discounted deep-water formation processes as a dominant source of variability in this DWBC on seasonal or shorter time scales. Rather, changes at the source regions where these deep-waters are formed tend to drive variability on decadal or longer time scales (Bindoff and McDougall 1994; Masuda et al. 2010). For example, a reduction in formation of the densest bottom waters over recent decades has caused a downward heave of deep-ocean isotherms (Johnson 2022; Purkey and Johnson 2012; Purkey et al. 2019). Propagating features, such as topographic Rossby waves, are another possible forcing mechanism. However, topographic Rossby waves at the western boundary of the SWPB would also travel through the southern Kermadec Trench where no seasonal signal was evident. Instead, topographic Rossby waves are believed to be the dominant source of intra-annual variability in this DWBC at 32.5°S (Moore and Wilkin 1998; Whitworth III et al. 1999), and in other Southern Hemisphere DWBCs (Fukamachi et al. 2010; Valla et al. 2019).

If we assume there is a consistent Ekman pumping-driven seasonal heaving across the SWPB at the latitude of the northern Kermadec Trench, then a simple potential vorticity

or Sverdrup balance argument suggests corresponding seasonal changes in DWBC transport. Vertically integrating the Sverdrup relation through the water column gives the equation for Sverdrup transport:

$$\beta V = f w_{Ek} \quad (3.5)$$

where  $\beta$  is the Rossby parameter ( $\frac{\partial f}{\partial y}$ ) and  $V$  is vertically-integrated meridional transport (e.g. Cushman-Roisin and Beckers 2011). This equation suggests that anomalously positive Ekman pumping enhances poleward transport in the interior. To balance this enhanced poleward interior flow, there must be enhanced equatorward transport at the western boundary. The situation reverses for anomalously negative Ekman pumping (i.e. reduced equatorward transport at the western boundary). Indeed, GLORYS meridional velocities at approximately 3220-m (within the depth range of the observed deep-ocean heaving) demonstrated a velocity seasonal cycle in the northern Kermadec Trench (Figure A3.5). DWBC velocities over almost the entire western flank of the northern Kermadec Trench region were significantly stronger in March (northward velocity seasonal maximum) than August (northward velocity seasonal minimum), as the Sverdrup relation argument suggests. However, recirculation velocities on the eastern side of the trench were also stronger in March than August, although only statistically significant over a substantially smaller area. It therefore remains to be seen whether seasonal changes are evident in net DWBC transport. Additionally, this brief examination comes with the caveat that temporal variability in GLORYS deep-ocean velocity has not yet been validated against observations in the Kermadec Trench.

Observing a transport seasonal cycle may be difficult without a long-term time series. The substantial transport variability in this DWBC on shorter time scales (Whitworth III et al. 1999) is likely larger than the seasonal transport signal, similar to that observed in other DWBCs (e.g. Lee et al. 1996; Meinen et al. 2017; Schott et al. 2005). For an Ekman pumping seasonal amplitude of  $6.4 \times 10^{-7} \text{ ms}^{-1}$  (the maximum Ekman pumping seasonal signal for the northern Kermadec Trench) and horizontal distance of 6000-km (a rough approximation of the SWPB

width at 28°S), the interior Sverdrup transport (equation 3.5) is  $-13$  Sv. If half of this transport occurs below 2000-m (barotropic flow in a 4000-m deep basin), the resulting DWBC transport seasonal signal of 6.5 Sv is clearly overwhelmed by the 1991–1992 DWBC transport standard deviation (11.9 Sv) and range (68.2 Sv) observed below 2000-m at 32.5°S (Whitworth III et al. 1999).

To the best of our knowledge, this work represents the first time an eddy-resolving ocean reanalysis has been compared against Deep Argo observations in the SWPB. Generally speaking, GLORYS qualitatively reproduced the observed DWBC and recirculation over the Kermadec Trench, although with a bias in velocity magnitude that changed with latitude. GLORYS had previously been found to broadly reproduce deep-ocean velocity in the Philippine Trench (Song et al. 2023) and in the Antarctic Circumpolar Current (Artana et al. 2021). When comparing  $\theta$ -salinity properties, GLORYS underestimated the deep-ocean salinity maximum and the very coarse vertical resolution of GLORYS in the deep-ocean meant that none of the discrete depth levels were within the core of the observed salinity maximum. GLORYS also had saltier and colder bottom waters than observed by Deep Argo, although this difference could reflect the different time periods. Using Deep Argo profiles in the SWPB, Johnson et al. (2019) observed a mean warming rate below 5000-dbar of  $3 \times 10^{-3}$ °C/year. Dividing the difference in GLORYS and Deep Argo  $\theta$  averaged below 5000-m by this warming rate gives a time scale (12.7-years) that is similar to the time difference between the mean GLORYS and Deep Argo dates (14.8-years). Seasonal cycles observed by Deep Argo were broadly reproduced by GLORYS, with changes predominantly due to heaving in both, but the magnitude of the seasonal signal was much weaker in the reanalysis. Even with these discrepancies, the similarities between Deep Argo observations and GLORYS output in the Kermadec Trench are remarkable given the limited amount of data presently assimilated below 2000-m. Assimilation of Deep Argo observations into future ocean reanalyses will improve the representation of the deep-ocean, potentially halving deep-ocean temperature and salinity errors (Gasparin et al. 2020). However, until this assimilation occurs, Deep Argo observations provide a means of validating the representation of

the deep-ocean in ocean reanalyses and models.

In summary, we have presented new insights into the DWBC of the SWPB using an unprecedented number of deep-ocean observations alongside output from an eddy-resolving ocean reanalysis. The spatial coverage provided by Deep Argo floats has clarified the pathway of this DWBC, including recirculation over the Kermadec Trench and seemingly as an eddy field within the Osbourn Trough. Using changes in  $\theta$  and salinity along the length of the DWBC we were able to resolve vertical turbulent mixing in the Samoan Passage, and revealed the Louisville Seamount Chain collision zone as a previously unidentified region of enhanced deep-ocean mixing where multiple mixing processes appear to be important. Seasonal heaving of isopycnals was evident in the DWBC and, in the northern Kermadec Trench, was found to be driven by local winds. However, this work only examined one Southern Hemisphere DWBC. We hypothesise that enhanced deep-ocean mixing at bathymetric choke-points and wind-driven seasonal heaving will also be present in other DWBCs. Even so, limited DWBC observations mean these characteristics may not be identifiable until a global deep-ocean observing system, such as a mature Deep Argo array, is achieved.

### 3.7 Open Research

Argo data is collected and made available by the International Argo Program and the national programs that contribute to it (Argo 2024). The Scripps Argo Trajectory-Based Velocity Product is available from the UC San Diego Library at <https://doi.org/10.6075/J0NK3F7V> (Zilberman et al. 2023b). GLORYS data is available from the EU Copernicus Marine Service at <https://doi.org/10.48670/moi-00021> (CMEMS 2018). ERA5 data is available from the Copernicus Climate Change Service at <https://doi.org/10.24381/cds.f17050d7> (Hersbach et al. 2023). WOCE current meter data was downloaded from NOAA National Centers for Environmental Information (<https://www.nodc.noaa.gov/archive/arc0001/0000649/1.1/data/0-data/disk2/cmdac/explist.htm>). Bathymetry data was from the ETOPO1 dataset which is made available by NOAA

National Centers for Environmental Information at <https://doi.org/10.7289/V5C8276M> (NOAA 2009). Colourmaps are from BrewerMap (<https://github.com/DrosteEffect/BrewerMap>). This work utilised the Gibbs-SeaWater Oceanographic Toolbox (McDougall and Barker 2011). The Deep Argo profiles and trajectories used in this study have been made permanently and publicly available at <https://doi.org/10.5281/zenodo.10791519> (Chandler 2024a). Monthly time series and seasonal cycles of potential temperature, salinity, and dynamic height from the spatially-averaged Deep Argo profiles within the Kermadec Trench DWBC have also been made permanently and publicly available at <https://doi.org/10.5281/zenodo.10791519> (Chandler 2024a).

### **3.8 Acknowledgements**

We would like to acknowledge Phil Sutton, Denise Fernandez, Matt Walkington and the crews of the R/V Kaharoa and R/V Tangaroa for their work in deploying the Deep Argo floats used in this study, John Gilson for conducting the delayed-mode quality control of these Deep Argo floats, Megan Scanderbeg for maintaining the Scripps Argo Trajectory-Based Velocity Product, and Gunnar Voet for providing the code for the numerical model. We also thank two anonymous reviewers for their time and feedback. MC and NZ received support from NOPP (NOAA grant NA18OAR0110434). MC, NZ, and JS received support from the NOAA Global Ocean Monitoring and Observing Program through Award NA20OAR4320278. NZ received support from NSF (OCE-2242742).

This chapter, in full, is a reprint of the material as it appears in ‘Chandler, M., Zilberman, N. V., and Sprintall, J. (2024). The deep western boundary current of the Southwest Pacific Basin: Insights from Deep Argo. *Journal of Geophysical Research: Oceans*, 129, e2024JC021098, <https://doi.org/10.1029/2024JC021098>’. The dissertation author was the primary investigator and author of this paper.

### 3.A Supplementary Figures for Chapter 3

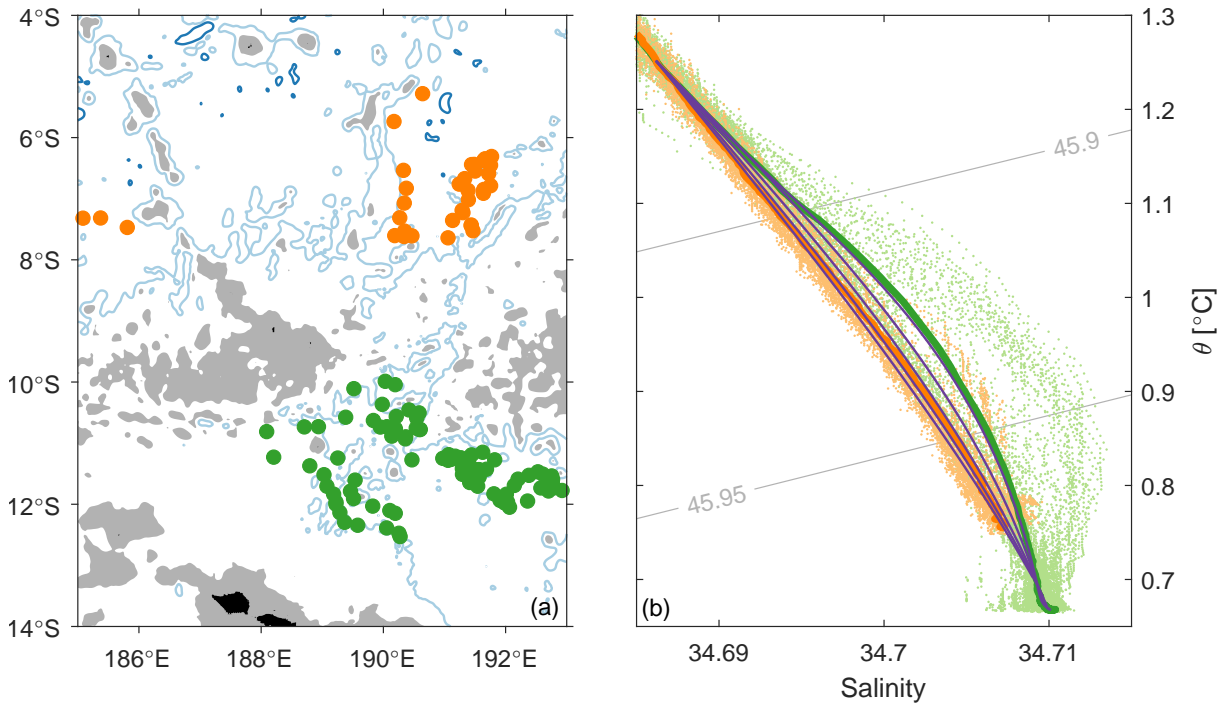


**Figure A3.1.** (a) Locations of Deep Argo profiles immediately upstream (green) and downstream (orange) of the Samoan Passage. Bathymetry contours are 5000-m (light blue) and 6000-m (dark blue), grey shading is shallower than 4000-m. Profiles within the passage are not shown. (b) Potential temperature ( $\theta$ ) - salinity curves for profiles upstream (mean profile in green, individual profiles in light green) and downstream (mean profile in orange, individual profiles in light orange) of the Samoan Passage, with  $\sigma_4$  (potential density anomaly referenced to 4000-dbar;  $\text{kg m}^{-3}$ ) contours in grey. Purple curves are the solutions of the numerical model applied to the mean upstream profile for spreading scales  $\lambda = 100\text{-m}, 200\text{-m}, 300\text{-m}, 400\text{-m}, \text{ and } 500\text{-m}$  (right-to-left).

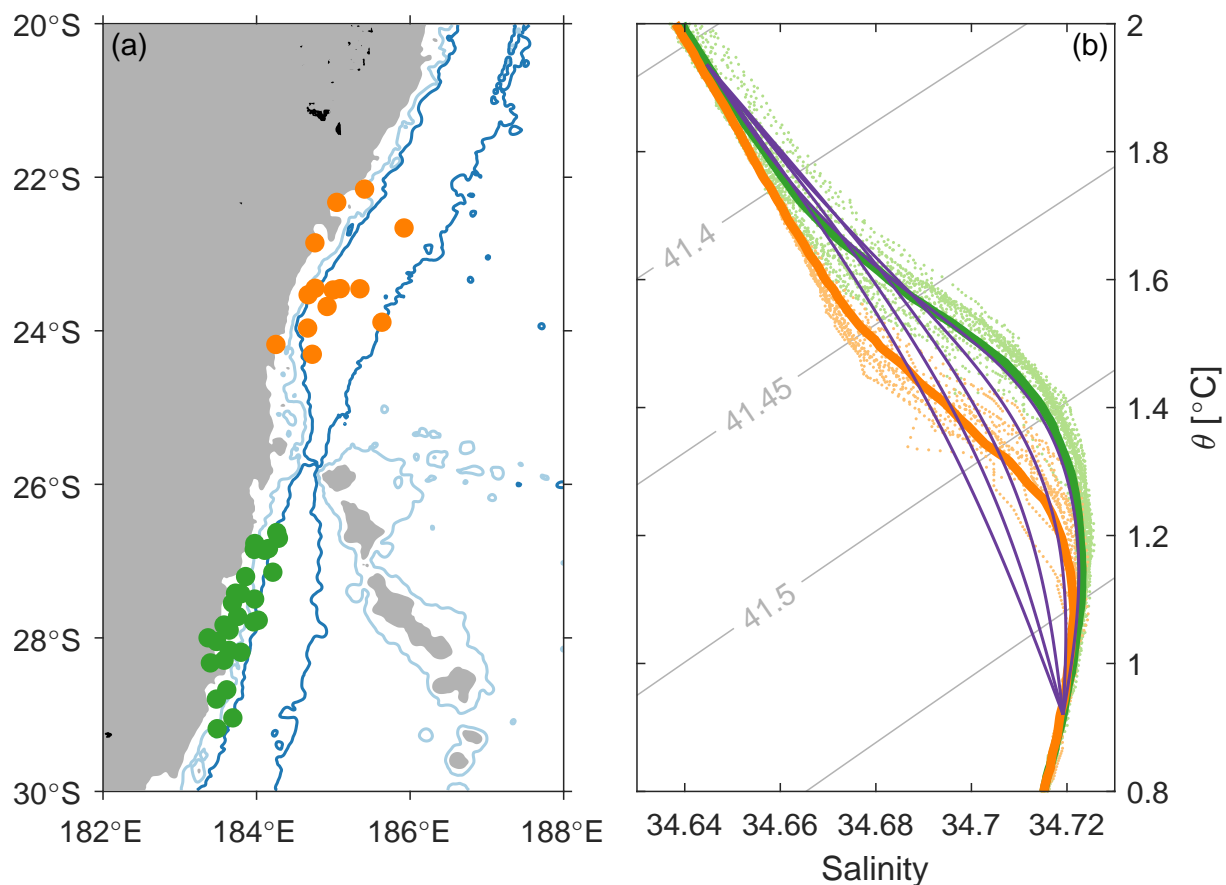


**Figure A3.2.** (a) Locations of Deep Argo profiles immediately upstream (green) and downstream (orange) of the Louisville Seamount Chain collision zone. Bathymetry contours are 5000-m (light blue) and 6000-m (dark blue), grey shading is shallower than 4000-m. Profiles within the collision zone are not shown. (b) Potential temperature ( $\theta$ ) - salinity curves for profiles upstream (mean profile in green, individual profiles in light green) and downstream (mean profile in orange, individual profiles in light orange) of the Louisville Seamount Chain collision zone, with  $\sigma_3$  (potential density anomaly referenced to 3000-dbar;  $\text{kg m}^{-3}$ ) contours in grey. Purple curves are the solutions of the numerical model applied to the mean upstream profile for spreading scales  $\lambda = 100\text{-}500\text{ m}$ , 200-m, 300-m, 400-m, and 500-m (right-to-left).

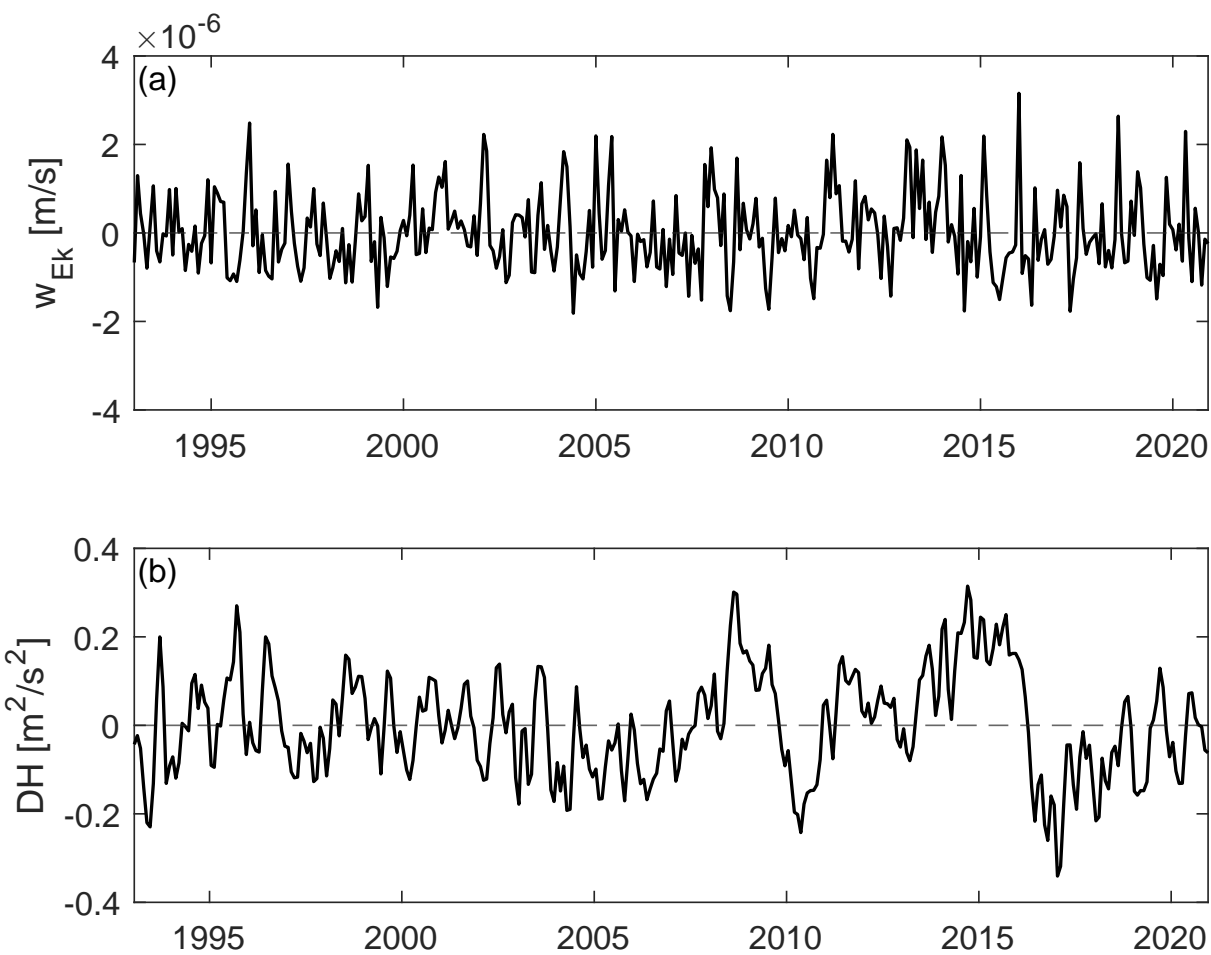


**Figure A3.3.** Detrended 1993–2020 monthly anomalies of (a) Ekman pumping ( $w_{Ek}$ ) from ERA5 and (b) the first principal component of dynamic height between 2000–4000-m (DH) from GLORYS, both in the northern Kermadec Trench DWBC (26–30°S).

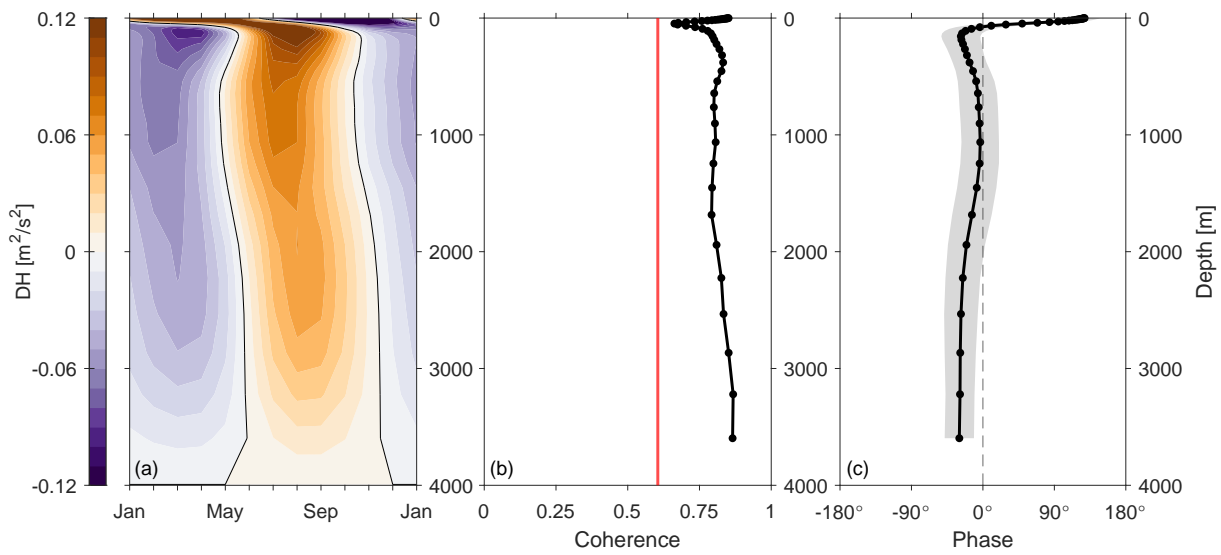


**Figure A3.4.** (a) Seasonal cycle of GLORYS dynamic height relative to 3992-m (DH) in the northern Kermadec Trench DWBC (26–30°S). (b) Coherence and (c) phase at the annual period between 1993–2020 monthly anomalies of detrended local Ekman pumping (from ERA5) and detrended DH (from GLORYS) in the northern Kermadec Trench DWBC. Dots indicate GLORYS discrete depth levels. The red line in (b) is the 95% significance threshold. Shading in (c) is the 95% confidence interval. A negative phase means that Ekman pumping leads DH. The change in phase near the surface likely reflects the influence of surface heating in summer (causing steric expansion) and cooling in winter (causing steric contraction). The coherence analysis utilised 6-year segments with a Hanning window applied and 50% overlap.

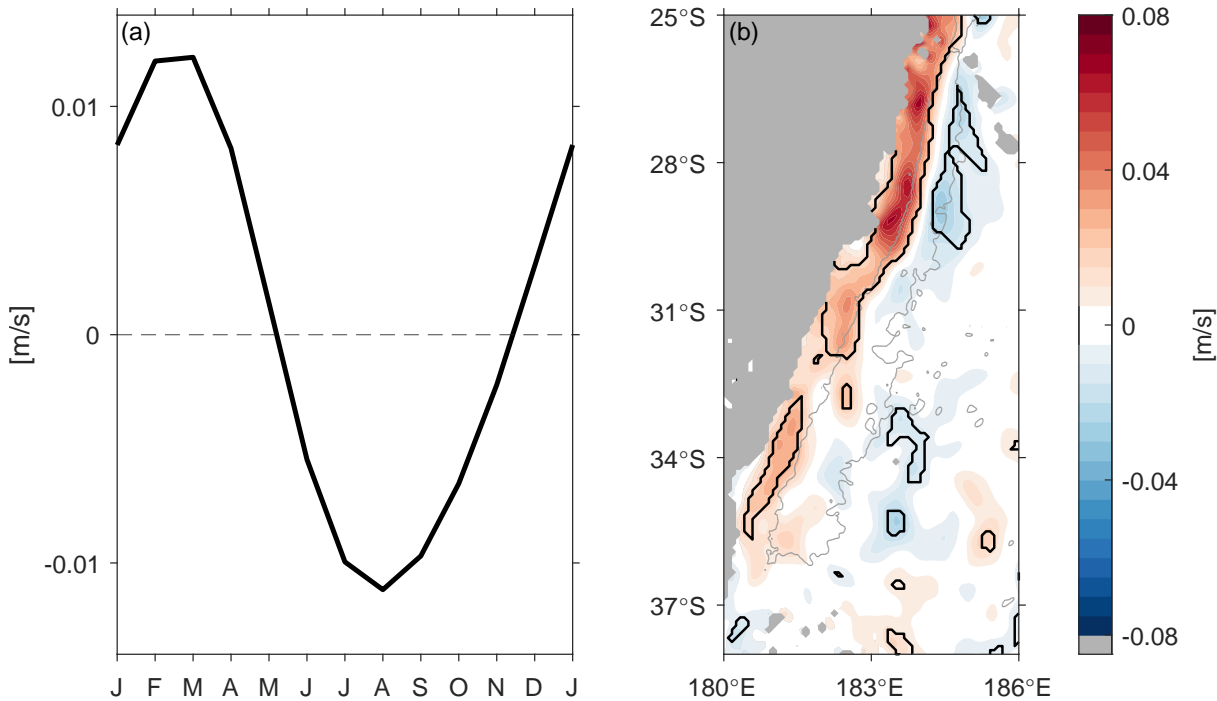


**Figure A3.5.** (a) Seasonal cycle of GLORYS northward meridional velocity at 3221-m depth in the northern Kermadec Trench DWBC (26–30°S) over 1993–2020. Positive is northward. (b) Mean difference in GLORYS meridional velocity between March and August at 3221-m depth in the Kermadec Trench and surrounding area (August subtracted from March). Black contour identifies where the difference is statistically significant from  $0 \text{ ms}^{-1}$  ( $p < 0.05$  using a two-tailed t-test with each year considered independent). The 6000-m bathymetry contour is in light grey, bathymetry shallower than 4000-m is shaded.

# Chapter 4

## Conclusions

The work in this dissertation has enhanced our knowledge of western boundary current (WBC) variability in both the upper-ocean (shallower than 2000-m) and deep-ocean (deeper than 2000-m) through the use of globally available ocean observations including High-Resolution eXpendable BathyThermographs (HR-XBTs), Argo floats, and satellites.

In Chapter 1 (Chandler et al. 2022a), I examined transport trends and variability in the subtropical WBCs of the Pacific and Indian Oceans. Estimates of cross-transect geostrophic velocity between the surface and 1975-m deep were constructed by combining complementary ocean observations along HR-XBT transects intersecting the Agulhas Current, East Australian Current (EAC), and Kuroshio. The resulting 16-year time series are longer than most other subsurface observations in these WBCs. As such, I was able to detect a weakening trend in Kuroshio transport. This decline in Kuroshio transport is believed to be driven by a weakening of the wind stress curl over the subtropical North Pacific Ocean which has caused both a decrease in speed and a narrowing of the current. There were no significant changes in Agulhas Current transport or EAC transport. Additionally, all three WBCs demonstrated similar and significant transport seasonal cycles, with stronger transport in the summer (weaker in the winter). This stronger WBC transport in summer was due to an increase in current speed and may be driven by local winds.

In Chapter 2 (in prep), I examined subsurface marine heatwaves (MHWs) along a HR-

XBT transect intersecting the Kuroshio and Kuroshio Extension east of Japan. By combining complementary HR-XBT and satellite observations, I was able to construct a 30-year time series of synthetic temperature anomalies between the surface and 800-m deep. A significant Kuroshio warming trend, driven by heaving of isotherms, was detected throughout the water column and determined to be driving an increase in both surface and subsurface Kuroshio MHW days per year. Subsurface MHWs were also discovered to occur significantly more often during El Niño periods. This increased occurrence during El Niño was due to a strengthening of the Kuroshio Extension and its Southern Recirculation Gyre, and was evident under both Central Pacific and Eastern Pacific El Niño conditions. In contrast, MHW occurrence at the surface was not influenced by the El Niño-Southern Oscillation (ENSO). This difference in MHW occurrence between the surface and subsurface emphasises the need for subsurface observations to be included in MHW studies.

Lastly, in Chapter 3 (Chandler et al. 2024), I examined spatial and temporal variability in the deep western boundary current (DWBC) of the Southwest Pacific Basin using Deep Argo observations. Deep Argo trajectory velocities confirmed the existence of a tight cyclonic recirculation over the Kermadec Trench. While, in the northern Kermadec Trench, Deep Argo profiles and an ocean reanalysis revealed seasonal heaving within the DWBC that was likely driven by local Ekman pumping at the surface. A Sverdrup balance argument suggests that this wind-driven heaving could influence seasonal DWBC transport. The deep-ocean salinity maximum was eroded as the DWBC exited the Kermadec Trench to the north through the Louisville Seamount Chain collision zone, thereby illuminating the collision zone as a previously unidentified site of enhanced deep-ocean mixing. Mixing within the collision zone could not be due solely to vertical turbulent diffusivity. Nevertheless, Deep Argo observations were able to accurately estimate vertical turbulent diffusivity through the Samoan Passage, a known site of enhanced deep-ocean mixing, suggesting that Deep Argo could be used to evaluate vertical turbulent diffusivity at other sites of enhanced deep-ocean mixing.

## 4.1 Future Research Questions

The research in this dissertation covered four different WBCs (the EAC, Agulhas Current, Kuroshio, and Southwest Pacific Basin DWBC). However, because globally available observations were used, the methods implemented here could be applied in other WBCs. Furthermore, transect IX21 in the Indian Ocean intersects the East Madagascar Current (east of Madagascar) and transect PX30 in the Pacific Ocean intersects the Vauban Current (east of New Caledonia). The existing time series (Chandler et al. 2022a,b) could therefore be used to study these smaller WBCs.

The work in this dissertation has also spawned a number of additional research questions, three of which are highlighted below:

- In Chapter 1, I noted that the timing of the Kuroshio seasonal transport minimum differed between transect PX40 and further upstream around the East China Sea (e.g. Lee et al. 2001; Wei et al. 2015; Zhu et al. 2017). I hypothesised that this difference could be due to the Izu Ridge blocking westward-propagating barotropic Rossby waves. However, the Ryukyu Island Chain further to the west would also block westward-propagating features from reaching the East China Sea. It is therefore unclear which of these features, if either, is causing the different Kuroshio transport seasonal cycles in the two regions. A modelling approach, similar to that applied in the Agulhas Current by Hutchinson et al. (2018), could prove useful in addressing this question.
- In Chapter 3, I revealed that deep-ocean mixing at the Louisville Seamount Chain collision zone could not be due solely to vertical turbulent diffusivity. Additional processes, such as horizontal diffusivity (mixing along isopycnals), must therefore be important. However, I did not explore these processes further and the magnitude of this horizontal diffusivity remains unknown. Core Argo data has been used to estimate horizontal diffusivity in the upper-ocean (e.g. Cole et al. 2015; Roach et al. 2018; Sévellec et al. 2022) and it

seems plausible that, with enough observations, Deep Argo data could similarly be used to estimate horizontal diffusivity through the Louisville Seamount Chain collision zone.

- Also in Chapter 3, I identified that deep-ocean seasonal heaving in the northern Kermadec Trench was driven by local Ekman pumping at the surface. However, at the time of analysis, Deep Argo observations could not be used to explore this relationship elsewhere along the DWBC. Nevertheless, a cursory examination of output from an ocean reanalysis (GLORYS; Lellouche et al. 2021) suggests that deep-ocean dynamic height seasonal cycles are indeed present elsewhere along the DWBC. Curiously, between roughly the Louisville Seamount Chain collision zone and the Samoan Passage, these deep-ocean seasonal cycles may not be in-phase with local Ekman pumping. Is the timing of the deep-ocean seasonal cycle in the reanalysis, which was not validated outside the Kermadec Trench in this dissertation, incorrect here? Or are other forcing mechanisms, such as Rossby waves propagating westward from the basin interior, important at other locations along the DWBC?

## 4.2 Summary

In summary, the research presented in this dissertation has contributed to advancing our knowledge of WBC variability and its impacts. In the upper-ocean, the temperature and velocity time series are longer than most other subsurface measurements of the subtropical WBCs. Multiple cycles of important signals such as the seasonal cycle and ENSO cycle can therefore be resolved and thus the significance of long-term trends assessed. In the deep-ocean, Deep Argo observations along a DWBC revealed the existence of wind-driven seasonal heaving and unearthed a previously unidentified site of enhanced deep-ocean mixing. These results thus provide blueprints for exploring whether wind-driven seasonal heaving exists in other DWBCs (as one may expect), and for evaluating vertical turbulent diffusivity in the deep-ocean. Additionally, both the long-term WBC time series in the upper-ocean and new DWBC observations in the

deep-ocean can, and should, be used to validate model (and reanalysis) output. It is therefore clear that sustaining the global ocean observing system is critical for understanding the oceanic arteries and veins of our climate system – western boundary currents.

# Bibliography

- Alford, M. H., Girton, J. B., Voet, G., Carter, G. S., Mickett, J. B. and Klymak, J. M. (2013). Turbulent mixing and hydraulic control of abyssal water in the Samoan Passage. *Geophysical Research Letters* 40: 4668–4674, doi:10.1002/grl.50684.
- Ando, K., Lin, X., Villanoy, C., Danchenkov, M., Lee, J.-H., He, H.-J., Liu, Q., Liu, Y., Lobanov, V., Ma, X.-L., Mulyadi, H. A., Nagano, A., Ren, J.-L., Syahailatua, A., Tian, Y., Wu, L., Zhang, J., Zhang, L., Zhao, M., Zheng, J., Ma, S. and Zhu, W. (2021). Half-Century of Scientific Advancements Since the Cooperative Study of the Kuroshio and Adjacent Regions (CSK) Programme - Need for a new Kuroshio Research. *Progress in Oceanography* 193: 102513, doi:10.1016/j.pocean.2021.102513.
- Archer, M. R., Shay, L. K. and Johns, W. E. (2017). The Surface Velocity Structure of the Florida Current in a Jet Coordinate Frame. *Journal of Geophysical Research: Oceans* 122: 9189–9208, doi:10.1002/2017JC013286.
- Argo (2024). Argo float data and metadata from Global Data Assembly Centre (Argo GDAC) [Dataset]. doi:10.17882/42182.
- Artana, C., Ferrari, R., Bricaud, C., Lellouche, J.-M., Garric, G., Sennéchael, N., Lee, J.-H., Park, Y.-H. and Provost, C. (2021). Twenty-five years of Mercator ocean reanalysis GLORYS12 at Drake Passage: Velocity assessment and total volume transport. *Advances in Space Research* 68: 447–466, doi:10.1016/j.asr.2019.11.033.
- Ayoub, N. K., Chidichimo, M. P., Dever, E., Guo, X., Kim, S. Y., Krug, M., Míguez, B. M., Morris, T., Roughan, M., Sprintall, J., Tanaka, K., Todd, R. E., Wilkin, J., Álvarez-Fanjul, E., Andres, M., Bosse, A., Edwards, C. A., Gula, J., Kerry, C. G., Miyazawa, Y., Oddo, P., Oka, E. and Zaba, K. D. (2024). Observing Ocean Boundary Currents: Lessons Learned from Six Regions with Mature Observational and Modeling Systems. *Oceanography* 37: 82–91, doi:10.5670/oceanog.2024.504.
- Beal, L. M. and Eliot, S. (2016). Broadening not strengthening of the Agulhas Current since the early 1990s. *Nature* 540: 570–573, doi:10.1038/nature19853.
- Beal, L. M., Eliot, S., Houk, A. and Leber, G. M. (2015). Capturing the Transport Variability of

a Western Boundary Jet: Results from the Agulhas Current Time-Series Experiment (ACT)\*. *Journal of Physical Oceanography* 45: 1302–1324, doi:10.1175/JPO-D-14-0119.1.

Bindoff, N. L. and McDougall, T. J. (1994). Diagnosing Climate Change and Ocean Ventilation Using Hydrographic Data. *Journal of Physical Oceanography* 24: 1137–1152, doi:10.1175/1520-0485(1994)024<1137:DCCAOV>2.0.CO;2.

Bond, N. A. and Cronin, M. F. (2008). Regional Weather Patterns during Anomalous Air–Sea Fluxes at the Kuroshio Extension Observatory (KEO). *Journal of Climate* 21: 1680–1697, doi:10.1175/2007JCLI1797.1.

Book, J. W., Wimbush, M., Imawaki, S., Ichikawa, H., Uchida, H. and Kinoshita, H. (2002). Kuroshio temporal and spatial variations south of Japan determined from inverted echo sounder measurements. *Journal of Geophysical Research: Oceans* 107: 4–1–4–12, doi:10.1029/2001JC000795.

Brum, A. L., Azevedo, J. L. L. de and Dengler, M. (2023). Energetics of eddy–mean flow interactions in the deep western boundary current off the northeastern coast of Brazil. *Deep Sea Research Part I: Oceanographic Research Papers* 193: 103965, doi:10.1016/j.dsr.2023.103965.

Bryden, H. L., Beal, L. M. and Duncan, L. M. (2005). Structure and Transport of the Agulhas Current and Its Temporal Variability. *Journal of Oceanography* 61: 479–492, doi:10.1007/s10872-005-0057-8.

Cai, L., Xu, L., Tang, D., Shao, W., Liu, Y., Zuo, J. and Ji, Q. (2020). The effects of ocean temperature gradients on bigeye tuna (*Thunnus obesus*) distribution in the equatorial eastern Pacific Ocean. *Advances in Space Research* 65: 2749–2760, doi:10.1016/j.asr.2020.03.030.

Capotondi, A., Wittenberg, A. T., Newman, M., Di Lorenzo, E., Yu, J.-Y., Braconnot, P., Cole, J., Dewitte, B., Giese, B., Guilyardi, E., Jin, F.-F., Karnauskas, K., Kirtman, B., Lee, T., Schneider, N., Xue, Y. and Yeh, S.-W. (2015). Understanding ENSO Diversity. *Bulletin of the American Meteorological Society* 96: 921–938, doi:10.1175/BAMS-D-13-00117.1.

Cavole, L., Demko, A., Diner, R., Giddings, A., Koester, I., Pagniello, C., Paulsen, M.-L., Ramirez-Valdez, A., Schwenck, S., Yen, N., Zill, M. and Franks, P. (2016). Biological Impacts of the 2013–2015 Warm-Water Anomaly in the Northeast Pacific: Winners, Losers, and the Future. *Oceanography* 29, doi:10.5670/oceanog.2016.32.

Cetina-Heredia, P., Roughan, M., Sebille, E. van and Coleman, M. A. (2014). Long-term trends in the East Australian Current separation latitude and eddy driven transport. *Journal of Geophysical Research: Oceans* 119: 4351–4366, doi:10.1002/2014JC010071.

Chandler, M. (2024a). Data in support of 'The deep western boundary current of the Southwest Pacific Basin: Insights from Deep Argo' [dataset]. doi:10.5281/zenodo.10791519.

Chandler, M. (2024b). Data in support of 'The influence of ENSO on subsurface marine heatwave occurrence in the Kuroshio Extension' [dataset]. doi:10.5281/zenodo.14219180.

Chandler, M., Zilberman, N. V. and Sprintall, J. (2022a). Seasonal to Decadal Western Boundary Current Variability From Sustained Ocean Observations. *Geophysical Research Letters* 49: e2022GL097834, doi:10.1029/2022GL097834.

Chandler, M., Zilberman, N. V. and Sprintall, J. (2022b). Seasonal to decadal western boundary current variability from sustained ocean observations [dataset]. doi:10.5281/ZENODO.5851312.

Chandler, M., Zilberman, N. V. and Sprintall, J. (2024). The Deep Western Boundary Current of the Southwest Pacific Basin: Insights From Deep Argo. *Journal of Geophysical Research: Oceans* 129: e2024JC021098, doi:10.1029/2024JC021098.

CMEAMS (2018). Global Ocean Physics Reanalysis [Dataset]. doi:10.48670/MOI-00021.

CMEAMS (2024a). Global Ocean Gridded L4 Sea Surface Heights and Derived Variables Reprocessed 1993–Ongoing [dataset]. doi:10.48670/MOI-00148.

CMEAMS (2024b). Global Ocean Physics Reanalysis [Dataset]. doi:10.48670/MOI-00021.

Cole, S. T., Wortham, C., Kunze, E. and Owens, W. B. (2015). Eddy stirring and horizontal diffusivity from Argo float observations: Geographic and depth variability. *Geophysical Research Letters* 42: 3989–3997, doi:10.1002/2015GL063827.

Colling, A., Brown, E., Park, D., Phillips, J., Rothery, D., Wright, J. and The Open University Course Team (2001). *Ocean Circulation*. Oxford: Butterworth Heinemann, in association with The Open University, 2nd ed., doi:10.1016/B978-0-7506-5278-0.X5012-7.

Cronin, M. F., Bond, N., Booth, J., Ichikawa, H., Joyce, T. M., Kelly, K., Kubota, M., Qiu, B., Reason, C., Rouault, M., Sabine, C., Saino, T., Small, J., Suga, T., Talley, L. D., Thompson, L. and Weller, R. A. (2010). Monitoring Ocean - Atmosphere Interactions in Western Boundary Current Extensions. In *Proceedings of OceanObs'09: Sustained Ocean Observations and Information for Society*, 2. Venice, Italy: European Space Agency, 199–209, doi:10.5270/OceanObs09.cwp.20.

Cushman-Roisin, B. and Beckers, J.-M. (2011). *Introduction to Geophysical Fluid Dynamics: Physical and Numerical Aspects*. Massachusetts: Academic Press, 2nd ed.

de Boyer Montégut, C. (2023). Mixed layer depth climatology computed with a density threshold criterion of 0.03 kg/m<sup>3</sup> from 10 m depth value [dataset]. doi:10.17882/91774.

de Boyer Montégut, C., Madec, G., Fischer, A. S., Lazar, A. and Iudicone, D. (2004). Mixed layer

depth over the global ocean: An examination of profile data and a profile-based climatology. *Journal of Geophysical Research: Oceans* 109, doi:10.1029/2004JC002378.

Dengler, M., Schott, F. A., Eden, C., Brandt, P., Fischer, J. and Zantopp, R. J. (2004). Break-up of the Atlantic deep western boundary current into eddies at 8° S. *Nature* 432: 1018–1020, doi:10.1038/nature03134.

Desbruyères, D. G., Bravo, E. P., Thierry, V., Mercier, H., Lherminier, P., Cabanes, C., Biló, T. C., Fried, N. and Femke De Jong, M. (2022). Warming-to-Cooling Reversal of Overflow-Derived Water Masses in the Irminger Sea During 2002–2021. *Geophysical Research Letters* 49: e2022GL098057, doi:10.1029/2022GL098057.

Desbruyères, D. G., Purkey, S. G., McDonagh, E. L., Johnson, G. C. and King, B. A. (2016). Deep and abyssal ocean warming from 35 years of repeat hydrography. *Geophysical Research Letters* 43: 10,356–10,365, doi:10.1002/2016GL070413.

Diabaté, S. T., Swingedouw, D., Hirschi, J. J.-M., Duche, A., Leadbitter, P. J., Haigh, I. D. and McCarthy, G. D. (2021). Western boundary circulation and coastal sea-level variability in Northern Hemisphere oceans. *Ocean Science* 17: 1449–1471, doi:10.5194/os-17-1449-2021.

Dillon, T. M. (1982). Vertical overturns: A comparison of Thorpe and Ozmidov length scales. *Journal of Geophysical Research: Oceans* 87: 9601–9613, doi:10.1029/JC087iC12p09601.

Donohue, K. A., Watts, D. R., Tracey, K., Wimbush, M., Park, J.-H., Bond, N., Cronin, M., Chen, S., Qiu, B., Hacker, P., Hogg, N., Jayne, S., McClean, J., Rainville, L., Mitsudera, H., Tanimoto, Y. and Xie, S.-P. (2008). Program Studies the Kuroshio Extension. *Eos, Transactions American Geophysical Union* 89: 161–162, doi:10.1029/2008EO170002.

Donohue, K. A., Watts, D. R., Tracey, K. L., Greene, A. D. and Kennelly, M. (2010). Mapping Circulation in the Kuroshio Extension with an Array of Current and Pressure Recording Inverted Echo Sounders. *Journal of Atmospheric and Oceanic Technology* 27: 507–527, doi:10.1175/2009JTECHO686.1.

Draper, N. R. and Smith, H. (1998). *Applied Regression Analysis*. Wiley Series in Probability and Statistics. New York: John Wiley & Sons, 3rd ed., doi:10.1002/9781118625590.

Du, Y., Feng, M., Xu, Z., Yin, B. and Hobday, A. J. (2022). Summer Marine Heatwaves in the Kuroshio-Oyashio Extension Region. *Remote Sensing* 14: 2980, doi:10.3390/rs14132980.

Elipot, S. and Beal, L. M. (2015). Characteristics, Energetics, and Origins of Agulhas Current Meanders and Their Limited Influence on Ring Shedding. *Journal of Physical Oceanography* 45: 2294–2314, doi:10.1175/JPO-D-14-0254.1.

Elzahaby, Y. and Schaeffer, A. (2019). Observational Insight Into the Subsurface Anomalies of

Marine Heatwaves. *Frontiers in Marine Science* 6, doi:10.3389/fmars.2019.00745.

Elzahaby, Y., Schaeffer, A., Roughan, M. and Delaux, S. (2021). Oceanic Circulation Drives the Deepest and Longest Marine Heatwaves in the East Australian Current System. *Geophysical Research Letters* 48: e2021GL094785, doi:10.1029/2021GL094785.

Emery, W. J. and Thomson, R. E. (2001). *Data Analysis Methods in Physical Oceanography*. Amsterdam: Elsevier, 2nd ed.

Ezer, T., Atkinson, L. P., Corlett, W. B. and Blanco, J. L. (2013). Gulf Stream's induced sea level rise and variability along the U.S. mid-Atlantic coast. *Journal of Geophysical Research: Oceans* 118: 685–697, doi:10.1002/jgrc.20091.

Farchadi, N., McDonnell, L. H., Ryan, S., Lewison, R. L. and Braun, C. D. (2025). Marine heatwaves are in the eye of the beholder. *Nature Climate Change* 15: 236–239, doi:10.1038/s41558-025-02257-6.

Ffield, A. and Gordon, A. L. (1992). Vertical Mixing in the Indonesian Thermocline. *Journal of Physical Oceanography* 22: 184–195, doi:10.1175/1520-0485(1992)022<0184:VMITIT>2.0.CO;2.

Foppert, A., Rintoul, S. R., Purkey, S. G., Zilberman, N., Kobayashi, T., Sallée, J.-B., van Wijk, E. M. and Wallace, L. O. (2021). Deep Argo Reveals Bottom Water Properties and Pathways in the Australian-Antarctic Basin. *Journal of Geophysical Research: Oceans* 126: e2021JC017935, doi:10.1029/2021JC017935.

Fujioka, K., Fukuda, H., Furukawa, S., Tei, Y., Okamoto, S. and Ohshima, S. (2018). Habitat use and movement patterns of small (age-0) juvenile Pacific bluefin tuna (*Thunnus orientalis*) relative to the Kuroshio. *Fisheries Oceanography* 27: 185–198, doi:10.1111/fog.12244.

Fukamachi, Y., Rintoul, S. R., Church, J. A., Aoki, S., Sokolov, S., Rosenberg, M. A. and Wakatsuchi, M. (2010). Strong export of Antarctic Bottom Water east of the Kerguelen plateau. *Nature Geoscience* 3: 327–331, doi:10.1038/ngeo842.

Gasparin, F., Hamon, M., Rémy, E. and Traon, P.-Y. L. (2020). How Deep Argo Will Improve the Deep Ocean in an Ocean Reanalysis. *Journal of Climate* 33: 77–94, doi:10.1175/JCLI-D-19-0208.1.

GEBCO Compilation Group (2023). GEBCO 2023 Grid [dataset]. doi:10.5285/f98b053b-0cbc-6c23-e053-6c86abc0af7b.

Gill, A. E. (1982). *Atmosphere-Ocean Dynamics*. Academic Press.

Gilson, J. and Roemmich, D. (2002). Mean and Temporal Variability in Kuroshio Geostrophic

Transport South of Taiwan (1993–2001). *Journal of Oceanography* 58: 183–195, doi:10.1023/A:1015841120927.

Gilson, J., Roemmich, D., Cornuelle, B. and Fu, L.-L. (1998). Relationship of TOPEX/Poseidon altimetric height to steric height and circulation in the North Pacific. *Journal of Geophysical Research: Oceans* 103: 27947–27965, doi:10.1029/98JC01680.

Goes, M., Goni, G., Dong, S., Boyer, T. and Baringer, M. (2020). The complementary value of XBT and Argo observations to monitor ocean boundary currents and meridional heat and volume transports: A case study in the Atlantic Ocean. *Journal of Atmospheric and Oceanic Technology* : 1–42doi:10.1175/JTECH-D-20-0027.1.

Goni, G. J., Sprintall, J., Bringas, F., Cheng, L., Cirano, M., Dong, S., Domingues, R., Goes, M., Lopez, H., Morrow, R., Rivero, U., Rossby, T., Todd, R. E., Trinanes, J., Zilberman, N., Baringer, M., Boyer, T., Cowley, R., Domingues, C. M., Hutchinson, K., Kramp, M., Mata, M. M., Reseghetti, F., Sun, C., Bhaskar TVS, U. and Volkov, D. (2019). More Than 50 Years of Successful Continuous Temperature Section Measurements by the Global Expendable Bathymeterograph Network, Its Integrability, Societal Benefits, and Future. *Frontiers in Marine Science* 6, doi:10.3389/fmars.2019.00452.

Greene, C. A., Thirumalai, K., Kearney, K. A., Delgado, J. M., Schwanghart, W., Wolfenbarger, N. S., Thyng, K. M., Gwyther, D. E., Gardner, A. S. and Blankenship, D. D. (2019). The Climate Data Toolbox for MATLAB. *Geochemistry, Geophysics, Geosystems* 20: 3774–3781, doi:10.1029/2019GC008392.

Gregory, C. H., Artana, C., Lama, S., León-FonFay, D., Sala, J., Xiao, F., Xu, T., Capotondi, A., Martinez-Villalobos, C. and Holbrook, N. J. (2024). Global Marine Heatwaves Under Different Flavors of ENSO. *Geophysical Research Letters* 51: e2024GL110399, doi:10.1029/2024GL110399.

Großelindemann, H., Ryan, S., Ummenhofer, C. C., Martin, T. and Biastoch, A. (2022). Marine Heatwaves and Their Depth Structures on the Northeast U.S. Continental Shelf. *Frontiers in Climate* 4, doi:10.3389/fclim.2022.857937.

Gunn, K. L., Rintoul, S. R., England, M. H. and Bowen, M. M. (2023). Recent reduced abyssal overturning and ventilation in the Australian Antarctic Basin. *Nature Climate Change* 13: 1–8, doi:10.1038/s41558-023-01667-8.

Häkkinen, S., Rhines, P. B. and Worthen, D. L. (2015). Heat content variability in the North Atlantic Ocean in ocean reanalyses. *Geophysical Research Letters* 42: 2901–2909, doi:10.1002/2015GL063299.

Hayashida, H., Matear, R. J., Strutton, P. G. and Zhang, X. (2020). Insights into projected changes in marine heatwaves from a high-resolution ocean circulation model. *Nature Communications*

11: 4352, doi:10.1038/s41467-020-18241-x.

Hersbach, H., Bell, B., Berrisford, P., Biavati, G., Horányi, A., Muñoz Sabater, J., Nicolas, J., Peubey, C., Radu, R., Rozum, I., Schepers, D., Simmons, A., Soci, C., Dee, D. and Thépaut, J.-N. (2023). ERA5 monthly averaged data on single levels from 1940 to present [Dataset]. doi:10.24381/CDS.F17050D7.

Hersbach, H., Bell, B., Berrisford, P., Hirahara, S., Horányi, A., Muñoz-Sabater, J., Nicolas, J., Peubey, C., Radu, R., Schepers, D., Simmons, A., Soci, C., Abdalla, S., Abellan, X., Balsamo, G., Bechtold, P., Biavati, G., Bidlot, J., Bonavita, M., De Chiara, G., Dahlgren, P., Dee, D., Diamantakis, M., Dragani, R., Flemming, J., Forbes, R., Fuentes, M., Geer, A., Haimberger, L., Healy, S., Hogan, R. J., Hólm, E., Janisková, M., Keeley, S., Laloyaux, P., Lopez, P., Lupu, C., Radnoti, G., de Rosnay, P., Rozum, I., Vamborg, F., Villaume, S. and Thépaut, J.-N. (2020). The ERA5 global reanalysis. *Quarterly Journal of the Royal Meteorological Society* 146: 1999–2049, doi:10.1002/qj.3803.

Hobday, A. J., Alexander, L. V., Perkins, S. E., Smale, D. A., Straub, S. C., Oliver, E. C. J., Benthuysen, J. A., Burrows, M. T., Donat, M. G., Feng, M., Holbrook, N. J., Moore, P. J., Scannell, H. A., Sen Gupta, A. and Wernberg, T. (2016). A hierarchical approach to defining marine heatwaves. *Progress in Oceanography* 141: 227–238, doi:10.1016/j.pocean.2015.12.014.

Holbrook, N. J., Goodwin, I. D., McGregor, S., Molina, E. and Power, S. B. (2011). ENSO to multi-decadal time scale changes in East Australian Current transports and Fort Denison sea level: Oceanic Rossby waves as the connecting mechanism. *Deep Sea Research Part II: Topical Studies in Oceanography* 58: 547–558, doi:10.1016/j.dsr2.2010.06.007.

Holbrook, N. J., Scannell, H. A., Sen Gupta, A., Benthuysen, J. A., Feng, M., Oliver, E. C. J., Alexander, L. V., Burrows, M. T., Donat, M. G., Hobday, A. J., Moore, P. J., Perkins-Kirkpatrick, S. E., Smale, D. A., Straub, S. C. and Wernberg, T. (2019). A global assessment of marine heatwaves and their drivers. *Nature Communications* 10: 2624, doi:10.1038/s41467-019-10206-z.

Hu, D., Wu, L., Cai, W., Gupta, A. S., Ganachaud, A., Qiu, B., Gordon, A. L., Lin, X., Chen, Z., Hu, S., Wang, G., Wang, Q., Sprintall, J., Qu, T., Kashino, Y., Wang, F. and Kessler, W. S. (2015). Pacific western boundary currents and their roles in climate. *Nature* 522: 299–308, doi:10.1038/nature14504.

Hu, S., Li, S., Zhang, Y., Guan, C., Du, Y., Feng, M., Ando, K., Wang, F., Schiller, A. and Hu, D. (2021). Observed strong subsurface marine heatwaves in the tropical western Pacific Ocean. *Environmental Research Letters* 16: 104024, doi:10.1088/1748-9326/ac26f2.

Huang, B., Liu, C., Banzon, V., Freeman, E., Graham, G., Hankins, B., Smith, T. and Zhang, H.-M. (2021). Improvements of the Daily Optimum Interpolation Sea Surface Temperature (DOISST) Version 2.1. *Journal of Climate* 34: 2923–2939, doi:10.1175/JCLI-D-20-0166.1.

- Huang, B., Liu, C., Banzon, V. F., Freeman, E., Graham, G., Hankins, W., Smith, T. M. and Zhang, H.-M. (2024). NOAA 0.25-degree Daily Optimum Interpolation Sea Surface Temperature (OISST), Version 2.1 [dataset]. doi:10.25921/RE9P-PT57.
- Hutchinson, K., Beal, L. M., Penven, P., Ansorge, I. and Hermes, J. (2018). Seasonal Phasing of Agulhas Current Transport Tied to a Baroclinic Adjustment of Near-Field Winds. *Journal of Geophysical Research: Oceans* 123: 7067–7083, doi:10.1029/2018JC014319.
- Jacox, M. G., Alexander, M. A., Amaya, D., Becker, E., Bograd, S. J., Brodie, S., Hazen, E. L., Pozo Buil, M. and Tommasi, D. (2022). Global seasonal forecasts of marine heatwaves. *Nature* 604: 486–490, doi:10.1038/s41586-022-04573-9.
- Jacox, M. G., Alexander, M. A., Bograd, S. J. and Scott, J. D. (2020). Thermal displacement by marine heatwaves. *Nature* 584: 82–86, doi:10.1038/s41586-020-2534-z.
- Jayne, S. R., Hogg, N. G., Waterman, S. N., Rainville, L., Donohue, K. A., Randolph Watts, D., Tracey, K. L., McClean, J. L., Maltrud, M. E., Qiu, B., Chen, S. and Hacker, P. (2009). The Kuroshio Extension and its recirculation gyres. *Deep Sea Research Part I: Oceanographic Research Papers* 56: 2088–2099, doi:10.1016/j.dsr.2009.08.006.
- Johnson, G. C. (1998). Deep water properties, velocities, and dynamics over ocean trenches. *Journal of Marine Research* 56: 329–347.
- Johnson, G. C. (2008). Quantifying Antarctic Bottom Water and North Atlantic Deep Water volumes. *Journal of Geophysical Research: Oceans* 113, doi:10.1029/2007JC004477.
- Johnson, G. C. (2022). Antarctic Bottom Water Warming and Circulation Slowdown in the Argentine Basin From Analyses of Deep Argo and Historical Shipboard Temperature Data. *Geophysical Research Letters* 49: e2022GL100526, doi:10.1029/2022GL100526.
- Johnson, G. C., Cadot, C., Lyman, J. M., McTaggart, K. E. and Steffen, E. L. (2020). Antarctic Bottom Water Warming in the Brazil Basin: 1990s Through 2020, From WOCE to Deep Argo. *Geophysical Research Letters* 47: e2020GL089191, doi:10.1029/2020GL089191.
- Johnson, G. C., Purkey, S. G., Zilberman, N. V. and Roemmich, D. (2019). Deep Argo Quantifies Bottom Water Warming Rates in the Southwest Pacific Basin. *Geophysical Research Letters* 46: 2662–2669, doi:10.1029/2018GL081685.
- Johnson, G. C., Whalen, C. B., Purkey, S. G. and Zilberman, N. (2022). Serendipitous Internal Wave Signals in Deep Argo Data. *Geophysical Research Letters* 49: e2022GL097900, doi:10.1029/2022GL097900.
- Kawabe, M. (1985). Sea level variations at the Izu Islands and typical stable paths of the Kuroshio. *Journal of the Oceanographical Society of Japan* 41: 307–326, doi:10.1007/BF02109238.

Kawabe, M. (1995). Variations of Current Path, Velocity, and Volume Transport of the Kuroshio in Relation with the Large Meander. *Journal of Physical Oceanography* 25: 3103–3117, doi:10.1175/1520-0485(1995)025<3103:VOCPVA>2.0.CO;2.

Kawakami, Y., Nakano, H., Urakawa, L. S., Toyoda, T., Sakamoto, K., Nishikawa, S., Sugiyama, T., Kurogi, M., Ishikawa, Y., Sato, K. and Yamanaka, G. (2024). Future changes in marine heatwaves based on high-resolution ensemble projections for the northwestern Pacific Ocean. *Journal of Oceanography* 80: 177–195, doi:10.1007/s10872-024-00714-y.

Kerry, C. and Roughan, M. (2020). Downstream Evolution of the East Australian Current System: Mean Flow, Seasonal, and Intra-annual Variability. *Journal of Geophysical Research: Oceans* 125, doi:10.1029/2019JC015227.

Kitagawa, T., Kato, Y., Miller, Michael. J., Sasai, Y., Sasaki, H. and Kimura, S. (2010). The restricted spawning area and season of Pacific bluefin tuna facilitate use of nursery areas: A modeling approach to larval and juvenile dispersal processes. *Journal of Experimental Marine Biology and Ecology* 393: 23–31, doi:10.1016/j.jembe.2010.06.016.

Köhl, A. (2014). Detecting Processes Contributing to Interannual Halosteric and Thermosteric Sea Level Variability. *Journal of Climate* 27: 2417–2426, doi:10.1175/JCLI-D-13-00412.1.

Kouketsu, S., Doi, T., Kawano, T., Masuda, S., Sugiura, N., Sasaki, Y., Toyoda, T., Igarashi, H., Kawai, Y., Katsumata, K., Uchida, H., Fukasawa, M. and Awaji, T. (2011). Deep ocean heat content changes estimated from observation and reanalysis product and their influence on sea level change. *Journal of Geophysical Research: Oceans* 116, doi:10.1029/2010JC006464.

Krug, M. and Tournadre, J. (2012). Satellite observations of an annual cycle in the Agulhas Current. *Geophysical Research Letters* 39, doi:10.1029/2012GL052335.

LaCasce, J. H. and Groeskamp, S. (2020). Baroclinic Modes over Rough Bathymetry and the Surface Deformation Radius. *Journal of Physical Oceanography* 50: 2835–2847, doi:10.1175/JPO-D-20-0055.1.

Leber, G. M. and Beal, L. M. (2014). Evidence that Agulhas Current transport is maintained during a meander. *Journal of Geophysical Research: Oceans* 119: 3806–3817, doi:10.1002/2014JC009802.

Lee, T. N., Johns, W. E., Liu, C.-T., Zhang, D., Zantopp, R. and Yang, Y. (2001). Mean transport and seasonal cycle of the Kuroshio east of Taiwan with comparison to the Florida Current. *Journal of Geophysical Research: Oceans* 106: 22143–22158, doi:10.1029/2000JC000535.

Lee, T. N., Johns, W. E., Zantopp, R. J. and Fillenbaum, E. R. (1996). Moored Observations of Western Boundary Current Variability and Thermohaline Circulation at 26.5° in the Subtropical North Atlantic. *Journal of Physical Oceanography* 26: 962–983, doi:10.1175/1520-

0485(1996)026<0962:MOOWBC>2.0.CO;2.

Lellouche, J.-M., Greiner, E., Bourdallé-Badie, R., Garric, G., Melet, A., Drévillon, M., Bricaud, C., Hamon, M., Le Galloudec, O., Regnier, C., Candela, T., Testut, C.-E., Gasparin, F., Ruggiero, G., Benkiran, M., Drillet, Y. and Le Traon, P.-Y. (2021). The Copernicus Global 1/12° Oceanic and Sea Ice GLORYS12 Reanalysis. *Frontiers in Earth Science* 9, doi:10.3389/feart.2021.698876.

Lellouche, J.-M., Greiner, E., Le Galloudec, O., Garric, G., Regnier, C., Drevillon, M., Benkiran, M., Testut, C.-E., Bourdalle-Badie, R., Gasparin, F., Hernandez, O., Levier, B., Drillet, Y., Remy, E. and Le Traon, P.-Y. (2018). Recent updates to the Copernicus Marine Service global ocean monitoring and forecasting real-time 1/12° high-resolution system. *Ocean Science* 14: 1093–1126, doi:10.5194/os-14-1093-2018.

Li, Z., Holbrook, N. J., Zhang, X., Oliver, E. C. J. and Cougnon, E. A. (2020). Remote Forcing of Tasman Sea Marine Heatwaves. *Journal of Climate* 33: 5337–5354, doi:10.1175/JCLI-D-19-0641.1.

Litzow, M. A., Hunsicker, M. E., Bond, N. A., Burke, B. J., Cunningham, C. J., Gosselin, J. L., Norton, E. L., Ward, E. J. and Zador, S. G. (2020). The changing physical and ecological meanings of North Pacific Ocean climate indices. *Proceedings of the National Academy of Sciences* 117: 7665–7671, doi:10.1073/pnas.1921266117.

Liu, Z.-J., Zhu, X.-H., Nakamura, H., Nishina, A., Wang, M. and Zheng, H. (2021). Comprehensive Observational Features for the Kuroshio Transport Decreasing Trend During a Recent Global Warming Hiatus. *Geophysical Research Letters* 48: e2021GL094169, doi:10.1029/2021GL094169.

Locarnini, R. A., Mishonov, A. V., Baranova, O. K., Reagan, J. R., Boyer, T. P., Seidov, D., Wang, Z., Garcia, H. E., Bouchard, C., Cross, S. L., Paver, C. R. and Dukhovskoy, D. (2024). World Ocean Atlas 2023, Volume 1: Temperature. *NOAA Atlas NESDIS* 89 doi:10.25923/54BH-1613.

Masuda, S., Awaji, T., Sugiura, N., Matthews, J. P., Toyoda, T., Kawai, Y., Doi, T., Kouketsu, S., Igarashi, H., Katsumata, K., Uchida, H., Kawano, T. and Fukasawa, M. (2010). Simulated Rapid Warming of Abyssal North Pacific Waters. *Science* 329: 319–322, doi:10.1126/science.1188703.

Mata, M. M., Tomczak, M., Wijffels, S. and Church, J. A. (2000). East Australian Current volume transports at 30°S: Estimates from the World Ocean Circulation Experiment hydrographic sections PR11/P6 and the PCM3 current meter array. *Journal of Geophysical Research: Oceans* 105: 28509–28526, doi:10.1029/1999JC000121.

McDougall, T. J. and Barker, P. M. (2011). *Getting Started with TEOS-10 and the Gibbs Seawater (GSW) Oceanographic Toolbox*. Battery Point, Tas.: SCOR/IAPSO WG127.

Meinen, C. S., Garzoli, S. L., Perez, R. C., Campos, E., Piola, A. R., Chidichimo, M. P., Dong, S. and Sato, O. T. (2017). Characteristics and causes of Deep Western Boundary Current transport variability at 34.5° S during 2009–2014. *Ocean Science* 13: 175–194, doi:10.5194/os-13-175-2017.

Mills, K., Pershing, A., Brown, C., Chen, Y., Chiang, F.-S., Holland, D., Lehuta, S., Nye, J., Sun, J., Thomas, A. and Wahle, R. (2013). Fisheries Management in a Changing Climate: Lessons From the 2012 Ocean Heat Wave in the Northwest Atlantic. *Oceanography* 26, doi:10.5670/oceanog.2013.27.

Miloslavich, P., O'Callaghan, J., Heslop, E., McConnell, T., Heupel, M., Satterthwaite, E., Lorenzoni, L., Schloss, I., Belbeoch, M., Rome, N., Widdicombe, S., Olalekan Elegbede, I. and Fontela, M. (2024). Ocean Decade Vision 2030 White Papers – Challenge 7: Sustainably Expand the Global Ocean Observing System. *The Ocean Decade Series*, 51.7 doi:10.25607/BRXB-KR45.

Minobe, S., Kuwano-Yoshida, A., Komori, N., Xie, S.-P. and Small, R. J. (2008). Influence of the Gulf Stream on the troposphere. *Nature* 452: 206–209, doi:10.1038/nature06690.

Moore, M. I. and Wilkin, J. L. (1998). Variability in the South Pacific Deep Western Boundary Current from current meter observations and a high-resolution global model. *Journal of Geophysical Research: Oceans* 103: 5439–5457, doi:10.1029/97JC03207.

Morris, T., Rudnick, D., Sprintall, J., Hermes, J., Goni, G., Parks, J., Bringas, F., Heslop, E. and the numerous contributors to the OCG-12 Boundary Current Workshop and OceanGliders BOON Project (2021). Monitoring Boundary Currents Using Ocean Observing Infrastructure. *Oceanography* 34: 16–17, doi:10.5670/oceanog.2021.supplement.02-07.

Munk, W. H. (1966). Abyssal recipes. *Deep Sea Research and Oceanographic Abstracts* 13: 707–730, doi:10.1016/0011-7471(66)90602-4.

Nakamura, H., Sampe, T., Goto, A., Ohfuchi, W. and Xie, S.-P. (2008). On the importance of mid-latitude oceanic frontal zones for the mean state and dominant variability in the tropospheric circulation. *Geophysical Research Letters* 35, doi:10.1029/2008GL034010.

Newman, M., Alexander, M. A., Ault, T. R., Cobb, K. M., Deser, C., Lorenzo, E. D., Mantua, N. J., Miller, A. J., Minobe, S., Nakamura, H., Schneider, N., Vimont, D. J., Phillips, A. S., Scott, J. D. and Smith, C. A. (2016). The Pacific Decadal Oscillation, Revisited. *Journal of Climate* 29: 4399–4427, doi:10.1175/JCLI-D-15-0508.1.

Nhantumbo, B. J., Nilsen, J. E. Ø., Backeberg, B. C. and Reason, C. J. C. (2020). The relationship between coastal sea level variability in South Africa and the Agulhas Current. *Journal of Marine Systems* 211: 103422, doi:10.1016/j.jmarsys.2020.103422.

- Njouodo, A. S. N., Koseki, S., Keenlyside, N. and Rouault, M. (2018). Atmospheric Signature of the Agulhas Current. *Geophysical Research Letters* 45: 5185–5193, doi:10.1029/2018GL077042.
- NOAA (2009). ETOPO1 1 Arc-Minute Global Relief Model [Dataset]. doi:10.7289/V5C8276M.
- Nonaka, M. and Xie, S.-P. (2003). Covariations of Sea Surface Temperature and Wind over the Kuroshio and Its Extension: Evidence for Ocean-to-Atmosphere Feedback. *Journal of Climate* 16: 1404–1413, doi:10.1175/1520-0442(2003)16<1404:COSSTA>2.0.CO;2.
- Noto, M. and Yasuda, I. (1999). Population decline of the Japanese sardine, *Sardinops melanostictus*, in relation to sea surface temperature in the Kuroshio Extension. *Canadian Journal of Fisheries and Aquatic Sciences* 56: 973–983, doi:10.1139/f99-028.
- Oka, E., Ishii, M., Nakano, T., Suga, T., Kouketsu, S., Miyamoto, M., Nakano, H., Qiu, B., Sugimoto, S. and Takatani, Y. (2018). Fifty years of the 137°E repeat hydrographic section in the western North Pacific Ocean. *Journal of Oceanography* 74: 115–145, doi:10.1007/s10872-017-0461-x.
- Oka, E., Katsura, S., Inoue, H., Kojima, A., Kitamoto, M., Nakano, T. and Suga, T. (2017). Long-term change and variation of salinity in the western North Pacific subtropical gyre revealed by 50-year long observations along 137°E. *Journal of Oceanography* 73: 479–490, doi:10.1007/s10872-017-0416-2.
- Oliver, E. C. J. (2019). Mean warming not variability drives marine heatwave trends. *Climate Dynamics* 53: 1653–1659, doi:10.1007/s00382-019-04707-2.
- Oliver, E. C. J., BenthuySEN, J. A., Bindoff, N. L., Hobday, A. J., Holbrook, N. J., Mundy, C. N. and Perkins-Kirkpatrick, S. E. (2017). The unprecedented 2015/16 Tasman Sea marine heatwave. *Nature Communications* 8: 16101, doi:10.1038/ncomms16101.
- Oliver, E. C. J., BenthuySEN, J. A., Darmaraki, S., Donat, M. G., Hobday, A. J., Holbrook, N. J., Schlegel, R. W. and Sen Gupta, A. (2021). Marine Heatwaves. *Annual Review of Marine Science* 13: 313–342, doi:10.1146/annurev-marine-032720-095144.
- Oliver, E. C. J., Burrows, M. T., Donat, M. G., Sen Gupta, A., Alexander, L. V., Perkins-Kirkpatrick, S. E., BenthuySEN, J. A., Hobday, A. J., Holbrook, N. J., Moore, P. J., Thomsen, M. S., Wernberg, T. and Smale, D. A. (2019). Projected Marine Heatwaves in the 21st Century and the Potential for Ecological Impact. *Frontiers in Marine Science* 6, doi:10.3389/fmars.2019.00734.
- Oliver, E. C. J., Donat, M. G., Burrows, M. T., Moore, P. J., Smale, D. A., Alexander, L. V., Ben-thuySEN, J. A., Feng, M., Sen Gupta, A., Hobday, A. J., Holbrook, N. J., Perkins-Kirkpatrick, S. E., Scannell, H. A., Straub, S. C. and Wernberg, T. (2018). Longer and more frequent

marine heatwaves over the past century. *Nature Communications* 9: 1324, doi:10.1038/s41467-018-03732-9.

Oliver, E. C. J. and Holbrook, N. J. (2014). Extending our understanding of South Pacific gyre “spin-up”: Modeling the East Australian Current in a future climate. *Journal of Geophysical Research: Oceans* 119: 2788–2805, doi:10.1002/2013JC009591.

Pathmeswaran, C., Sen Gupta, A., Perkins-Kirkpatrick, S. E. and Hart, M. A. (2022). Exploring Potential Links Between Co-occurring Coastal Terrestrial and Marine Heatwaves in Australia. *Frontiers in Climate* 4, doi:10.3389/fclim.2022.792730.

Pershing, A. J., Mills, K. E., Dayton, A. M., Franklin, B. S. and Kennedy, B. T. (2018). Evidence for Adaptation from the 2016 Marine Heatwave in the Northwest Atlantic Ocean. *Oceanography* 31: 152–161, doi:10.5670/oceanog.2018.213.

Petit, T., Thierry, V. and Mercier, H. (2022). Deep through-flow in the Bight Fracture Zone. *Ocean Science* 18: 1055–1071, doi:10.5194/os-18-1055-2022.

Purkey, S. G. and Johnson, G. C. (2010). Warming of Global Abyssal and Deep Southern Ocean Waters between the 1990s and 2000s: Contributions to Global Heat and Sea Level Rise Budgets. *Journal of Climate* 23: 6336–6351, doi:10.1175/2010JCLI3682.1.

Purkey, S. G. and Johnson, G. C. (2012). Global Contraction of Antarctic Bottom Water between the 1980s and 2000s. *Journal of Climate* 25: 5830–5844, doi:10.1175/JCLI-D-11-00612.1.

Purkey, S. G. and Johnson, G. C. (2013). Antarctic Bottom Water Warming and Freshening: Contributions to Sea Level Rise, Ocean Freshwater Budgets, and Global Heat Gain. *Journal of Climate* 26: 6105–6122, doi:10.1175/JCLI-D-12-00834.1.

Purkey, S. G., Johnson, G. C., Talley, L. D., Sloyan, B. M., Wijffels, S. E., Smethie, W., Mecking, S. and Katsumata, K. (2019). Unabated Bottom Water Warming and Freshening in the South Pacific Ocean. *Journal of Geophysical Research: Oceans* 124: 1778–1794, doi:10.1029/2018JC014775.

Qiu, B. and Chen, S. (2005). Variability of the Kuroshio Extension Jet, Recirculation Gyre, and Mesoscale Eddies on Decadal Time Scales. *Journal of Physical Oceanography* 35: 2090–2103, doi:10.1175/JPO2807.1.

Qiu, B. and Chen, S. (2010). Eddy-mean flow interaction in the decadally modulating Kuroshio Extension system. *Deep Sea Research Part II: Topical Studies in Oceanography* 57: 1098–1110, doi:10.1016/j.dsr2.2008.11.036.

Qiu, B., Chen, S. and Oka, E. (2023). Why Did the 2017 Kuroshio Large Meander Event Become the Longest in the Past 70 Years? *Geophysical Research Letters* 50: e2023GL103548,

doi:10.1029/2023GL103548.

Qiu, B., Chen, S., Schneider, N., Oka, E. and Sugimoto, S. (2020). On the Reset of the Wind-Forced Decadal Kuroshio Extension Variability in Late 2017. *Journal of Climate* 33: 10813–10828, doi:10.1175/JCLI-D-20-0237.1.

Qiu, B., Chen, S., Schneider, N. and Taguchi, B. (2014). A Coupled Decadal Prediction of the Dynamic State of the Kuroshio Extension System. *Journal of Climate* 27: 1751–1764, doi:10.1175/JCLI-D-13-00318.1.

Racapé, V., Thierry, V., Mercier, H. and Cabanes, C. (2019). ISOW Spreading and Mixing as Revealed by Deep-Argo Floats Launched in the Charlie-Gibbs Fracture Zone. *Journal of Geophysical Research: Oceans* 124: 6787–6808, doi:10.1029/2019JC015040.

Reagan, J. R., Boyer, T. P., Garcia, H. E., Locarnini, R. A., Baranova, O. K., Bouchard, C., Cross, S. L., Mishonov, A. V., Paver, C. R., Seidov, D., Wang, K. and Dukhovskoy, D. (2024). World Ocean Atlas 2023 [dataset]. doi:10.25921/va26-hv25.

Reid, J. L. (1986). On the total geostrophic circulation of the South Pacific Ocean: Flow patterns, tracers and transports. *Progress in Oceanography* 16: 1–61, doi:10.1016/0079-6611(86)90036-4.

Reid, J. L. (1997). On the total geostrophic circulation of the pacific ocean: Flow patterns, tracers, and transports. *Progress in Oceanography* 39: 263–352, doi:10.1016/S0079-6611(97)00012-8.

Ridgway, K. R., Coleman, R. C., Bailey, R. J. and Sutton, P. (2008). Decadal variability of East Australian Current transport inferred from repeated high-density XBT transects, a CTD survey and satellite altimetry. *Journal of Geophysical Research* 113: C08039, doi:10.1029/2007JC004664.

Ridgway, K. R. and Godfrey, J. S. (1997). Seasonal cycle of the East Australian Current. *Journal of Geophysical Research: Oceans* 102: 22921–22936, doi:10.1029/97JC00227.

Riser, S. C., Freeland, H. J., Roemmich, D., Wijffels, S., Troisi, A., Belbéoch, M., Gilbert, D., Xu, J., Pouliquen, S., Thresher, A., Le Traon, P.-Y., Maze, G., Klein, B., Ravichandran, M., Grant, F., Poulain, P.-M., Suga, T., Lim, B., Sterl, A., Sutton, P., Mork, K.-A., Vélez-Belchí, P. J., Ansorge, I., King, B., Turton, J., Baringer, M. and Jayne, S. R. (2016). Fifteen years of ocean observations with the global Argo array. *Nature Climate Change* 6: 145–153, doi:10.1038/nclimate2872.

Roach, C. J., Balwada, D. and Speer, K. (2018). Global Observations of Horizontal Mixing from Argo Float and Surface Drifter Trajectories. *Journal of Geophysical Research: Oceans* 123: 4560–4575, doi:10.1029/2018JC013750.

Roemmich, D. (1983). Optimal Estimation of Hydrographic Station Data and Derived Fields. *Journal of Physical Oceanography* 13: 1544–1549, doi:10.1175/1520-0485(1983)013<1544:OEOHSD>2.0.CO;2.

Roemmich, D., Alford, M. H., Claustre, H., Johnson, K., King, B., Moum, J., Oke, P., Owens, W. B., Pouliquen, S., Purkey, S., Scanderbeg, M., Suga, T., Wijffels, S., Zilberman, N., Bakker, D., Baringer, M., Belbeoch, M., Bittig, H. C., Boss, E., Calil, P., Carse, F., Carval, T., Chai, F., Conchubhair, D. Ó., d'Ortenzio, F., Dall'Olmo, G., Desbruyeres, D., Fennel, K., Fer, I., Ferrari, R., Forget, G., Freeland, H., Fujiki, T., Gehlen, M., Greenan, B., Hallberg, R., Hibiya, T., Hosoda, S., Jayne, S., Jochum, M., Johnson, G. C., Kang, K., Kolodziejczyk, N., Körtzinger, A., Traon, P.-Y. L., Lenn, Y.-D., Maze, G., Mork, K. A., Morris, T., Nagai, T., Nash, J., Garabato, A. N., Olsen, A., Pattabhi, R. R., Prakash, S., Riser, S., Schmechtig, C., Schmid, C., Shroyer, E., Sterl, A., Sutton, P., Talley, L., Tanhua, T., Thierry, V., Thomalla, S., Toole, J., Troisi, A., Trull, T. W., Turton, J., Velez-Belchi, P. J., Walczowski, W., Wang, H., Wanninkhof, R., Waterhouse, A. F., Waterman, S., Watson, A., Wilson, C., Wong, A. P. S., Xu, J. and Yasuda, I. (2019a). On the Future of Argo: A Global, Full-Depth, Multi-Disciplinary Array. *Frontiers in Marine Science* 6, doi:10.3389/fmars.2019.00439.

Roemmich, D. and Gilson, J. (2009). The 2004–2008 mean and annual cycle of temperature, salinity, and steric height in the global ocean from the Argo Program. *Progress in Oceanography* 82: 81–100, doi:10.1016/j.pocean.2009.03.004.

Roemmich, D., Hautala, S. and Rudnick, D. (1996). Northward abyssal transport through the Samoan passage and adjacent regions. *Journal of Geophysical Research: Oceans* 101: 14039–14055, doi:10.1029/96JC00797.

Roemmich, D., Sherman, J. T., Davis, R. E., Grindley, K., McClune, M., Parker, C. J., Black, D. N., Zilberman, N., Purkey, S. G., Sutton, P. J. H. and Gilson, J. (2019b). Deep SOLO: A Full-Depth Profiling Float for the Argo Program. *Journal of Atmospheric and Oceanic Technology* 36: 1967–1981, doi:10.1175/JTECH-D-19-0066.1.

Roemmich, D., Talley, L., Zilberman, N., Osborne, E., Johnson, K., Barbero, L., Bittig, H., Briggs, N., Fassbender, A., Johnson, G., King, B., McDonagh, E., Purkey, S., Riser, S., Suga, T., Takeshita, Y., Thierry, V. and Wijffels, S. (2021). The Technological, Scientific, and Sociological Revolution of Global Subsurface Ocean Observing. *Oceanography* 34: 2–8, doi:10.5670/oceanog.2021.supplement.02-02.

Rouault, M. J. and Penven, P. (2011). New perspectives on Natal Pulses from satellite observations. *Journal of Geophysical Research: Oceans* 116, doi:10.1029/2010JC006866.

Rudnick, D. L. (1997). Direct velocity measurements in the Samoan Passage. *Journal of Geophysical Research: Oceans* 102: 3293–3302, doi:10.1029/96JC03286.

Rudnick, D. L. (2016). Ocean Research Enabled by Underwater Gliders. *Annual Review of*

*Marine Science* 8: 519–541, doi:10.1146/annurev-marine-122414-033913.

Salmon, R. (1998). *Lectures on Geophysical Fluid Dynamics*. New York: Oxford University Press, doi:10.1093/oso/9780195108088.001.0001.

Sasaki, Y. N., Minobe, S., Asai, T. and Inatsu, M. (2012). Influence of the Kuroshio in the East China Sea on the Early Summer (Baiu) Rain. *Journal of Climate* 25: 6627–6645, doi:10.1175/JCLI-D-11-00727.1.

Sasaki, Y. N., Minobe, S. and Miura, Y. (2014). Decadal sea-level variability along the coast of Japan in response to ocean circulation changes. *Journal of Geophysical Research: Oceans* 119: 266–275, doi:10.1002/2013JC009327.

Savidge, W. B., Savidge, D. K., Brandini, F., Greer, A. T., Hofmann, E. E., Roughan, M., da Silveira, I. and Suthers, I. M. (2024). Western Boundary Current–Subtropical Continental Shelf Interactions. *Oceanography* 37: 64–69, doi:10.5670/oceanog.2024.502.

Scanderbeg, M., Rannou, J.-P., Buck, J., Schmid, C., Gilson, J. and Swift, D. (2019). Argo DAC trajectory cookbook doi:10.13155/29824.

Scannell, H. A., Pershing, A. J., Alexander, M. A., Thomas, A. C. and Mills, K. E. (2016). Frequency of marine heatwaves in the North Atlantic and North Pacific since 1950. *Geophysical Research Letters* 43: 2069–2076, doi:10.1002/2015GL067308.

Schaeffer, A. and Roughan, M. (2017). Subsurface intensification of marine heatwaves off southeastern Australia: The role of stratification and local winds. *Geophysical Research Letters* 44: 5025–5033, doi:10.1002/2017GL073714.

Schaeffer, A., Sen Gupta, A. and Roughan, M. (2023). Seasonal stratification and complex local dynamics control the sub-surface structure of marine heatwaves in Eastern Australian coastal waters. *Communications Earth & Environment* 4: 1–12, doi:10.1038/s43247-023-00966-4.

Schott, F. A., Dengler, M., Zantopp, R., Stramma, L., Fischer, J. and Brandt, P. (2005). The Shallow and Deep Western Boundary Circulation of the South Atlantic at 5°–11°S. *Journal of Physical Oceanography* 35: 2031–2053, doi:10.1175/JPO2813.1.

Sen Gupta, A., Stellema, A., Pontes, G. M., Taschetto, A. S., Vergés, A. and Rossi, V. (2021). Future changes to the upper ocean Western Boundary Currents across two generations of climate models. *Scientific Reports* 11: 9538, doi:10.1038/s41598-021-88934-w.

Sen Gupta, A., Thomsen, M., Benthuysen, J. A., Hobday, A. J., Oliver, E., Alexander, L. V., Burrows, M. T., Donat, M. G., Feng, M., Holbrook, N. J., Perkins-Kirkpatrick, S., Moore, P. J., Rodrigues, R. R., Scannell, H. A., Taschetto, A. S., Ummenhofer, C. C., Wernberg, T. and Smale, D. A. (2020). Drivers and impacts of the most extreme marine heatwave events.

*Scientific Reports* 10: 19359, doi:10.1038/s41598-020-75445-3.

Send, U., Davis, R., Fischer, J., Imawaki, S., Kessler, W., Meinen, C., Owens, B., Roemmich, D., Rossby, T., Rudnick, D., Toole, J., Wijffles, S. and Beal, L. (2010). A Global Boundary Current Circulation Observing Network. In *Proceedings of OceanObs'09: Sustained Ocean Observations and Information for Society*, 2. Venice, Italy: European Space Agency, doi:10.5270/OceanObs09.cwp.78.

Sévellec, F., Verdière, A. C. de and Kolodziejczyk, N. (2022). Estimation of Horizontal Turbulent Diffusivity from Deep Argo Float Displacements. *Journal of Physical Oceanography* doi:10.1175/JPO-D-21-0150.1.

Sloyan, B. M., Ridgway, K. R. and Cowley, R. (2016). The East Australian Current and Property Transport at 27°S from 2012 to 2013. *Journal of Physical Oceanography* 46: 993–1008, doi:10.1175/JPO-D-15-0052.1.

Sloyan, B. M., Wanninkhof, R., Kramp, M., Johnson, G. C., Talley, L. D., Tanhua, T., McDonagh, E., Cusack, C., O'Rourke, E., McGovern, E., Katsumata, K., Diggs, S., Hummon, J., Ishii, M., Azetsu-Scott, K., Boss, E., Ansorge, I., Perez, F. F., Mercier, H., Williams, M. J. M., Anderson, L., Lee, J. H., Murata, A., Kouketsu, S., Jeansson, E., Hoppe, M. and Campos, E. (2019). The Global Ocean Ship-Based Hydrographic Investigations Program (GO-SHIP): A Platform for Integrated Multidisciplinary Ocean Science. *Frontiers in Marine Science* 6, doi:10.3389/fmars.2019.00445.

Sloyan, B. M., Wijffels, S. E., Tilbrook, B., Katsumata, K., Murata, A. and Macdonald, A. M. (2013). Deep Ocean Changes near the Western Boundary of the South Pacific Ocean. *Journal of Physical Oceanography* 43: 2132–2141, doi:10.1175/JPO-D-12-0182.1.

Smale, D. A., Wernberg, T., Oliver, E. C. J., Thomsen, M., Harvey, B. P., Straub, S. C., Burrows, M. T., Alexander, L. V., Benthuyzen, J. A., Donat, M. G., Feng, M., Hobday, A. J., Holbrook, N. J., Perkins-Kirkpatrick, S. E., Scannell, H. A., Sen Gupta, A., Payne, B. L. and Moore, P. J. (2019). Marine heatwaves threaten global biodiversity and the provision of ecosystem services. *Nature Climate Change* 9: 306–312, doi:10.1038/s41558-019-0412-1.

Smith, K. E., Burrows, M. T., Hobday, A. J., King, N. G., Moore, P. J., Sen Gupta, A., Thomsen, M. S., Wernberg, T. and Smale, D. A. (2023). Biological Impacts of Marine Heatwaves. *Annual Review of Marine Science* 15, doi:10.1146/annurev-marine-032122-121437.

Smith, K. E., Burrows, M. T., Hobday, A. J., Sen Gupta, A., Moore, P. J., Thomsen, M., Wernberg, T. and Smale, D. A. (2021). Socioeconomic impacts of marine heatwaves: Global issues and opportunities. *Science* 374, doi:10.1126/science.abj3593.

Smith, W. H. F. and Sandwell, D. T. (1997). Global Sea Floor Topography from Satellite Altimetry and Ship Depth Soundings. *Science* 277: 1956–1962, doi:10.1126/science.277.5334.1956.

- Song, H., Zhu, X.-H., Zhu, Z.-N., Chae, J.-Y., Jeon, C., Kim, D.-G., Min, H.-S., Lee, J.-H. and Park, J.-H. (2023). Seasonal Variability of the Deep Western Boundary Current in the Philippine Sea. *Journal of Marine Science and Engineering* 11: 1290, doi:10.3390/jmse11071290.
- Stommel, H. and Arons, A. B. (1959a). On the abyssal circulation of the world ocean — II. An idealized model of the circulation pattern and amplitude in oceanic basins. *Deep Sea Research* (1953) 6: 217–233, doi:10.1016/0146-6313(59)90075-9.
- Stommel, H. and Arons, A. B. (1959b). On the abyssal circulation of the world ocean—I. Stationary planetary flow patterns on a sphere. *Deep Sea Research* (1953) 6: 140–154, doi:10.1016/0146-6313(59)90065-6.
- Sugimoto, S., Hanawa, K., Narikiyo, K., Fujimori, M. and Suga, T. (2010). Temporal variations of the net Kuroshio transport and its relation to atmospheric variations. *Journal of Oceanography* 66: 611–619, doi:10.1007/s10872-010-0050-8.
- Sugimoto, S., Qiu, B. and Schneider, N. (2021). Local Atmospheric Response to the Kuroshio Large Meander Path in Summer and Its Remote Influence on the Climate of Japan. *Journal of Climate* 34: 3571–3589, doi:10.1175/JCLI-D-20-0387.1.
- Sun, J., Zhang, L. and Hu, D. (2022). Decadal and Long-Term Variability of Sea Level in the Southwestern Pacific During 1948–2018. *Geophysical Research Letters* 49: e2022GL098747, doi:10.1029/2022GL098747.
- Taburet, G., Sanchez-Roman, A., Ballarotta, M., Pujol, M.-I., Legeais, J.-F., Fournier, F., Faugere, Y. and Dibarboure, G. (2019). DUACS DT2018: 25 years of reprocessed sea level altimetry products. *Ocean Science* 15: 1207–1224, doi:10.5194/os-15-1207-2019.
- Talley, L. D. (2013). Closure of the Global Overturning Circulation Through the Indian, Pacific, and Southern Oceans: Schematics and Transports. *Oceanography* 26: 80–97, doi:10.5670/oceanog.2013.07.
- Talley, L. D., Pickard, G. L., Emery, W. J. and Swift, J. H. (2011). *Descriptive Physical Oceanography: An Introduction*. Boston: Academic Press, 6th ed., doi:10.1016/C2009-0-24322-4.
- Testor, P., de Young, B., Rudnick, D. L., Glenn, S., Hayes, D., Lee, C. M., Pattiariatchi, C., Hill, K., Heslop, E., Turpin, V., Alenius, P., Barrera, C., Barth, J. A., Beaird, N., Bécu, G., Bosse, A., Bourrin, F., Brearley, J. A., Chao, Y., Chen, S., Chiggiato, J., Coppola, L., Crout, R., Cummings, J., Curry, B., Curry, R., Davis, R., Desai, K., DiMarco, S., Edwards, C., Fielding, S., Fer, I., Frajka-Williams, E., Gildor, H., Goni, G., Gutierrez, D., Haugan, P., Hebert, D., Heiderich, J., Henson, S., Heywood, K., Hogan, P., Houptert, L., Huh, S., E. Inall, M., Ishii, M., Ito, S.-i., Itoh, S., Jan, S., Kaiser, J., Karstensen, J., Kirkpatrick, B., Klymak, J., Kohut, J., Krahmann, G., Krug, M., McClatchie, S., Marin, F., Mauri, E., Mehra, A.,

P. Meredith, M., Meunier, T., Miles, T., Morell, J. M., Mortier, L., Nicholson, S., O'Callaghan, J., O'Conchubhair, D., Oke, P., Pallàs-Sanz, E., Palmer, M., Park, J., Perivoliotis, L., Poulaire, P.-M., Perry, R., Queste, B., Rainville, L., Rehm, E., Roughan, M., Rome, N., Ross, T., Ruiz, S., Saba, G., Schaeffer, A., Schönau, M., Schroeder, K., Shimizu, Y., Sloyan, B. M., Smeed, D., Snowden, D., Song, Y., Swart, S., Tenreiro, M., Thompson, A., Tintore, J., Todd, R. E., Toro, C., Venables, H., Wagawa, T., Waterman, S., Watlington, R. A. and Wilson, D. (2019). OceanGliders: A Component of the Integrated GOOS. *Frontiers in Marine Science* 6: 422, doi:10.3389/fmars.2019.00422.

Thomas, G., Purkey, S. G., Roemmich, D., Foppert, A. and Rintoul, S. R. (2020). Spatial Variability of Antarctic Bottom Water in the Australian Antarctic Basin From 2018–2020 Captured by Deep Argo. *Geophysical Research Letters* 47: e2020GL089467, doi:10.1029/2020GL089467.

Thomson, R. E. and Emery, W. J. (2014). *Data Analysis Methods in Physical Oceanography*. Amsterdam: Elsevier, 3rd ed., doi:10.1016/C2010-0-66362-0.

Thorpe, S. A. (1977). Turbulence and mixing in a Scottish Loch. *Philosophical Transactions of the Royal Society of London. Series A, Mathematical and Physical Sciences* 286: 125–181, doi:10.1098/rsta.1977.0112.

Tochimoto, E. and Iizuka, S. (2022). Impact of warm sea surface temperature over a Kuroshio large meander on extreme heavy rainfall caused by an extratropical cyclone. *Atmospheric Science Letters* e1135, doi:10.1002/asl.1135.

Toole, J. M., Schmitt, R. W. and Polzin, K. L. (1994). Estimates of Diapycnal Mixing in the Abyssal Ocean. *Science* 264: 1120–1123, doi:10.1126/science.264.5162.1120.

Trenberth, K. E., Fasullo, J. T., Branstator, G. and Phillips, A. S. (2014). Seasonal aspects of the recent pause in surface warming. *Nature Climate Change* 4: 911–916, doi:10.1038/nclimate2341.

Valla, D., Piola, A. R., Meinen, C. S. and Campos, E. (2019). Abyssal Transport Variations in the Southwest South Atlantic: First Insights From a Long-Term Observation Array at 34.5°S. *Geophysical Research Letters* 46: 6699–6705, doi:10.1029/2019GL082740.

Voet, G., Alford, M. H., Girton, J. B., Carter, G. S., Mickett, J. B. and Klymak, J. M. (2016). Warming and Weakening of the Abyssal Flow through Samoan Passage. *Journal of Physical Oceanography* 46: 2389–2401, doi:10.1175/JPO-D-16-0063.1.

Voet, G., Girton, J. B., Alford, M. H., Carter, G. S., Klymak, J. M. and Mickett, J. B. (2015). Pathways, Volume Transport, and Mixing of Abyssal Water in the Samoan Passage. *Journal of Physical Oceanography* 45: 562–588, doi:10.1175/JPO-D-14-0096.1.

von Kietzell, A., Schurer, A. and Hegerl, G. C. (2022). Marine heatwaves in global sea

surface temperature records since 1850. *Environmental Research Letters* 17: 084027, doi:10.1088/1748-9326/ac81db.

Von Storch, H. and Zwiers, F. W. (1999). *Statistical Analysis in Climate Research*. Cambridge University Press, 1st ed., doi:10.1017/CBO9780511612336.

Wang, Y.-L., Jin, F.-F., Wu, C.-R. and Qiu, B. (2024). Northwestern Pacific Oceanic circulation shaped by ENSO. *Scientific Reports* 14: 11684, doi:10.1038/s41598-024-62361-z.

Wang, Y.-L., Wu, C.-R. and Chao, S.-Y. (2016). Warming and weakening trends of the Kuroshio during 1993–2013. *Geophysical Research Letters* 43: 9200–9207, doi:10.1002/2016GL069432.

Warren, B. A. (1973). Transpacific hydrographic sections at lats. 43°S and 28°S: The SCORPIO expedition—II. deep water. *Deep Sea Research and Oceanographic Abstracts* 20: 9–38, doi:10.1016/0011-7471(73)90040-5.

Warren, B. A. (1981). Transindian hydrographic section at Lat. 18°S: Property distributions and circulation in the South Indian Ocean. *Deep Sea Research Part A. Oceanographic Research Papers* 28: 759–IN48, doi:10.1016/S0198-0149(81)80001-5.

Warren, B. A. and Voorhis, A. D. (1970). Velocity Measurements in the Deep Western Boundary Current of the South Pacific. *Nature* 228: 849–850, doi:10.1038/228849b0.

Watts, D. R. and Kontoyiannis, H. (1990). Deep-Ocean Bottom Pressure Measurement: Drift Removal and Performance. *Journal of Atmospheric and Oceanic Technology* 7: 296–306, doi:10.1175/1520-0426(1990)007<0296:DOBPMD>2.0.CO;2.

Wei, Y., Pei, Y. and Zhang, R.-H. (2015). Seasonal variability of the Kuroshio Current at the PN Section in the East China Sea based on in-situ observation from 1987 to 2010. *Acta Oceanologica Sinica* 34: 12–21, doi:10.1007/s13131-015-0662-3.

White, W. B. and Tai, C.-K. (1995). Inferring interannual changes in global upper ocean heat storage from TOPEX altimetry. *Journal of Geophysical Research: Oceans* 100: 24943–24954, doi:10.1029/95JC02332.

Whitworth III, T., Nowlin Jr., W. D., Pillsbury, R. D., Moore, M. I. and Weiss, R. F. (1991). Observations of the Antarctic Circumpolar Current and deep boundary current in the southwest Atlantic. *Journal of Geophysical Research: Oceans* 96: 15105–15118, doi:10.1029/91JC01319.

Whitworth III, T., Warren, B. A., Nowlin Jr., W. D., Rutz, S. B., Pillsbury, R. D. and Moore, M. I. (1999). On the deep western-boundary current in the Southwest Pacific Basin. *Progress in Oceanography* 43: 1–54, doi:10.1016/S0079-6611(99)00005-1.

Wijffels, S. E., Toole, J. M. and Davis, R. (2001). Revisiting the South Pacific subtropical circulation: A synthesis of World Ocean Circulation Experiment observations along 32°S. *Journal of Geophysical Research: Oceans* 106: 19481–19513, doi:10.1029/1999JC000118.

Willis, J. K., Roemmich, D. and Cornuelle, B. (2003). Combining altimetric height with broadscale profile data to estimate steric height, heat storage, subsurface temperature, and sea-surface temperature variability. *Journal of Geophysical Research: Oceans* 108, doi:10.1029/2002JC001755.

Wong, A. P. S., Keeley, R., Carval, T. and Argo Data Management Team (2022). Argo Quality Control Manual for CTD and Trajectory Data doi:10.13155/33951.

Wong, A. P. S., Wijffels, S. E., Riser, S. C., Pouliquen, S., Hosoda, S., Roemmich, D., Gilson, J., Johnson, G. C., Martini, K., Murphy, D. J., Scanderbeg, M., Bhaskar, T. V. S. U., Buck, J. J. H., Merceur, F., Carval, T., Maze, G., Cabanes, C., André, X., Poffa, N., Yashayaev, I., Barker, P. M., Guinehut, S., Belbéoch, M., Ignaszewski, M., Baringer, M. O., Schmid, C., Lyman, J. M., McTaggart, K. E., Purkey, S. G., Zilberman, N., Alkire, M. B., Swift, D., Owens, W. B., Jayne, S. R., Hersh, C., Robbins, P., West-Mack, D., Bahr, F., Yoshida, S., Sutton, P. J. H., Cancouët, R., Coatanoan, C., Dobbler, D., Juan, A. G., Gourrion, J., Kolodziejczyk, N., Bernard, V., Bourlès, B., Claustre, H., D'Ortenzio, F., Le Reste, S., Le Traon, P.-Y., Rannou, J.-P., Saout-Grit, C., Speich, S., Thierry, V., Verbrugge, N., Angel-Benavides, I. M., Klein, B., Notarstefano, G., Poulain, P.-M., Vélez-Belchí, P., Suga, T., Ando, K., Iwasaka, N., Kobayashi, T., Masuda, S., Oka, E., Sato, K., Nakamura, T., Sato, K., Takatsuki, Y., Yoshida, T., Cowley, R., Lovell, J. L., Oke, P. R., van Wijk, E. M., Carse, F., Donnelly, M., Gould, W. J., Gowers, K., King, B. A., Loch, S. G., Mowat, M., Turton, J., Rama Rao, E. P., Ravichandran, M., Freeland, H. J., Gaboury, I., Gilbert, D., Greenan, B. J. W., Ouellet, M., Ross, T., Tran, A., Dong, M., Liu, Z., Xu, J., Kang, K., Jo, H., Kim, S.-D. and Park, H.-M. (2020). Argo Data 1999–2019: Two Million Temperature-Salinity Profiles and Subsurface Velocity Observations From a Global Array of Profiling Floats. *Frontiers in Marine Science* 7, doi:10.3389/fmars.2020.00700.

Xu, Q., Liu, K., Wang, H. and Chen, X. (2024). Vertical structures and drivers of marine heatwaves and cold-spells in the Kuroshio Extension region. *Environmental Research Letters* 19: 054015, doi:10.1088/1748-9326/ad3b26.

Yang, H., Lohmann, G., Wei, W., Dima, M., Ionita, M. and Liu, J. (2016). Intensification and poleward shift of subtropical western boundary currents in a warming climate. *Journal of Geophysical Research: Oceans* 121: 4928–4945, doi:10.1002/2015JC011513.

Yatsu, A. (2019). Review of population dynamics and management of small pelagic fishes around the Japanese Archipelago. *Fisheries Science* 85: 611–639, doi:10.1007/s12562-019-01305-3.

Yoshida, T., Shimohira, Y., Rinno, H., Yokouchi, K. and Akiyama, H. (2006). Criteria for the Determination of a Large Meander of the Kuroshio Based on its Path Information. *Oceanography*

*in Japan* 15: 499–507, doi:10.5928/kaiyou.15.6\_499.

Zhang, Y., Du, Y., Feng, M. and Hobday, A. J. (2023). Vertical structures of marine heatwaves. *Nature Communications* 14: 6483, doi:10.1038/s41467-023-42219-0.

Zhang, Z.-L., Nakamura, H. and Zhu, X.-H. (2021). Seasonal velocity variations over the entire Kuroshio path part I: Data analysis and numerical experiments. *Journal of Oceanography* 77: 719–744, doi:10.1007/s10872-021-00604-7.

Zhou, C., Ren, H.-L., Geng, Y., Wang, R. and Wang, L. (2024). Seasonal predictability of SST anomalies and marine heatwaves over the Kuroshio extension region in the Copernicus C3S models. *Ocean Modelling* 189: 102361, doi:10.1016/j.ocemod.2024.102361.

Zhu, X.-H., Nakamura, H., Dong, M., Nishina, A. and Yamashiro, T. (2017). Tidal currents and Kuroshio transport variations in the Tokara Strait estimated from ferryboat ADCP data. *Journal of Geophysical Research: Oceans* 122: 2120–2142, doi:10.1002/2016JC012329.

Zilberman, N. V., Roemmich, D. H., Gille, S. T. and Gilson, J. (2018). Estimating the Velocity and Transport of Western Boundary Current Systems: A Case Study of the East Australian Current near Brisbane. *Journal of Atmospheric and Oceanic Technology* 35: 1313–1329, doi:10.1175/JTECH-D-17-0153.1.

Zilberman, N. V., Roemmich, D. H. and Gilson, J. (2020). Deep-Ocean Circulation in the Southwest Pacific Ocean Interior: Estimates of the Mean Flow and Variability Using Deep Argo Data. *Geophysical Research Letters* 47: e2020GL088342, doi:10.1029/2020GL088342.

Zilberman, N. V., Scanderbeg, M., Gray, A. R. and Oke, P. R. (2023a). Scripps Argo Trajectory-Based Velocity Product: Global Estimates of Absolute Velocity Derived from Core, Biogeochemical, and Deep Argo Float Trajectories at Parking Depth. *Journal of Atmospheric and Oceanic Technology* 40: 361–374, doi:10.1175/JTECH-D-22-0065.1.

Zilberman, N. V., Scanderbeg, M. C., Gray, A. R. and Oke, P. R. (2023b). Scripps Argo trajectory-based velocity product 2001-01 to 2022-12. In Scripps Argo Trajectory-Based Velocity Product [Dataset]. doi:10.6075/J0NK3F7V.

Zilberman, N. V., Thierry, V., King, B., Alford, M., André, X., Balem, K., Briggs, N., Chen, Z., Cabanes, C., Coppola, L., Dall'Olmo, G., Desbruyères, D., Fernandez, D., Foppert, A., Gardner, W., Gasparin, F., Hally, B., Hosoda, S., Johnson, G. C., Kobayashi, T., Le Boyer, A., Llovel, W., Oke, P., Purkey, S., Remy, E., Roemmich, D., Scanderbeg, M., Sutton, P., Walicka, K., Wallace, L. and van Wijk, E. M. (2023c). Observing the full ocean volume using Deep Argo floats. *Frontiers in Marine Science* 10, doi:10.3389/fmars.2023.1287867.